THE UNIVERSITY OF CHICAGO

DISCOVERY AND MODELING OF MILKY WAY STELLAR STREAMS

A DISSERTATION SUBMITTED TO
THE FACULTY OF THE DIVISION OF THE PHYSICAL SCIENCES
IN CANDIDACY FOR THE DEGREE OF
DOCTOR OF PHILOSOPHY

DEPARTMENT OF ASTRONOMY AND ASTROPHYSICS

BY

NORA SHIPP

CHICAGO, ILLINOIS

AUGUST 2021

For Harry.

Table of Contents

List of Figures

List of Tables

ACKNOWLEDGMENTS

I would like to say thank you to the many people who have supported me throughout my PhD and without whom I would not have been able to complete this dissertation:

First, I would like to thank my advisor, Alex Drlica-Wagner, for being the best teacher, mentor, and collaborator and for all of your support and encouragement throughout my PhD. Thank you also to my thesis committee, Wendy Freedman, Josh Frieman, Dan Hooper, and Andrey Kravtsov for your support in putting together this thesis and for helpful conversations over the years. I have also been fortunate to work with many incredible collaborators and mentors. In particular, I would like to thank Denis Erkal, Ting Li, Brian Yanny, and Adrian Price-Whelan. Thank you Denis, for your invaluable insight and advice, and for your positivity and encouragement that never fail to make science more fun. Thank you Ting, for being a great collaborator and for always being willing to provide helpful advice, scientific and otherwise. Thank you to Brian for your support and insight throughout my time at Fermilab. Thank you Adrian, for fun collaboration and honest and supportive conversations.

Thank you to many members of the UChicago Astro community for your support and friendship. Thank you to all the members of IDEA who have worked tirelessly to build community, support each other, and to make our department a better and more just place. Thank you to all my graduate school friends, including Amy, Andrew, Jason, Phil, Mandy, Emily, Rebecca, and Maya for tea desks, Jimmy's nights, cooking parties, quarantine bubbles, and generally for making grad school fun.

Finally, thank you to all of my family. Thank you to my parents, Bill and Ellen, and my sister, Lily, for your unwavering support and for always being there for me. Thank you to my parents-in-law, Manjit and Kiran, and my sister-in-law, Gouri, for being an amazing, supportive chosen family. And thank you to Gourav (and Bella!) – I couldn't have done this without you.

ABSTRACT

Stellar streams, the tidal remnants of accreted globular clusters and dwarf galaxies, are uniquely powerful tools for studying the Milky Way. In particular, they allow for strong constraints on the local distribution of dark matter, and they provide insight into how our Galaxy has evolved over time. Models of stellar streams enable measurements of the overall shape and mass of the Milky Way's halo, which is sensitive to dark matter and galaxy formation physics. On smaller scales, stellar streams are one of the most promising methods for detecting the presence of small clumps of dark matter, which will allow for unprecedented constraints on the nature of the dark matter particle. Streams also provide important constraints on the formation of the Milky Way stellar halo and the history of hierarchical structure formation in our Galaxy, as predicted by the standard Λ Cold Dark Matter (ΛCDM) cosmological model.

These studies require a large, well-observed sample of stellar streams with full 6D position and velocity measurements. Until recently, such a population was unattainable, but with the advent of large surveys, observations of stellar streams have improved significantly in recent years. In this thesis, I present my work on assembling and modeling the first such population of stellar streams in 6D.

First, I present the discovery of a large sample of stellar streams in the Dark Energy Survey, which increased the known population of streams by $\sim$ 50%, as well as the discovery of a unique stellar stream associated with the Palomar 13 globular cluster. I then describe the measurement of the velocities of this new sample of stellar streams via spectroscopic survey and with data from the Gaia satellite, and present results of modeling this population of stellar streams to constrain the distribution of matter in our Galaxy, including the mass of the Milky Way's largest satellite, the Large Magellanic Cloud. Finally, I conclude and discuss future efforts in the study of near-field cosmology with this population of 6D stellar streams.

CHAPTER 1

INTRODUCTION

Our Galaxy, the Milky Way, is a powerful astrophysical laboratory that has revolutionized our understanding of fields across astrophysics. The Milky Way offers a unique opportunity to precisely measure the structures and systems that make up a galaxy, providing unmatched insight into galactic structure and evolution as well as the behavior and distribution of dark matter at galactic scales. Near-field cosmology takes advantage of these precise measurements in order to test and inform theories of the structure and evolution of the Universe. Precise measurements of our Galaxy and its neighbors have revolutionized the study of galaxy formation, enabled strong constraints on the nature of dark matter, and challenged the standard Λ Cold Dark Matter (ΛCDM) cosmological model. Among the systems that can be studied around our Milky Way are stellar streams, the tidally disrupted remnants of Milky Way satellite galaxies and star clusters. These systems are particularly sensitive probes of the local matter distribution and the structure of our Galaxy, tracing the local gravitational potential at both large and small scales, and providing a snapshot of the accretion history of the Milky Way. They provide essential insight into the structure of our Galaxy that will improve our ability to place the Milky Way in a cosmological context, to make precise comparisons to simulations and extra-galactic observations, and to inform our understanding of the structure and evolution of our Universe. In this thesis, I present the discovery, analysis, and modeling of the first population of systematically-observed stellar streams in 6D.

1.1 The Milky Way

Galaxies are vast and complex systems. Our Milky Way consists of more than 100 billion stars, with the majority residing within a disk of spiral arms, as well as a central bulge and

bar, all embedded within a diffuse stellar and gaseous halo. All of these visible components are situated within an invisible dark matter halo that makes up $\sim$ 95% of the mass of the Galaxy.

The stellar and dark matter halos of the Milky Way are of particular interest in this thesis and generally within the field of near-field cosmology. Only a small fraction of the stars in the Milky Way reside within the diffuse stellar halo (Bell et al., 2008), and the gravitational potential in this region is dominated by dark matter. Halo stars are therefore sensitive to the underlying distribution of dark matter and are particularly sensitive probes of this dominant component of our Galaxy. In addition, studies of the dynamics and chemical composition of halo stars indicates that the stellar halo is predominantly made up of ancient and chemically pristine stars belonging to the disrupted, phase-mixed remnants of accreted systems (Bullock & Johnston, 2005; Bell et al., 2008), as predicted by the hierarchical theory of structure formation (Peebles, 1965; Press & Schechter, 1974; Blumenthal et al., 1984). The study of halo stars therefore enables studies of galaxy formation across cosmic time, the accretion history of the Milky Way, and the local distribution of dark matter.

However, not all structure in the halo is phase-mixed. The halo is a complex neighborhood consisting of accreted satellite galaxies and star clusters at varying phases of disruption. The population of undisrupted satellites of the Milky Way has been studied in the greatest detail, providing many constraints on theories of dark matter and galaxy formation. To date, > 50 satellite galaxies (Drlica-Wagner et al., 2020), and > 150 globular clusters (Harris, 2010) are known to reside within the Milky Way halo. Of particular interest is the Milky Way's largest satellite, the Large Magellanic Cloud (LMC). The LMC is a uniquely massive satellite galaxy, with a stellar mass of $2.7 \times 10^9\,\mathrm{M}_\odot$ (van der Marel, 2006), and a total mass of $> 10^{11}\,\mathrm{M}_\odot$, $\sim$15% that of the Milky Way (Erkal et al., 2019a).

In addition to these fully-intact satellites are many systems currently undergoing disruption, which contain unique information about the invisible dark matter halo in which they

are embedded and the history of the formation and evolution of the Milky Way.

1.2 Near-Field Cosmology

Through the study of our Milky Way, we can learn about the structure and evolution of our broader Universe. Near-field cosmology enables precise tests of a wide range of theories, on topics including galaxy formation, hierarchical structure formation, the nature of dark matter, reionization, and the formation of the first stars and galaxies.

Near-field cosmology enables strong constraints on the properties of dark matter via observations of the clustering of dark matter at small scales. Observations of satellite galaxies of the Milky Way provide precise measurements of the low-mass end of the matter power spectrum, which is particularly sensitive to deviations from the standard cold, collisionless dark matter model (Robles et al., 2019; Bullock & Boylan-Kolchin, 2017; Buckley & Peter, 2017). In addition, measurements of the inner profiles of dark matter halos at a range of scales, including the shape of the Milky Way potential (Prada et al., 2019), the radial distribution of satellites within our Galaxy (e.g. Bozek et al., 2016), and the inner profiles of low-mass subhalos (Bullock & Boylan-Kolchin, 2017), inform our understanding of the nature of dark matter.

Studies of the stellar populations and star formation histories of the Local Group galaxies enable studies of star and galaxy formation across cosmic time. The lowest mass galaxies remain beyond our detection limits in the early Universe . However, many satellites of the Milky Way have old and pristine stellar populations, making them fossil-like remnants of these early galaxies (Brown et al., 2014). By studying these systems, we can test theories of the formation of the first galaxies and stars (Frebel & Norris, 2015), the details of galaxy formation at small scales, and the effects of reionization (Robertson et al., 2010; Weisz et al., 2014; Boylan-Kolchin et al., 2015).

These studies, however, rely on our ability to accurately place our Galaxy in a cosmolog-

ical context. We must be able to make accurate comparisons between the Milky Way and Milky Way-like galaxies in cosmological simulations and extra-galactic observations in order to extrapolate observations beyond the Local Universe.

One important factor in these comparisons, is a precise measurement of the total mass of the Milky Way. In order to accurately match our Galaxy to predictions from cosmological simulations, we must be able to make one-to-one comparisons with Milky Way-like galaxies. However, the Milky Way mass is currently known only within a factor of $\sim$ 2 (Callingham et al., 2018; Eilers et al., 2018; Watkins et al., 2018), and the 3D shape and profile of the gravitational potential is even more uncertain (e.g. Law & Majewski, 2010). This uncertainty arises largely due to modeling assumptions and systematic uncertainties inherent in different methods of mass estimation. For example, many studies directly measure the mass only within a relatively small radius, and estimates of the total mass therefore require significant extrapolation. In addition, many mass measurements rely on an assumption of dynamical equilibrium within our Galaxy. Recent studies of the effect of the LMC on the Milky Way indicate that this assumption may significantly bias mass measurements (Erkal et al., 2020a). Therefore, reliable measurements of the total mass and the 3D potential of our Galaxy require tracers and models that extend to large distances throughout the halo and that take into account the influence of the LMC. Detailed measurements will further enable accurate comparisons between our Galaxy and theoretical predictions based on cosmological simulations, as well as comparisons between the Milky Way and the broader population of galaxies throughout our Universe.

Any study of the population of Milky Way satellites also requires an understanding of how a triaxial, multi-component potential like that of the Milky Way disrupts accreted systems. The inner potential of the Milky Way, dominated by the Galactic disk, is known to cause extreme disruption (Garrison-Kimmel et al., 2017), severely reducing the number of intact satellite galaxies. Satellites also disrupt as they orbit at larger distances within the halo of the

Milky Way (Johnston, 1998). Precise comparisons of the Milky Way satellite population to theoretical predictions require an understanding of how satellites are disrupted as a function of progenitor and orbital properties. In addition, it is essential to develop an understanding of how unique properties of our Galaxy, such as the relatively recent accretion of the massive LMC, may influence the disruption rate and surviving population of satellites. This process of disruption remains very uncertain, and in fact is a leading source of uncertainty in many simulations. Precise studies of near-field cosmology therefore require advancements in our understanding of how a population of satellites is accreted onto and disrupted by our Galaxy.

In these comparisons, it is also essential to consider ways in which the Milky Way may be unusual among galaxies of similar masses. In particular, the most massive satellites of the Milky Way – the LMC and it's less-massive partner, the Small Magellanic Cloud (SMC), distinguish our Galaxy from the majority of similarly-sized systems. Observations suggest that only $\sim$10% of Milky Way-like galaxies have satellites as massive as the LMC (Wang & White, 2012; Busha et al., 2011). The LMC is a significant perturber to the Milky Way system, with a mass of $\sim$ 15% that of the Galaxy (Erkal et al., 2019a; Vasiliev et al., 2021). The LMC compounds the above uncertainties, introducing further complexity to measurements of the mass and 3D potential of the Milky Way and the abundance and disruption rate of Milky Way satellites. As described above, the LMC is known to cause significant perturbations in the outer halo of the Milky Way, biasing dynamical measurements of the Galactic potential (Erkal et al., 2020a). In addition, the LMC is thought to have brought in its own population of satellite galaxies that is in the process of blending in with that of the Milky Way (Nadler et al., 2020; Jethwa et al., 2016). Studies of near-field cosmology therefore require a precise understanding of the effect of the LMC on the Milky Way system in order to make accurate cosmological predictions.

The open questions enumerated above, including the total mass and 3D potential of the Milky Way, the accretion and disruption history of Milky Way satellites, and the influence

of the LMC, can all be addressed via the study of the tidal remnants of Milky Way satellites – stellar streams.

1.3 Thesis Outline

This thesis focuses on the study of stellar streams. Observations of stellar streams enable unique insight into the formation and evolution of our Galaxy, including the build-up of the Galactic stellar halo and the disruption history of Milky Way satellites. In addition, streams are strong tracers of the local gravitational potential on both large and small scales, enabling precise measurements of the total mass and 3D potential of the Milky Way, the abundance of subhalos around our Galaxy, and the influence of significant perturbers like the LMC.

These essential measurements will deepen our understanding of our Galaxy, and enable unprecedented constraints on the properties of dark matter and galaxy formation throughout our Universe. However, these studies require precise measurements of a large population of stellar streams with complete position and velocity measurements. These measurements have only recently become attainable thanks to advances in large sky surveys. In this thesis, I present the assembly of the first such population of stellar streams and the first measurement the mass of the LMC with a population of stellar streams.

In Chapter 2, I present an overview of stellar streams in the Milky Way, and discuss their ability to inform studies of near-field cosmology. In Chapter 3, I discuss the observation of stellar streams and detail the datasets used in this work. In Chapter 4, I describe the discovery of eleven new stellar streams in the Dark Energy Survey (DES; Shipp et al., 2018) and in Chapter 5, I present the discovery of a unique stream associated with the Palomar 13 globular cluster in the DECaLS data (Shipp et al., 2020). In Chapter 6, I present measurements of the proper motions of the DES stellar streams using data from *Gaia* DR2, and illustrate evidence of the perturbation of these streams by the LMC (Shipp et al., 2019). In Chapter 7, I discuss constraints on the mass of the LMC from this population

of stellar streams (Shipp et al., 2021). Finally, in Chapter 8 I summarize the work presented in this thesis and discuss future efforts to address the science goals enumerated above with this unprecedented population of 6D stellar streams.

CHAPTER 2

STELLAR STREAMS

2.1 Overview

Stellar streams provide an exciting new avenue for further developing our understanding of our Galaxy, informing studies of near-field cosmology, and tightening constraints on dark matter and galaxy formation.

The study of stellar streams is a relatively new field, having taken off with the advent of large photometric surveys, such as the Two Micron All Sky Survey (2MASS, Skrutskie et al., 2006), the Sloan Digital Sky Survey (SDSS, York et al., 2000), and the Dark Energy Survey (DES, DES Collaboration, 2005). Today, more than 60 stellar streams have been discovered orbiting our Galaxy. Many of these streams, along with a wide variety of other tidal debris and halo structures can be seen in Figure 2.1. These streams have a range of morphologies, including the massive Sagittarius stream (Ibata et al., 1994), with long and broad tidal tails extending from the partially-bound Sagittarius dwarf spheroidal galaxy and wrapping around the Milky Way. At the other end of the spectrum are globular cluster-progenitor streams, which are thin and dynamically cold, and in many cases extend $< 10\,\mathrm{kpc}$. Between these extremes are a wide variety of tidal remnants, originating from dwarf galaxies and globular clusters with a range of masses and at varying states of disruption. These streams cover much of the sky, and in some cases extend to distances $> 50\,\mathrm{kpc}$, providing information on the distribution of matter throughout much of the Milky Way's halo.

2.2 Physics and Modeling of Stellar Streams

Stellar streams form as stars escape from the bound progenitor system to follow their own orbits around the Milky Way. This process of stream formation can be approximated starting with the simple case of a point mass satellite system following a circular orbit around a

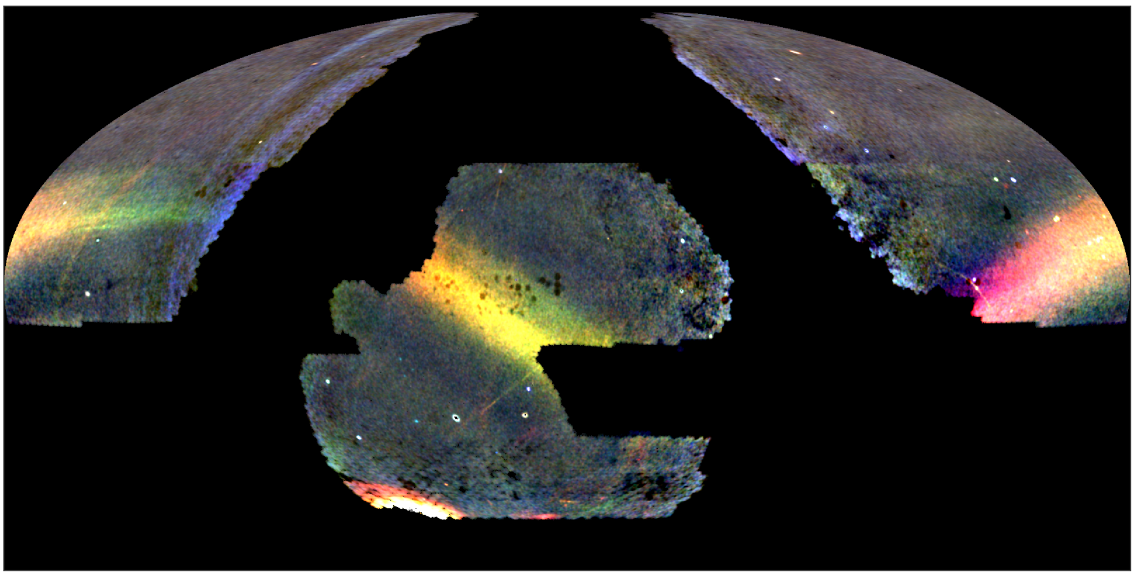

Figure 2.1 Density of stars in the Legacy Surveys dataset (Dey et al., 2018) passing an isochrone filter designed to select old, and metal-poor stellar populations, and color-coded by distance. Bluer stars are closer, and redder stars are farther away. A wide range of structure is visible in this figure, including many of the streams presented in this thesis, which lie within the DES footprint, centered in the image. The large band spanning the image is the Sagittarius stream. At the lower left of the DES footprint is the edge of the Large Magellanic Cloud.

massive host galaxy. In this "restricted three-body problem," as presented in Binney & Tremaine (2008), we can consider a reference frame rotating at the orbital frequency of the satellite, in which we may calculate a time-independent effective potential,

$$\mathbf{\Phi}_{\rm eff}(\boldsymbol{r}) = \mathbf{\Phi}(\boldsymbol{r}) - \frac{1}{2}\left|\mathbf{\Omega} \times \boldsymbol{r}\right|^2, \tag{2.1}$$

where $\mathbf{\Omega}$ is the vector $(0, 0, \Omega)$, and Ω is the orbital frequency of the circular orbit. In this setup, the only conserved quantity is the Jacobi integral (Binney & Tremaine, 2008), which is written as,

$$E_{\rm J} = \frac{1}{2}v^2 + \mathbf{\Phi}_{\rm eff}(\boldsymbol{r}). \tag{2.2}$$

When the velocity, v, goes to zero, $E_{\rm J} = \mathbf{\Phi}_{\rm eff}$. This boundary is referred to as the

"zero-velocity surface." Stars cannot pass beyond this surface, since v^2 will never equal less than zero. For values of $E_{\rm J}$ corresponding to orbits close to the satellite, these boundaries will fully encircle the satellite, trapping orbiting stars within the satellite system. However, at larger radii, there will be a point at which the gravitational fields of the satellite and host galaxy combine to produce a discontinuity in the regions contained by the zero-velocity surfaces. These saddle points in $\mathbf{\Phi}_{\rm eff}$, the inner and outer Lagrange points, represent the tidal radius of the satellite, at which stars may become unbound from the progenitor and begin to instead orbit the host galaxy.

The radius of these Lagrange points relative to the satellite, $r_{\rm J}$, may be calculated by determining the locations of these saddle points, and the result can be written as,

$$r_{\rm J} = \pm \left(\frac{Gm}{\Omega^2 - \frac{d^2\Phi}{dr^2}} \right)^{1/3}, \tag{2.3}$$

where m is the mass of the satellite, Ω is the instantaneous orbital frequency of the satellite, and Φ is the gravitational potential (King, 1962; Gibbons et al., 2014). This radius is referred to as the Jacobi limit of the satellite, and approximates the satellite's tidal radius. The inner and outer Lagrange points at $\pm r_{\rm J}$ represent the points at which stars are preferentially stripped from the satellite. Stars that are stripped at $-r_{\rm J}$, between the progenitor and host, have a negative ΔE and ΔL relative to the progenitor. They therefore have a shorter orbital period and move ahead of the progenitor to form the leading arm of the stellar stream. Similarly, stars stripped at the opposite Lagrange point have a larger orbital period and form the trailing arm of the stream.

In a realistic galaxy potential, this process is more complex. For a satellite on a non-circular orbit, there is no static effective potential, and even on circular orbits, this tidal radius is not a rigid divide between bound and unbound stars. However, numerical simulations have provided strong evidence for the effectiveness of this approximation in reproducing realistic tidal debris in a Milky Way-like system (Johnston, 2016).

Streams can therefore be simulated by stripping stars at these Lagrange points as the progenitor satellite orbits the host. This is the basis for the modified Lagrange cloud stripping technique proposed by Gibbons et al. (2014) and used in the simulations discussed in Chapter 7. The progenitor is rewound back a fixed amount of time along its orbit within the host potential. Then, at fixed time-steps, δt, stars are ejected from the progenitor at the Lagrange points at $\pm r_{\rm J}$, with velocities drawn from a Gaussian distribution centered on the progenitor velocity. Each of these stars is then evolved forward in the joint potential of the host and the progenitor to the present day.

This methodology produces more realistic stream models than methods that either assume that stripped stars follow the progenitor orbit (Sanders & Binney, 2013) or that fail to take into consideration the gravitational force from the progenitor after stripping (Gibbons et al., 2014).

2.3 Milky Way Potential Constraints

The fact that the formation and evolution of stellar streams is dependent on the underlying gravitational potential means that these systems are excellent probes of the local matter distribution. In addition, we know that the stars that make up a stellar stream once belonged to a single bound progenitor system, which provides additional constraints on their orbital histories relative to a population of independent stars (Johnston, 2016). For these reasons, Milky Way stellar streams are in fact powerful probes of the distribution of matter in our Galaxy on both large and small scales. On larger scales, streams trace the gravitational potential of the Galaxy over tens of kiloparsecs and have the ability to connect Milky Way mass measurements at a range of distances throughout the halo, extending far beyond the reach of the majority of Milky Way stars. Furthermore, because each stream is accreted at a different time and has a unique position in phase space, and therefore contains distinct information about the local matter distribution, measurements of multiple streams can be

combined to place even stronger constraints on both the total mass and the 3D profile of the Milky Way potential. In fact, Bonaca & Hogg (2018) predict that a population of a dozen well-observed stellar streams should be able to constrain Milky Way halo parameters to the percent-level. Streams also enable constraints of large-scale perturbers to the Milky Way potential. In particular, recent work has shown that stellar streams are sensitive to the gravitational potential and the orbit of the Large Magellanic Cloud (Erkal et al., 2019a, Shipp et al., 2021), which is discussed in greater detail in Chapter 7.

2.4 Small-scale Dark Matter Constraints

Stellar streams also enable strong constraints on the small-scale distribution of dark matter. Streams tend to be dynamically cold, and are therefore easily imprinted with lasting evidence of smaller-scale perturbations (Johnston, 2016). This makes streams unique probes of the small-scale structure within our Galaxy. Many leading dark matter models predict that the population of dark matter subhalos around our galaxy should extend to masses far below those probed by luminous satellite galaxies (Green et al., 2004; Diemand et al., 2005; Wang et al., 2020). The abundance of low-mass subhalos and, in particular, this mass cutoff, is sensitive to the particle physics of dark matter (Bullock & Boylan-Kolchin, 2017; Nadler et al., 2021). Detections of completely dark, low-mass subhalos would provide unprecedented constraints on the particle nature of dark matter. Stellar streams are one of only a couple of proposed methods for detecting these low-mass subhalos that contain no luminous baryonic component (Ibata et al., 2002; Johnston et al., 2002; Yoon et al., 2011a; Carlberg, 2012). Some of these subhalos orbiting within the halo of the Milky Way will inevitably collide with stellar streams, and will imprint the stream with a distinctive density perturbation, dependant on the properties of the subhalo and the interaction (Erkal & Belokurov, 2015a; Erkal et al., 2016b). Therefore, by studying density variations along stellar streams, we can indirectly infer the population of low-mass subhalos around the Milky Way – a strong test

of the nature of dark matter.

2.5 Accretion History of the Milky Way

Stellar streams also provide strong evidence of the hierarchical merger history of our Galaxy (Johnston, 1998). These tidally disrupted remnants of accreted globular clusters and dwarf galaxies provide a unique snapshot of the accretion process, bridging the gap between the population of undisrupted stellar systems that have been accreted onto the Milky Way system, and the diffuse stellar halo. Stellar streams originate from both galaxies and star clusters, and studying each of these populations, both independently and in comparison, provides valuable information about the formation history of our Galaxy and the evolution of these satellite populations of the Milky Way. In addition, by making comparisons to the populations of intact satellite galaxies and globular clusters, we can reveal the process by which systems disrupt and become phase-mixed within the Milky Way.

2.6 Milky Way Stellar Streams

Recent datasets have enabled an acceleration in the discovery of stellar streams, with many discovered within recent years in surveys such as DES (Shipp et al., 2018, Chapter 3) and *Gaia* (Malhan & Ibata, 2018). In addition, recent observations have enabled a more detailed look at many of these systems. For example, deeper photometric and astrometric data have enabled precise studies of the density variations along stellar streams (e.g. Bonaca et al., 2019b; Banik & Bovy, 2018), informing searches for interactions with low-mass subhalos. Proper motion measurements from *Gaia* and radial velocity measurements from spectroscopic surveys such as the Southern Stellar Stream Spectroscopic Survey (S^5; Li et al., 2019) have provided kinematic measurements for a large population of stellar streams, enabling unprecedented dynamical modeling, including mass measurements of the Milky Way (Erkal

et al., 2019a) and studies of the influence of the LMC (Erkal et al., 2019a, Shipp et al. 2021). In addition, spectroscopy enables measurements of the chemical compositions of streams, providing information about the properties of the population of progenitor systems that has been accreted and disrupted to form these tidal remnants (Ji et al., 2020). As we build upon the progress of recent years, and continue towards a complete census of the population of Milky Way stellar streams, we will enable precise measurements of the total mass and 3D potential of our Galaxy and its perturbers, the population of dark subhalos, and the accretion and disruption history of Milky Way satellites. These measurements will provide essential input to studies of near-field cosmology, further enabling us to place our Galaxy in a cosmological context and to test theories of galaxy formation and the nature of dark matter in the Local Universe.

CHAPTER 3

OBSERVATIONAL DATA

The study of near-field cosmology with stellar streams requires a variety of detailed measurements. The precise dynamical modeling of streams requires kinematic data, and ideally complete 6D position and velocity measurements of the individual stars that make up each stellar stream. In the context of astronomical observations, this 6D data comprises positions on the sky, proper motions along the sky, radial velocities, and distances.

Another important consideration is that stellar streams are not isolated on the sky, and instead are embedded within a complicated projection of astrophysical objects, including stars situated in different components of our Galaxy as well as extragalactic sources. We must therefore take advantage of observed properties of these systems in order to disentangle the stars that make up a stellar stream from contaminating systems. This requires measurements of the morphologies of sources and their colors and magnitudes at different wavelengths.

Finally, in order to study in greater detail the structures that are disrupted and evolve into stellar streams, it is important to have measurements of the metallicities and the chemical compositions of these structures. These data provide insight into the origins of these systems and the nature of their progenitors.

All of these data come together to elucidate the origin and evolution of these structures and enable detailed inferences about the structure and evolution of our Galaxy. However, assembling this complex dataset is no easy feat and requires collecting data from various sources using various types of instruments. In this chapter, I describe the different types of data that must come together to provide a detailed view of a stellar stream, as well as some of the datasets that have enabled this work.

This chapter is divided into sections corresponding to different types of measurements, namely photometry, astrometry, and spectroscopy, each of which provides different components of the data enumerated above.

3.1 Photometry

Photometry consists of measuring the flux of light coming from an object within a given wavelength range. Cutting-edge photometric surveys employ giant digital cameras made up of collections of CCDs, which take images of patches of the night sky. The collected data enables measurements of the morphology and brightness of objects across wavelength bins. This data is used to distinguish stars from galaxies, and can be used to pull out certain stellar populations. In color-magnitude space, single-age stellar populations are distributed along distinctive curves, referred to as isochrones. Isochrones depend on the population age and metallicity, and the whole curve shifts in apparent magnitude as a function of distance. Thin, faint stellar streams tend to originate from progenitors with simple, one-generation, old and metal-poor stellar populations. Stream member stars therefore tend to be tightly clustered around particular isochrones. This feature of stellar populations allows us to select stars likely to belong to a given stellar stream and to eliminate much of the foreground contamination from other Galactic stars. It also enables measurements of the ages, metallicities, and distances of stream member stars. This methodology is a key component of many searches for stellar streams in photometric data, and is described in greater detail in Chapter 4, in which I present the discovery of stellar streams in the photometric dataset from the Dark Energy Survey.

Wide-area, multi-band photometric surveys have revolutionized the study of the Milky Way halo. The Sloan Digital Sky Survey (SDSS; York et al., 2000) provided unprecedented measurements of resolved stellar populations in the Galactic halo, including diffuse structures (e.g. Carollo et al., 2007; de Jong et al., 2010; Deason et al., 2011; Hattori et al., 2013), satellite galaxies (e.g. Willman et al., 2005a,b; Belokurov et al., 2007a), stellar clouds (e.g. Newberg et al., 2002; Yanny et al., 2003), and stellar streams (e.g. Belokurov et al., 2006a; Grillmair, 2006). Along with SDSS, recent photometric surveys, such as Pan-STARRS (Bernard et al., 2014; Grillmair, 2017a), ATLAS (Koposov et al., 2014), the Dark Energy

Survey (Balbinot et al., 2016; Shipp et al., 2018), and the DESI Legacy Imaging Surveys (Shipp et al., 2020), have since collectively enabled the discovery of > 50 stellar streams. In this thesis, I present the discovery of 12 stellar streams in the Dark Energy Survey and DESI Legacy Imaging Surveys datasets.

3.1.1 The Dark Energy Survey

The Dark Energy Survey (DES; DES Collaboration, 2005, 2016) is a deep, wide-area imaging survey using the Dark Energy Camera (Flaugher et al., 2015), on the 4m Blanco Telescope at Cerro Telolo Inter-American Observatory in Chile. The primary goal of the survey is to constrain dark energy and the nature of cosmic acceleration (DES Collaboration, 2017). The precise calibration and data uniformity required for this goal also makes the DES data perfectly suited for observations of the Milky Way stellar distribution. DES has had a major impact on our understanding of the local stellar and dark matter distributions, nearly doubling the number of known ultra-faint dwarf galaxies (Bechtol et al., 2015; Drlica-Wagner et al., 2015; Koposov et al., 2015), increasing the number of known faint halo star clusters (Pieres et al., 2016; Luque et al., 2016, 2017, 2018), identifying several diffuse stellar overdensities (Li et al., 2016; Pieres et al., 2017), and, as described in Chapter 4 of this thesis, enabling the discovery of a large population of stellar streams (Shipp et al., 2018).

The DES footprint covers an area of $\sim 5000\,\mathrm{deg}^2$, roughly 1/8 of the sky, around the southern Galactic cap. The survey covers this region in five optical and near-infrared filters, $grizY$ with a g-band depth of 24.6 mag, > 2 mag deeper than SDSS (Abbott et al., 2021; Abazajian et al., 2009). The data is discussed in greater detail in Chapter 4.

3.1.2 The DECam Legacy Survey

The DECam Legacy Survey (DECaLS) is a component of the DESI Legacy Imaging Surveys (Dey et al., 2019), an optical and infrared imaging survey covering $14,000\,\mathrm{deg}^2$. The DECaLS

program consists of DECam imaging across the northern and southern Galactic caps in the grz bands, incorporating existing imaging in the region, including from DES, and extending observations beyond existing survey footprints up to Dec $\sim 32\,\mathrm{deg}$. The g-band depth is 23.7 mag, $\sim$ 1 magnitude shallower than DES. In Chapter 5, I discuss the data in greater detail, and present the discovery of extended tidal tails from the Palomar 13 globular cluster in the DECaLS data.

3.2 Astrometry

Astrometry is the precise measurement of the positions of stars on the sky. This is essential not only for identifying precise 2D coordinates of stars, but also for deriving distances via parallax measurements, and for measuring the proper motions of stars – their motion within the plane of the sky. For stellar streams, proper motion measurements, derived from the comparison of precise position measurements at different epochs, are an essential component of 6D phase space measurements, necessary for the dynamical modeling of stellar streams.

The astrometric satellite Hipparcos (Perryman et al., 1997), launched in 1989, was the first to provide global astrometric measurements across the sky. These global measurements enabled comparison to a consistently-defined reference frame and allowed for uniformity in instrument systematics. Hipparcos provided astrometric measurements of $> 100,000$ stars to unprecedented precision and had a significant impact on a wide range of areas of study across the field of astronomy.

The Gaia mission (Gaia Collaboration et al., 2016, 2018) has built upon the methodology developed by Hipparcos to obtain astrometric measurements of $>$ 1 billion stars to 100 times the precision of Hipparcos. Gaia has truly revolutionized the study of stellar streams by providing precise astrometric measurements of stars out to large distances in the Milky Way's halo. I describe the Gaia data in greater detail here, and in Chapter 6 I present measurements of the proper motions of a population of stellar streams using data from the

second data release of Gaia (DR2).

3.2.1 Gaia

The Gaia satellite is an astrometric space mission with the goal of making the largest and most precise 3D map of the stellar population of the Milky Way. Gaia hosts three instruments – the astrometric instrument, the photometric instrument, and the radial velocity spectrometer, which enable the observatory to measure positions, proper motions, parallaxes, color, magnitude, and radial velocity of a large population of stars. The latest Gaia data release, the early third data release (EDR3; Gaia Collaboration et al., 2020), released in December 2020, included full astrometric solutions – including positions, proper motions, and parallaxes – of >1.4 billion stars, to a limiting magnitude of ~ 21 mag. The proper motion measurements from Gaia in particular have revolutionized the study of stellar streams, providing kinematic measurements of a large population of Milky Way stellar streams, and enabling unprecedented dynamical studies of the tidal remnants in our Galaxy. The proper motion uncertainties of EDR3 are 0.07 mas/yr at a magnitude in the *Gaia* G band of G=17 mag and 1.4 mas/yr at G=21 mag, enabling measurements of the proper motions of main sequence turnoff stars out to $\sim$ 25 kpc, and red giant branch stars at distances up to > 50 kpc. Future data releases, including the third data release expected in early 2022, will further extend these measurements to a larger population of stars in our Galaxy and improve the precision of existing measurements. The Gaia proper motions and their application to the study of stellar streams are discussed in greater detail in Chapter 6.

3.3 Spectroscopy

Spectroscopy enables the detection of electromagnetic radiation from an astronomical source as a function of wavelength, allowing for measurements of chemical compositions and radial velocities. Spectroscopy is an important component of the detailed study of stellar streams,

providing essential measurements of kinematic and chemical properties of streams that cannot be obtained with photometric and astrometric observations alone.

Spectroscopic surveys of stellar streams are difficult due to the faint and diffuse nature of the majority of known Milky Way streams, as well as the presence of significant foreground contamination from Milky Way stars. Until recently, therefore, the majority of spectroscopic observations of stellar streams were not part of large survey programs, and instead were obtained by individual observers. The vast majority of known streams had no spectroscopic measurements at all. However, beginning in 2018, the Southern Stellar Stream Spectroscopic Survey (S^5; Li et al., 2019) has for the first time obtained systematic spectroscopic measurements of a large population of stellar streams across the southern sky.

3.3.1 The Southern Stellar Stream Spectroscopic Survey

S^5 is the first spectroscopic survey of stellar streams in the Milky Way halo, and aims to measure radial velocities and metallicities of stellar streams across the southern sky. S^5 began with the observation of the DES streams presented in Chapter 4, and has since continued on to observe more than 21 stellar streams.

Much of the challenge of spectroscopic observations of stellar streams is due to the difficulty of target selection and the resulting inefficiency of observations. S^5 has mitigated these challenges by taking advantage of recent cutting-edge datasets, increasing the efficiency of target selection and enabling the first efficient and systematic spectroscopic survey of stellar streams. In particular, S^5 utilizes the precise photometry from DES (Chapter 4) and proper motion measurements from Gaia (Chapter 6) to optimize the selection of likely stream member stars.

S^5 uses the Two-degree Field (2dF) fiber positioner (Lewis et al., 2002) and the AAOmega spectrograph (Sharp et al., 2006) on the 3.9 meter Anglo Australian Telescope (AAT). This setup allows for observations of $\sim 3\,\mathrm{deg}^2$ fields with 392 science fibers. The dramatic im-

provements in target selection have enabled not only an efficient survey of stellar streams, but have led to the availability of spare fibers, allowing for two auxiliary science programs – a low-z galaxy survey, and a halo star survey.

The S^5 data, when combined with the precise photometric observations from DES, and the unprecedented proper motions provided by *Gaia*, complete the 6D phase-space measurements of the DES stellar streams. For a detailed overview of the survey, see Li et al. (2019). The proper motion measurements used in S^5 target selection are discussed in Chapter 6 and Shipp et al. (2019), and the use of the S^5 data in the dynamical modeling of stellar streams is described in greater detail in Chapter 7 and Shipp et al., 2021.

CHAPTER 4

STELLAR STREAMS DISCOVERED IN THE DARK ENERGY SURVEY

The text of this chapter was published in Shipp et al. ApJ 862, 2 (2018).

4.1 Introduction

Stellar streams produced by the tidal disruption of globular clusters and dwarf galaxies are a prevalent feature of the Milky Way environs (see Newberg & Carlin, 2016, for a recent review). Observations of stellar streams can provide important constraints on the formation of the Milky Way stellar halo (e.g., Johnston, 1998; Bullock & Johnston, 2005; Bell et al., 2008), the shape of the Galactic gravitational field (e.g., Johnston et al., 2005; Koposov et al., 2010; Law & Majewski, 2010; Bovy, 2014; Bonaca et al., 2014; Gibbons et al., 2014; Price-Whelan et al., 2014; Sanders, 2014; Bowden et al., 2015; Küpper et al., 2015b; Erkal et al., 2016b; Bovy et al., 2016), and the abundance of low-mass dark matter substructure (e.g., Ibata et al., 2002; Johnston et al., 2002; Carlberg, 2009; Yoon et al., 2011a; Carlberg, 2012; Ngan & Carlberg, 2014; Erkal & Belokurov, 2015a; Carlberg, 2016; Sanderson et al., 2016; Sanders et al., 2016; Bovy et al., 2017; Erkal et al., 2017; Sandford et al., 2017). In addition, stellar streams are a direct snapshot of hierarchical structure formation (Peebles, 1965; Press & Schechter, 1974; Blumenthal et al., 1984) and support the standard ΛCDM cosmological model (Diemand et al., 2008; Springel et al., 2008).

Wide-area, multi-band digital sky surveys have been essential for finding and characterizing resolved stellar populations in the Galactic halo. The Sloan Digital Sky Survey (SDSS; York et al., 2000) revolutionized our understanding of the Milky Way stellar halo, both through improved sensitivity to diffuse components (e.g., Carollo et al., 2007, 2010; de Jong et al., 2010; Deason et al., 2011; An et al., 2013; Kafle et al., 2013; Hattori et al., 2013;

An et al., 2015; Das & Binney, 2016) and by vastly increasing the number of known satellite galaxies (e.g., Willman et al., 2005a,b; Zucker et al., 2006a,b; Belokurov et al., 2006b, 2007b), stellar clouds (e.g., Newberg et al., 2002; Yanny et al., 2003; Rocha-Pinto et al., 2004), and stellar streams (e.g., Odenkirchen et al., 2001; Newberg et al., 2002; Belokurov et al., 2006a; Grillmair, 2006). Early techniques for detecting stellar streams used simple color and magnitude cuts to select blue main sequence turn-off (MSTO) stars (e.g., Grillmair et al., 1995; Belokurov et al., 2006a). More recently, matched-filter techniques have been used to maximize the contrast between distant, metal poor stellar populations and foreground field stars to push the detection limit to lower surface brightnesses (e.g. Rockosi et al., 2002). The matched-filter technique has been applied broadly to other digital sky surveys including Pan-STARRS (Bernard et al., 2014, 2016; Grillmair, 2017a) and ATLAS (Koposov et al., 2014).

The Dark Energy Survey (DES; DES Collaboration, 2005, 2016) is a deep, wide-area survey with the primary goal of constraining dark energy and the nature of cosmic acceleration (e.g., DES Collaboration, 2017). While DES was designed to probe the evolution of the universe out to $z \sim 1.2$, it has already had a major impact on "near-field" cosmology and Galactic archaeology. Specifically, DES has nearly doubled the number of known ultra-faint dwarf galaxies (Bechtol et al., 2015; Koposov et al., 2015; Kim & Jerjen, 2015; Drlica-Wagner et al., 2015), increased the number of known faint outer-halo star clusters (Pieres et al., 2016; Luque et al., 2016, 2017, 2018), and identified several diffuse stellar overdensities (Li et al., 2016; Pieres et al., 2017). In addition, early data from DES have been used to detect a cold stellar stream in the constellation of Phoenix (Balbinot et al., 2016) and a tidal stream associated with the ultra-faint satellite, Tucana III (Drlica-Wagner et al., 2015). Here we extend the search for stellar streams with DES using a deeper, more uniform, and better calibrated data set.

We perform a search for stellar streams using the first three years of DES data. We search

for stellar streams possessing old, metal-poor stellar populations at heliocentric distances between $6\,\mathrm{kpc} \lesssim \mathrm{D}_\odot \lesssim 63\,\mathrm{kpc}$ ($14 < m - M < 19$). We recover known streams within the DES footprint, including Sagittarius (Ibata et al., 2001; Newberg et al., 2002), ATLAS (Koposov et al., 2014), Phoenix (Balbinot et al., 2016), and Tucana III (Drlica-Wagner et al., 2015). In addition, we detect a possible faint extension of the Molonglo stream (Grillmair, 2017a) in the DES data. Our search results in the discovery of eleven new high-significance curvilinear stellar stream candidates. These new stream candidates range in distance from $\sim 13\,\mathrm{kpc}$ to $\sim 50\,\mathrm{kpc}$. These streams are low surface brightness, $\mu \gtrsim 32\,\mathrm{mag/\,arcsec^2}$, and push the boundary of detectability using the current generation of wide-area photometric surveys. As a natural by-product of a global search for extended stellar structures, we find evidence for extended extra-tidal features around the Milky Way globular clusters NGC 288, NGC 1261, NGC 1851, and NGC 1904.

This paper is organized as follows. In Section 4.2 we discuss the DES data and the construction of the stellar sample used in this work. In Section 4.3 we present our matched-filter search algorithm and maximum-likelihood techniques that we implement for characterizing stellar streams. In Section 4.4 we discuss the properties of previously known and newly detected stellar streams. We place our results in the larger context of the Milky Way in Section 4.5 and conclude in Section 4.6.

4.2 Data Set

DES is a deep, wide-area imaging survey using the Dark Energy Camera (DECam; Flaugher et al., 2015) mounted on the 4-m Blanco Telescope at Cerro Tololo Inter-American Observatory in Chile. DES surveys $\sim 5000\,\mathrm{deg^2}$ of the southern Galactic cap in five visible/near-infrared filters, $grizY$. Here, we use wide-field imaging data from an internal data release

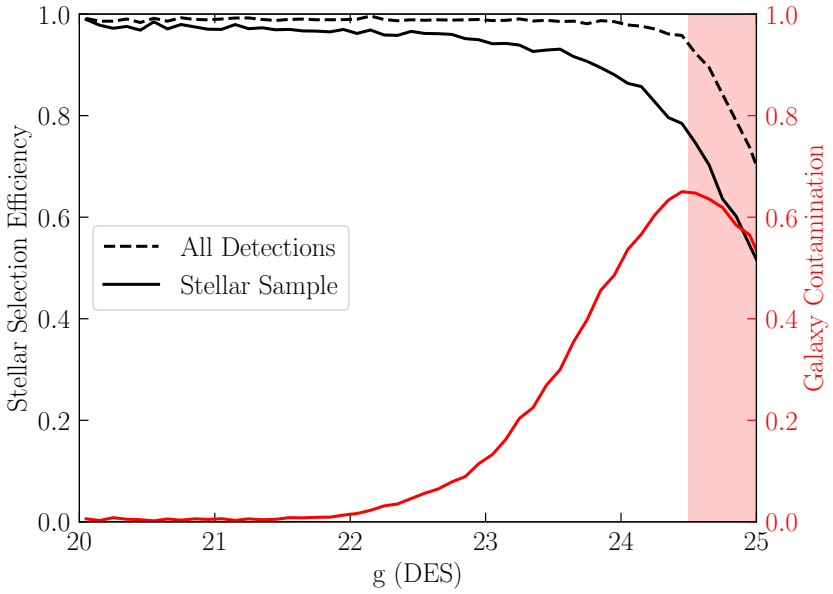

Figure 4.1 Stellar selection efficiency and galaxy contamination for the DES Y3 data evaluated from a comparison to HSC DR1 using ~ 18 deg^2 of overlap in the SDSS Stripe 82 region. The DES efficiency is evaluated with respect to a stellar sample from HSC. The red shaded band indicates the faint magnitude range where the HSC data are affected by star-galaxy confusion and may be less reliable as a test sample. Our stellar classification primarily uses the `ngmix` multi-epoch fitting size parameter and error.

of the first three years of DES operations (DES Y3A2).[1] DES Y3A2 is the first data set to cover the full DES wide-area footprint, and has a median coverage of 5–6 exposures per filter (Diehl et al., 2016). The contiguous, uniform, wide-area imaging of DES allows for the first deep, systematic search for faint features in the Milky Way stellar halo in this region of the southern sky.

The DES Y3A2 images were processed by the DES data management pipeline (Morganson et al., 2018). Photometric calibration was performed via the Forward Global Calibration Method (FGCM; Burke et al., 2018), which utilized ancillary information about atmospheric and environmental conditions at the time of each exposure. The FGCM photometric calibration is found to have a relative photometric uniformity of ~ 7 mmag (Burke et al., 2018) and an absolute calibration accuracy of ~ 3 mmag (DES Collaboration et al., 2018). Individual exposures were remapped to a consistent pixel grid and coadded to increase imaging depth (Morganson et al., 2018). Object detection was performed on a combination of the $r + i + z$ coadded images using the `SExtractor` toolkit (Bertin & Arnouts, 1996; Bertin et al., 2002) with an object detection threshold corresponding to S/N ~ 10 (Morganson et al., 2018).

While the coadded images increase our sensitivity to faint sources, depth variations and PSF discontinuities in the coadds can make it difficult to perform precise photometric and morphological measurements (e.g., Drlica-Wagner et al., 2018). To circumvent this issue, we used `ngmix`[2] (Sheldon, 2014; Jarvis et al., 2016; Drlica-Wagner et al., 2018) to fit the flux and morphology of each source over all individual single-epoch images simultaneously. When fitting each source we masked nearby neighbors using the `uberseg` map, which was derived from the `SExtractor` coadd segmentation maps (Section 5.2 of Jarvis et al., 2016).[3]

1. DES Y3A2 serves as the basis for the first public DES data release (DES DR1; DES Collaboration et al., 2018). However, the internal Y3A2 data release contains improved multi-epoch photometric and morphological measurements as well as other auxiliary data products.

2. `https://github.com/esheldon/ngmix`

3. Masking nearby sources yields slightly less accurate photometry than the iterative multi-object fitting (MOF) described by Drlica-Wagner et al. (2018); however, masking is less computationally intensive and has a lower failure rate than MOF.

Throughout this paper, quoted magnitudes and errors were derived from fitting a PSF model to each source using `ngmix` (i.e., `PSF_MAG` and `PSF_MAG_ERR`).

To select a high-quality stellar sample, we expanded on the star-galaxy classification procedure outlined in Appendix A of Rozo et al. (2016). We used `ngmix` to fit a composite galaxy model (bulge plus disk) to each source in all bands simultaneously (Drlica-Wagner et al., 2018). We then used the best-fit size, `CM_T`, and associated uncertainty, `CM_T_ERR`, from this galaxy-model fit to distinguish point-like objects from those that are spatially extended. Specifically, we defined an extended classification variable, `NGMIX_CLASS`, based on the sum of three selection criteria,

$$\begin{aligned} \texttt{NGMIX\_CLASS} = &((\texttt{CM\_T} + 5\,\texttt{CM\_T\_ERR}) > 0.1) \\ &+ ((\texttt{CM\_T} + \texttt{CM\_T\_ERR}) > 0.05) \\ &+ ((\texttt{CM\_T} - \texttt{CM\_T\_ERR}) > 0.02). \end{aligned} \tag{4.1}$$

The `ngmix` composite galaxy-model fit fails for a small number of bright stars. To recover those objects, we defined a second selection based on the weighted-average `SExtractor` quantity `WAVG_SPREAD_MODEL` measured in the DES i-band (Morganson et al., 2018),

$$\begin{aligned} &\texttt{WAVG\_CLASS} = \\ &\quad((\texttt{WAVG\_SPREAD\_MODEL\_I} + 3\,\texttt{WAVG\_SPREADERR\_MODEL\_I}) > 0.005) \\ &+((\texttt{WAVG\_SPREAD\_MODEL\_I} + \texttt{WAVG\_SPREADERR\_MODEL\_I}) > 0.003) \\ &+((\texttt{WAVG\_SPREAD\_MODEL\_I} - \texttt{WAVG\_SPREADERR\_MODEL\_I}) > 0.001). \end{aligned} \tag{4.2}$$

Both `NGMIX_CLASS` and `WAVG_CLASS` can have values of 0, 1, 2, or 3, with 0 being most star-like and 3 being most galaxy-like. Our final stellar sample used $\texttt{NGMIX\_CLASS} \leq 1$ when the composite-model fit succeeded and $\texttt{WAVG\_CLASS} \leq 1$ otherwise:

$$\texttt{STARS} = \begin{cases} \texttt{NGMIX\_CLASS} \leq 1, & \text{if } \texttt{ngmix} \text{ fit succeeds} \\ \texttt{WAVG\_CLASS} \leq 1, & \text{otherwise} \end{cases} \tag{4.3}$$

Our stellar selection was designed to yield a compromise between completeness and purity in the resulting stellar sample. In Figure 4.1 we compare our stellar classification with deeper imaging data from Hyper Suprime-Cam DR1 (Aihara et al., 2018). We find that our selection is $> 90\%$ complete for $g = 23.5$ with a galaxy contamination rising from $\lesssim 5\%$ at $g \leq 22.5$ to $\sim 30\%$ by $g \sim 23.5$. Throughout the paper we refer to the objects passing the selection in Equation (4.3) as stars.

We constrained our stellar sample to the range $16 < g < 23.5$. The bright-end limit was imposed to avoid saturation effects from bright stars, while at the faint end we seek to avoid spurious density fluctuations resulting from inhomogeneous survey depth and galaxy contamination. Since we are primarily interested in Main Sequence (MS) and Red Giant Branch (RGB) stars associated with old, metal-poor stellar populations, we constrain our sample to the color range, $0.0 < g - r < 1.0$.

In contrast to previous DES photometric calibration techniques (Drlica-Wagner et al., 2015, 2018), no stellar locus regression adjustment was applied to the DES Y3A2 zeropoints derived by the FGCM. Instead, we followed the procedure described in DES Collaboration et al. (2018) to account for interstellar dust extinction. We started with $E(B-V)$ values from the reddening map of Schlegel et al. (SFD; 1998). We computed fiducial interstellar extinction coefficients, R_b, for each band so that the corrections to the top-of-the-atmosphere calibrated source magnitudes are $A_b = E(B-V) \times R_b$. Fiducial coefficients are derived using the Fitzpatrick (1999) reddening law with $R_V = 3.1$ and the Schlafly & Finkbeiner (2011) adjusted reddening normalization parameter, $N = 0.78$. We integrated over the DES standard bandpasses considering a fixed source spectrum that is constant in spectral flux density per unit wavelength. The resulting multiplicative coefficients for the g and r band

are $R_g = 3.185$ and $R_r = 2.140$.[4] Throughout this paper, all magnitudes refer to extinction corrected PSF magnitudes derived by `ngmix`.

We build a high-resolution map of the DES survey coverage to account for missing survey coverage at the boundary of the footprint and gaps associated with saturated stars, bleed trails, and other instrumental signatures. We follow the procedure described in Drlica-Wagner et al. (2018) to transform a vectorized representation of the survey coverage calculated by `mangle` (Hamilton & Tegmark, 2004; Swanson et al., 2008) into a `HEALPix` (Górski et al., 2005) coverage fraction map. In each `nside` = 4096 ($\sim 0.74\,\mathrm{arcmin}^2$) `HEALPix` pixel, we oversample the `mangle` map by a factor of 64 to quantify the simultaneous coverage in the *griz* bands. The `HEALPix` nested pixelization scheme makes it trivial to degrade the resolution of this coverage fraction map by summing the coverage fraction of all high resolution pixels nested within a lower resolution pixel. We restrict our stream search to regions where the *griz* detection fraction is greater than 50%, resulting in a total solid angle of $4946\,\mathrm{deg}^2$. Throughout this paper, all coordinates refer to J2000 epoch.

4.3 Analysis

4.3.1 Matched-Filter Selection

We searched for stellar streams using an unweighted matched-filter algorithm in color-magnitude space (Rockosi et al., 2002; Grillmair, 2006; Bonaca et al., 2012; Jethwa et al., 2017). Our matched-filter is based on the synthetic isochrone of an old, $\tau = 13\,\mathrm{Gyr}$, metal-poor, $Z = 0.0002$ ([Fe/H] $= -1.9$), stellar population as constructed by Dotter et al. (2008) and implemented in `ugali` (Bechtol et al., 2015; Drlica-Wagner et al., 2015). We selected

4. An update to the DECam standard bandpasses changed these coefficients by < 1 part per 1000 for the DR1 release (DES Collaboration et al., 2018).

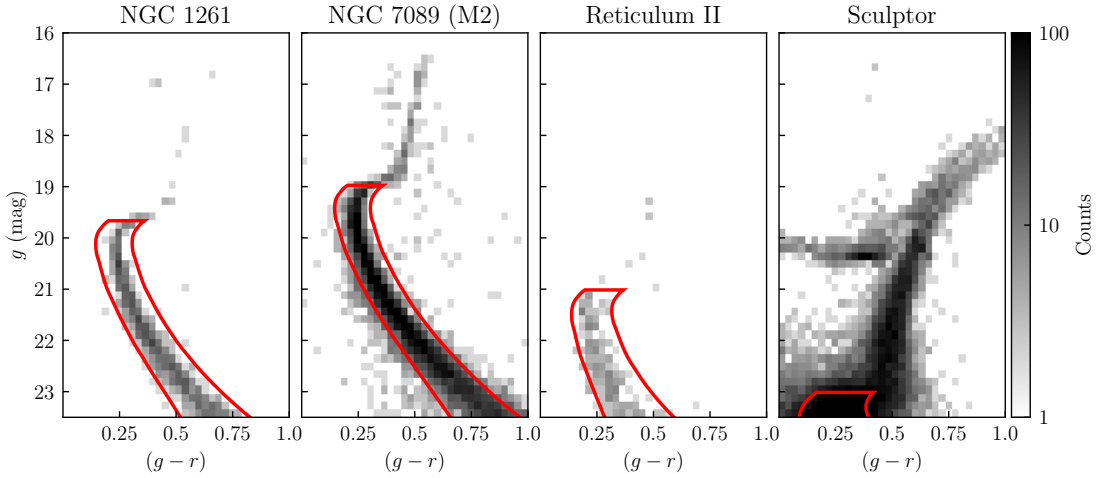

Figure 4.2 Binned color-magnitude diagram of DES Y3A2 stellar sources selected around the globular clusters NGC 1261 and NGC 7089 (M2), the ultra-faint dwarf galaxy Reticulum II, and the classical dwarf galaxy Sculptor. For the two globular clusters, data are selected in an annulus with $0.^{\circ}07 < r < 0.^{\circ}12$. Stellar sources are selected within $r < 0.^{\circ}15$ of Reticulum II and $r < 0.^{\circ}20$ of Sculptor. The matched-filter selection region for our stellar stream search is shown with the red outlines.

stars within a range of colors around the isochrone according to the criteria

$$\begin{aligned}(g-r)_{\rm iso}+E\times err(g_{\rm iso}+\mu+\Delta\mu/2)-C_1\\ <(g-r)<\\ (g-r)_{\rm iso}+E\times err(g_{\rm iso}+\mu-\Delta\mu/2)+C_2.\end{aligned} \tag{4.4}$$

where $(g-r)_{\rm iso}$ represents the predicted color from the synthetic isochrone at a distance modulus of $\mu = m - M$. We parametrize the magnitude-dependent spread in color due to measurement uncertainties as

$$err(g) = 0.001 + e^{(g-27.09)/1.09} \tag{4.5}$$

where the normalization coefficients were derived from fitting the median photometric error as a function of magnitude in the g band (`PSF_MAG_G` vs. `PSF_MAG_ERR_G`). We parameterize the selection region around the isochrone with a symmetric magnitude broadening, $\Delta\mu$,

an asymmetric color broadening, $C_{1,2}$, and a multiplicative factor for broadening based on photometric uncertainty, E. We set the values $\Delta\mu = 0.5$, $C_{1,2} = (0.05, 0.10)$ and $E = 2$ by comparing to the color-magnitude diagrams (CMDs) of old, metal-poor globular clusters and dwarf galaxies (Figure 4.2).

In Figure 4.2 we show our matched-filter selection over-plotted on binned CMDs from the globular clusters NGC 1260 and NGC 7089 (M2), the ultra-faint dwarf galaxy Reticulum II, and the classical dwarf galaxy Sculptor. Our selection retains $\gtrsim 90\%$ of stellar sources fainter than the MSTO in an annulus of $0.^{\circ}07 < r < 0.^{\circ}12$ around NGC 1260 and NGC 7089. This is a conservative estimate of the true efficiency of our selection, since it does not account for contamination from Milky Way foreground stars within this annulus.

In our initial search for stellar streams in Y3A2, we applied our matched-filter isochrone selection over a grid of distance moduli from $14 < m - M < 19$ spaced at intervals of $\Delta(m-M) = 0.3$. This spacing between distance modulus steps was chosen so that sequential isochrone selections overlap by $\gtrsim 75\%$ to insure that streams at intermediate distance moduli were detectable (Grillmair, 2017a). For each distance modulus, we binned stars passing our matched-filter selection into equal-area `HEALPix` pixels with area of $\sim 0.013\,\mathrm{deg}^2$ (`nside` = 512). We divided the number of stars selected in each `HEALPix` pixel by a map of the coverage fraction at equivalent resolution to produce a coverage-corrected map of stellar density. We smoothed the density maps with a 2-dimensional Gaussian symmetric beam with $\sigma = 0.^{\circ}3$.[5] We later repeated this procedure at spacings of $\Delta(m - M) = 0.1$ and confirmed that all stream candidates were still detected. We show the smoothed density map after the isochrone selection in Figure 4.3.

Matched-filters are often weighted by the ratio of the density of stars in color-magnitude space between a target stellar population and the background population (e.g., Rockosi et al., 2002). However, this weighting disrupts the Poisson distributed nature of the counts and

5. `http://healpy.readthedocs.io/en/latest/generated/healpy.sphtfunc.smoothing.html`

does not account for changes in the foreground and background stellar populations across the footprint (e.g., close to the Galactic disk, LMC, or Sagittarius stream). For these reasons, we perform an unweighted matched-filter search, where stars are simply accepted or rejected based on their location in color-magnitude space (e.g. Erkal et al., 2017). As a validation, we repeated our search following the procedure of Rockosi et al. (2002) to build a matched-filter isochrone from the CMDs of the globular cluster NGC 7089 and the average Milky Way foreground population. We apply an additive factor of $\Delta(m-M)$ to shift the CMD of NGC 7089 in distance modulus and thus select for stellar populations over a range of distances. We find that this procedure yields very similar results to our primary unweighted synthetic isochrone selection technique, and all stream candidates reported here were detected by both analyses.

4.3.2 Stream Detection

The Sagittarius ($l, b \sim 160^\circ, -60^\circ$), ATLAS ($l, b \sim -130^\circ, -80^\circ$), Phoenix ($l, b \sim -70^\circ, -65^\circ$), and Tucana III ($l, b \sim -45^\circ, -55^\circ$) streams are clearly visible in smoothed density maps (Figure 4.3). To further increase our sensitivity to faint stellar streams, we created a smooth model for the stellar foreground and mis-classified background galaxies. We mask the dense stellar regions around the Sagittarius stream, the LMC, and the Galactic plane (Figure 4.4) and fit a 2-dimensional, 5th-order polynomial to the distribution of smoothed stellar counts. We subtracted this model from the stellar density to create smooth maps of the residual stellar density (Figure 4.4). Visual inspection of the foreground-subtracted residual density maps served as the primary technique for identifying new streams.

To facilitate the detection of faint streams, we repeated the procedure described above to generate residual stellar density maps for a range of isochrone selections with distance moduli between $14 \leq m - M \leq 19$ in steps of $\Delta(m - M) = 0.3$. We assembled these sequences of residual density maps into animations of the isochrone-selected stellar density as a function

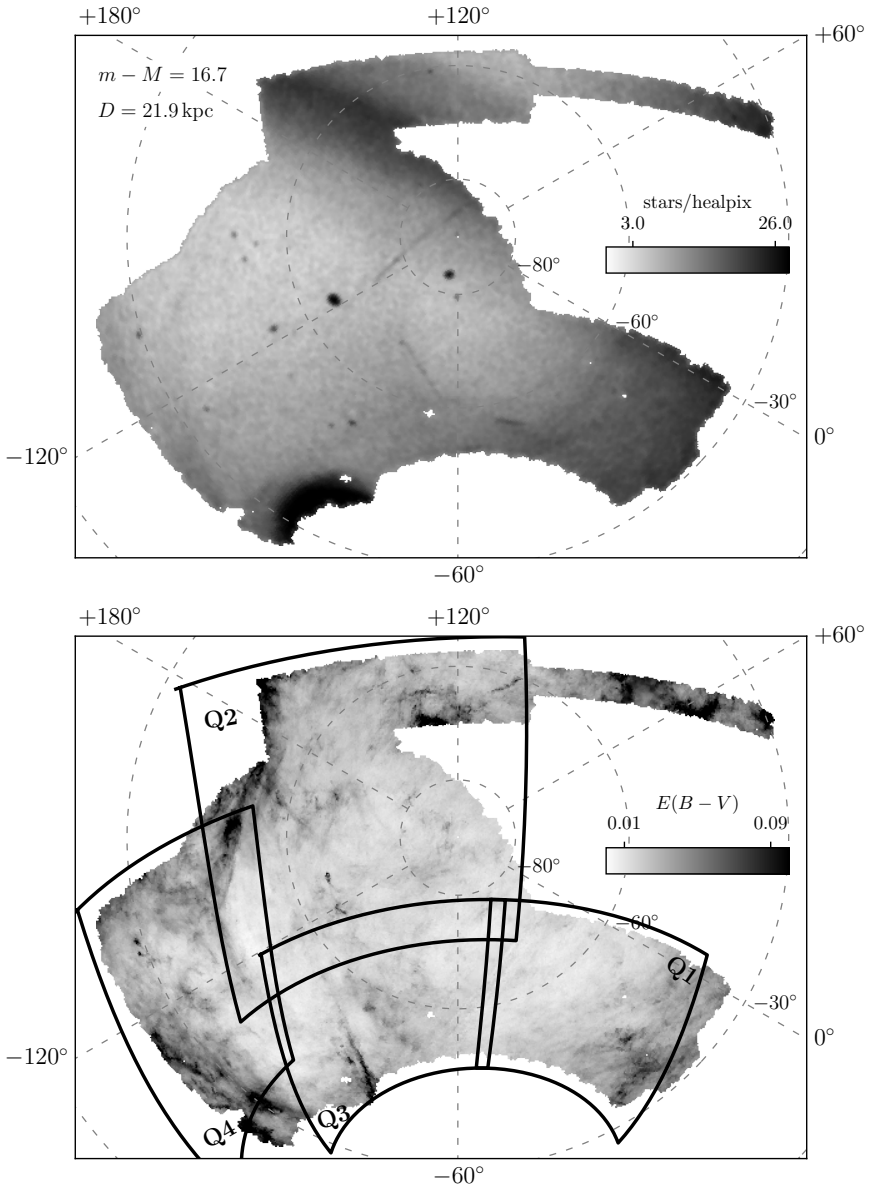

Figure 4.3 (Top) Density of stars passing the matched-filter isochrone selection at a distance modulus of $m - M = 16.7$. Stars are pixelized into equal-area `HEALPix` pixels with area of $\sim 0.013\,\mathrm{deg}^2$ (`nside` = 512). Contributions from the LMC (lower left), Sagittarius stream (top center), and Galactic thick disk (lower right) can be clearly seen. (Bottom) Interstellar extinction, $E(B-V)$, estimated by Schlegel et al. (1998). Outlines of the four DES "quadrants" defined in Section 4.4 are overplotted. Both panels are plotted in Galactic coordinates using a polar Lambert equal-area projection. An animated version of this figure can be found online at this url.

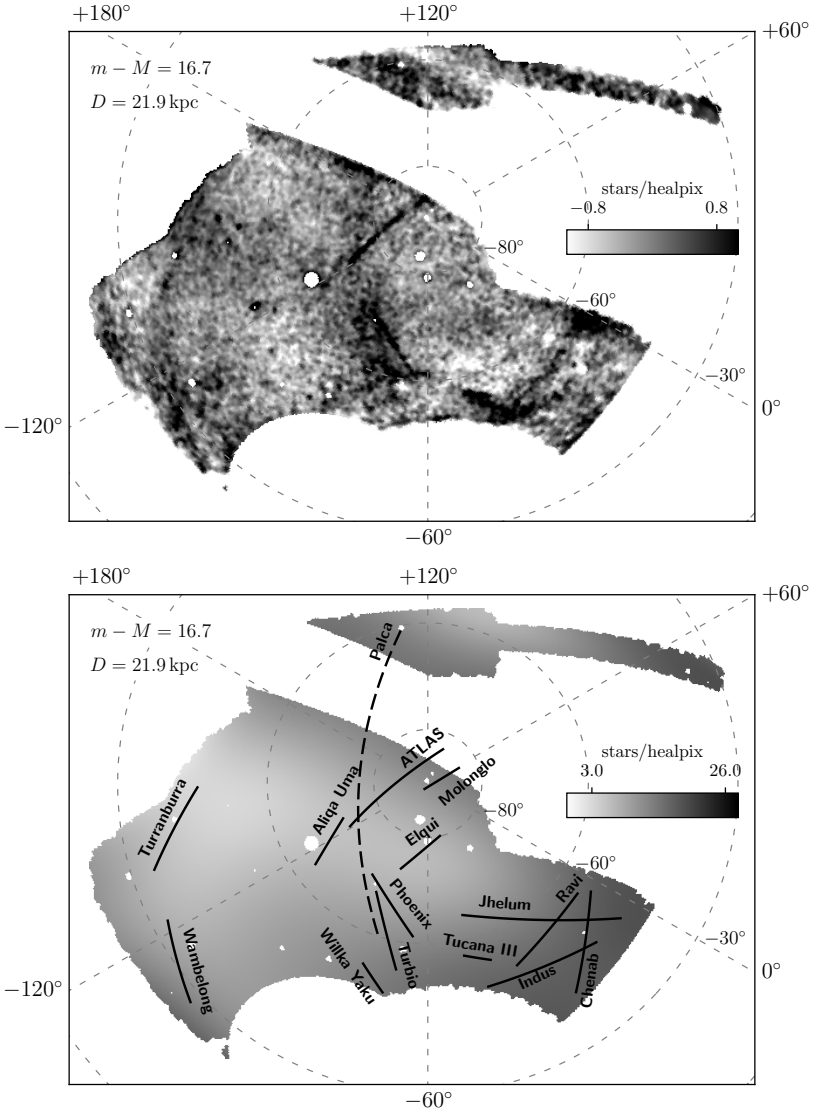

Figure 4.4 (Top) Residual density of stars passing the matched-filter isochrone selection at a distance modulus of $m-M = 16.7$. Regions around the LMC (lower left), Sagittarius stream (top center), and the Galactic disk (lower right) have been masked to improve the quality of the polynomial background fit. In addition, small regions ($r < 1^\circ$) around bright Milky Way globular clusters, satellite galaxies, and Local Group galaxies have been masked. (Bottom) Smooth background fit to the stellar density using a 2-dimensional, 5th-order polynomial (gray-scale) . Stellar streams labeled and overplotted. Palca and ATLAS are traced by a second order polynomials (Sections 4.4.2 and 4.4.5, respectively), while other streams are traced by great circle arcs. Both panels are plotted in Galactic coordinates using a polar Lambert equal-area projection. An animated version of this figure can be found online at this url.

of heliocentric distance. We required that stellar stream candidates appear in the residual density maps for at least two sequential distance moduli. The animations associated with Figure 4.3 and Figure 4.4 contain a wealth of information about stellar structure in the Milky Way halo. In this paper we specifically focus on the the most prominent stellar streams, leaving other studies of the outer halo to future work.

We perform our visual search by assembling residual density maps of the full DES footprint and in smaller subregions, which we call "quadrants". Candidates identified in the residual density maps were further examined in color-magnitude space for evidence of a stellar population distinct from the Milky Way foreground (Section 4.3.3). Only candidates that showed a distinct stellar locus consistent with an old, metal poor isochrone were included in our list of stellar stream candidates. This search resulted in the detection of the four previously known narrow stellar streams (ATLAS, Phoenix, Tucana III, and Molonglo) and eleven new stream candidates. We report the measured and derived parameters of our stream candidates in Tables 4.1 and 4.2. and discuss each candidate in more detail in Section 4.4.

Table 4.1. Measured parameters of stellar streams

Name	End Points (α, δ) (deg)	Great Circle Pole (α, δ) (deg)	Length (deg)	Width (deg)	$m - M$	Age (Gyr)	Z	N_*	Significance
Tucana III	$(-6.3, -59.7), (3.2, -59.4)$	$(354.2, 30.3)$	4.8	0.18	17.0	13.5	0.0001	700	17.0
ATLAS	$(9.3, -20.9), (30.7, -33.2)$	$(74.3, 47.9)$	22.6	0.24	16.8	11.0	0.0007	1600	13.9
Molonglo	$(6.4, -24.4), (13.6, -28.1)$	$(62.3, 51.0)$	7.4	0.32	16.8	13.5	0.0010	700	5.2
Phoenix	$(20.1, -55.3), (27.9, -42.7)$	$(311.2, 14.0)$	13.6	0.16	16.4	13.0	0.0004	700	11.1
Indus	$(-36.3, -50.7), (-8.0, -64.8)$	$(24.8, 21.6)$	20.3	0.83	16.1	13.0	0.0007	9700	21.4
Jhelum	$(-38.8, -45.1), (4.7, -51.7)$	$(359.1, 38.2)$	29.2	1.16	15.6	12.0	0.0009	4600	18.6
Ravi	$(-25.2, -44.1), (-16.0, -59.7)$	$(53.2, 11.7)$	16.6	0.72	16.8	13.5	0.0003	2300	10.3
Chenab	$(-40.7, -59.9), (-28.3, -43.0)$	$(255.5, 14.4)$	18.5	0.71	18.0	13.0	0.0004	1700	15.1
Elqui	$(10.7, -36.9), (20.6, -42.4)$	$(64.0, 38.5)$	9.4	0.54	18.5	12.0	0.0004	700	18.4
Aliqa Uma	$(31.7, -31.5), (40.6, -38.3)$	$(94.5, 36.7)$	10.0	0.26	17.3	13.0	0.0004	400	9.1
Turbio	$(28.0, -61.0), (27.9, -46.0)$	$(297.8, -0.1)$	15.0	0.25	16.1	13.0	0.0004	1000	7.9
Willka Yaku	$(36.1, -64.6), (38.4, -58.3)$	$(316.0, 4.7)$	6.4	0.21	17.7	11.0	0.0006	600	7.1
Turranburra	$(59.3, -18.0), (75.2, -26.4)$	$(123.5, 53.3)$	16.9	0.60	17.2	13.5	0.0003	1300	14.4
Wambelong	$(90.5, -45.6), (79.3, -34.3)$	$(328.7, -27.3)$	14.2	0.40	15.9	11.0	0.0001	500	5.9
Palca	$(30.3, -53.7), (16.2, 2.4)$	$(286.6, -9.9)$	57.3	...	17.8	13.0	0.0004	...	...

Note. — Measured characteristics of stellar streams detected in DES Y3A2 data. The first section reports DES measurements of previously known streams, while the second section reports narrow streams discovered by DES. The broad stream/stellar overdensity, Palca, is given its own section. Endpoints and great circle poles are reported in Equatorial coordinates and are derived from the residual stellar density analysis described in Section 4.3.2. Stream lengths are calculated as the angular separation between endpoints, while stream widths, w, come from the standard deviation of a Gaussian fit to the transverse stream profile. Distance moduli, ages, and metallicities were calculated by fitting a Dotter et al. (2008) isochrone to the Hess diagrams described in Section 4.3.3. The number of stars is calculated by summing MS stars in the background-subtracted Hess diagram. The significance is calculated as the signal-to-noise ratio between the on-stream and off-stream regions.

4.3.3 Stream Characterization

After candidates are identified in the residual density images, we perform an iterative process to fit the characteristics of each stream:

1. Define stream endpoints from the residual density maps.
2. Fit the transverse stream width to define an "on-stream" region.
3. Fit isochrone parameters to the CMD of on-stream minus off-stream stars.
4. Re-fit the transverse stream width using the best-fit isochrone selection.

We describe each of these steps in more detail below.

We defined the endpoints of each stream from the residual stellar density map. The residual stellar density map has a pixel scale of $\sim 0\overset{\circ}{.}1$ (`nside` = 512) and is smoothed by a Gaussian kernel with standard deviation $\sigma = 0\overset{\circ}{.}3$. For narrow, prominent streams the endpoints can be measured with an accuracy of better than $0\overset{\circ}{.}1$; however, for fainter and/or more diffuse structures, measuring endpoints becomes more uncertain. The stream length reported in Table 4.1 was calculated as the angular separation between the endpoints assuming that the streams follow a great circle on the sky.

For each stream, we calculate the pole of a great circle passing through the endpoints and rotate into a coordinate system where the fundamental plane is aligned with the long axis of the stream. Following the convention of Majewski et al. (2003), we define (heliocentric) longitudinal and latitudinal coordinates (Λ, B) for the rotated coordinate system associated with each stream.

As an initial estimate for the width of each stream, we rotate the `HEALPix` pixels of our raw and residual density maps into the frame of each stream. We then sum the content of `HEALPix` pixels along the transverse stream dimension to provide the transverse stream profile. We fit the transverse stream profile with a linear foreground component and a Gaussian stream model with free normalization and standard deviation. The standard deviation of the best-fit Gaussian was taken as an estimate of the stream width, and was used to define signal and

Table 4.2. Derived parameters of stellar streams

Name	Distance (kpc)	Length (kpc)	Width (pc)	Stellar Mass (10^3 $M_\odot$)	M_V (mag)	μ_V (mag arcsec^{-2})	Progenitor Mass (10^4 $M_\odot$)
Tucana III	25.1	2.1	79	3.8	-3.8	32.0	8
ATLAS	22.9	9.0	96	7.4	-4.5	33.0	12
Molonglo	22.9	3.0	128	3.5	-3.7	33.0	30
Phoenix	19.1	4.5	53	2.8	-3.6	32.6	3
Indus	16.6	5.9	240	34.0	-6.2	31.9	650
Jhelum	13.2	6.7	267	13.0	-5.1	33.3	1300
Ravi	22.9	6.6	288	10.4	-5.0	33.4	520
Chenab	39.8	12.9	493	18.3	-5.7	34.1	780
Elqui	50.1	8.2	472	10.4	-4.9	34.3	320
Aliqa Uma	28.8	5.0	131	2.3	-3.4	33.8	18
Turbio	16.6	4.3	72	3.5	-3.9	32.6	10
Willka Yaku	34.7	3.9	127	4.6	-4.1	32.9	14
Turranburra	27.5	8.1	288	7.6	-4.7	34.0	180
Wambelong	15.1	3.7	106	1.6	-3.0	33.7	26
Palca	36.3	36.3	...	...	...	...	...

Note. — Derived physical parameters of stellar streams detected in DES Y3A2 data. Heliocentric distances are calculated by fitting a Dotter et al. (2008) isochrone to the Hess diagrams described in Section 4.3.3 and have an error of $\sim 20\%$. Other physical parameters are derived from the measured parameters in Table 4.1 assuming this distance. Stream lengths are calculated from the angular distance between the stream endpoints, while the widths represent the standard deviation of the best-fit Gaussian. Stellar masses, absolute magnitudes, and surface brightnesses are derived from the richness of the best-fit isochrone model assuming a Chabrier (2001) IMF. The absolute magnitude is derived from the DES g and r bands following the prescription of Bechtol et al. (2015). The surface brightness is derived assuming that 68% of the luminosity is contained within the stream width of $\pm w$. The progenitor masses are estimated using the results of Erkal et al. (2016b).

Table 4.3. Galactocentric parameters of stellar streams

Name	x_1, y_1, z_1 (kpc)	x_2, y_2, z_2 (kpc)	$\overline{\mathrm{R_{GC}}}$ (kpc)	(ϕ, ψ) (deg)
Tucana III	$(2.7, -9.4, -20.5)$	$(0.8, -10.2, -21.1)$	23	$(285.9, 64.6)$
ATLAS	$(-8.5, 2.8, -22.7)$	$(-11.7, -5.6, -22.0)$	25	$(157.3, 68.5)$
Molonglo	$(-6.9, 2.1, -22.8)$	$(-8.3, -0.5, -22.9)$	24	$(152.3, 72.7)$
Phoenix	$(-4.5, -8.3, -16.7)$	$(-8.4, -6.4, -17.9)$	20	$(235.4, 60.6)$
Indus	$(2.9, -2.6, -12.0)$	$(-0.6, -7.3, -12.7)$	14	$(321.3, 72.0)$
Jhelum	$(0.9, -0.8, -9.4)$	$(-4.3, -4.0, -11.9)$	11	$(298.6, 83.1)$
Ravi	$(4.7, -1.4, -18.8)$	$(3.4, -7.9, -18.0)$	20	$(350.6, 75.4)$
Chenab	$(18.9, -12.5, -26.3)$	$(15.5, -1.5, -31.9)$	35	$(28.7, 68.0)$
Elqui	$(-2.4, -6.3, -49.4)$	$(-5.2, -13.9, -48.0)$	50	$(159.6, 89.9)$
Aliqa Uma	$(-13.4, -6.7, -27.6)$	$(-13.5, -11.4, -26.0)$	31	$(171.2, 66.0)$
Turbio	$(-5.0, -9.0, -13.5)$	$(-7.8, -6.3, -15.4)$	18	$(208.7, 57.3)$
Willka Yaku	$(-1.5, -21.4, -26.4)$	$(-4.7, -20.0, -28.1)$	34	$(229.7, 56.9)$
Turranburra	$(-24.6, -9.8, -19.9)$	$(-23.6, -16.6, -15.8)$	33	$(155.3, 47.5)$
Wambelong	$(-12.3, -12.8, -6.9)$	$(-15.0, -10.7, -8.3)$	20	$(183.1, 28.1)$
Palca	$(-4.6, -17.5, -31.6)$	$(-19.8, 13.8, -31.5)$	38	$(205.8, 69.5)$

Note. — Galactocentric parameters of stellar streams detected in DES Y3A2 data. Transformation into Galactocentric coordinates performed assuming the Earth resides at $(8.3\,\mathrm{kpc}, 0, 0)$. The Galactocentric azimuthal and polar angles, (ϕ, ψ), are defined as in Fig. 1 of Erkal et al. (2016b). Both endpoints are assumed to be at the heliocentric distance quoted in Table 4.1.

background regions for the color-magnitude analysis in the following section. We repeated this procedure after selecting stars consistent with the best-fit isochrone to derive the final stream width.

Stream candidates were examined in color-magnitude space to confirm the presence of a distinct stellar population matched to an old, metal poor isochrone. An "on-stream" region was selected along the great circle connecting the stream endpoints. For most streams, this region had a width of $\pm 2w$, where w is the stream width derived from the standard deviation of the best-fit Gaussian. Two "off-stream" regions were selected with the same shape as the on-stream region, but offset perpendicular to the stream axis by $\pm 4w$. In some cases this on-stream and off-stream geometry was impossible due to the boundary of the survey or the presence of large resolved stellar populations (e.g., other streams, large dwarf galaxies, etc.). The precise on- and off-stream regions selected for each stream are described in Table 4.A.1. When building on- and off-stream regions, we excise regions around known globular clusters and dwarf galaxies to avoid contaminating the CMD analysis. We calculate the effective solid angle of each region accounting for the excised regions and incomplete survey coverage using the maps described in Section 4.3.1. We binned the stars in the on-stream region in color-magnitude space with bin size $\Delta g = 0.167$ mag and $\Delta(g - r) = 0.04$ mag. We calculated the effective foreground contribution in each bin of the CMD using the off-stream regions and correcting the difference in effective solid angle. Hess diagrams were smoothed by a 0.75 pixel Gaussian kernel, and the resulting smooth residual color-magnitude diagram was examined for the presence of a distinct stellar population.

We performed a binned maximum-likelihood fit of the smoothed two-dimensional background-subtracted Hess diagrams using a synthetic isochrone from Dotter et al. (2008) weighted by a Chabrier (2001) initial mass function (IMF). We built a binned Poisson likelihood function for the observed number of stars in each CMD bin given the number of stars predicted by our isochrone model convolved by the empirically determined photometric measurement

uncertainties (Section 4.2). We simultaneously fit the richness, distance modulus, age, and metallicity of the isochrone model to the observed excess counts in the Hess diagram. The richness is a normalization parameter representing the total number of stream member stars with mass $>0.1\,M_\odot$ (Bechtol et al., 2015). For roughly half the stream candidates, the data were unable to reliably constrain all four parameters simultaneously, and we fixed the age ($\tau = 13\,\mathrm{Gyr}$) and metallicity ($Z = 0.0004$) while fitting richness and distance modulus. Furthermore, we note that there is a significant degeneracy between the age, metallicity, and distance modulus. We estimate a systematic uncertainty on the distance modulus of $\sigma(m-M) \sim 0.4\,\mathrm{mag}$, while spectroscopic observations are essential to break the degeneracy between age and metallicity.

Several streams, specifically those closer to the Galactic plane, suffer from over- or under-subtraction due to gradients in the surrounding stellar density. Mis-subtraction will bias estimates of the richness and total luminosity. To mitigate these issues, we estimate the stellar content of each stream based on the number of MS stars within a region around the best-fit isochrone. We apply a narrow isochrone selection based on Equation (4.4) using the best-fit age, metallicity, and distance modulus (Table 4.1) and the selection parameters $\Delta\mu = 0.5$, $C_{1,2} = (0.05, 0.05)$, and $E = 1$.[6] We sum the content of the background-subtracted Hess diagram within this selection region. We then correct the number of stars for the fraction of the stream width contained in the spatial selection region, to estimate the total number of MS stream stars within the spatial and magnitude range of DES. We record this value as N_* in Table 4.1. We then use the isochrone model along with a Chabrier (2001) IMF to estimate to total stellar mass, luminosity, and absolute magnitude in Table 4.2.

We re-fit the stream width after applying an isochrone selection consistent with the best-fit isochrone. We also calculate the statistical significance of each stream from the on- and area-corrected off-stream regions, $S \equiv (\mathrm{on} - \mathrm{off})/\sqrt{\mathrm{off}}$. Note that Poisson statistics are valid

6. We find that this selection is 67% efficient for stars in the globular cluster NGC 7089 (M2). This efficiency is taken into account when calculating the richness and stellar mass.

in this case due to our use of an unweighted matched-filter. For consistency, all on-stream regions had a width of $\pm w$ for this calculation. We report the measured parameters of each stream in Table 4.1 and derived physical parameters in Table 4.2. In addition, we use this absolute magnitude to calculate an average surface brightness, which we estimate assuming 68% of the luminosity is contained within $\pm w$ of the stream axis.

In Table 4.2 we also provide estimates of the progenitor masses. We use the relation between the stream width and the progenitor mass derived in Erkal et al. (2016b). More precisely, we use Equation (27) from Erkal et al. (2016b), where the progenitor mass is given in terms of the stream width as viewed from the galactic center, and the enclosed mass of the Milky Way at the stream's location. For the mass of the Milky Way, we use the best fit model in McMillan (2017) who used a range of data to constrain the Milky Way potential. We then use GALPOT (Dehnen & Binney, 1998) to evaluate the circular velocity (and hence the enclosed mass), as a function of Galactocentric radius. We note that this method assumes that the streams are on a circular orbit and only works on average for streams on eccentric orbits (Erkal et al., 2016b). Furthermore, this method also assumes that the streams have not fanned out significantly due to being in a non-spherical potential (Erkal et al., 2016b; Pearson et al., 2015). As such, this method should be seen as giving a rough estimate of the progenitor mass.

In Table 4.3 we present stream parameters in Galactocentric coordinates, assuming that the Sun is located 8.3 kpc from the Galactic center (de Grijs & Bono, 2016; Gillessen et al., 2009). Galactocentric Cartesian coordinates are provided for endpoints of each stream assuming the heliocentric distance derived in Table 4.2. We provide longitude and co-latitude (ϕ, ψ) for the pole of a Galactocentric orbit passing through the endpoints of each stream.[7] Assuming a single heliocentric distance for each stream naturally introduces a gradient in the Galactocentric radius. We use the average Galactocentric radius when calculating Galac-

7. Our definition of ϕ and ψ conforms to Figure 1 of Erkal et al. (2016b).

tocentric great-circle orbits. These Galactocentric parameters are primarily used to identify potential associations in Section 4.5.1.

4.4 Stellar Stream Candidates

As part of our search for stellar streams, we divided the DES footprint into four "quadrants" (Q1 – Q4). These quadrants were designed to be large enough to fully contain streams spanning $> 20^\circ$, while providing a more detailed view than maps of the full footprint could offer. These quadrants offer a useful unit to subdivide the DES stellar stream candidates and we discuss each quadrant in turn. We choose to name our stellar stream candidates after aquatic terms used by the geographically distinct cultures of India (Q1), Chile (Q2 and Q3), and Australia (Q4).

4.4.1 First Quadrant[8]

The first quadrant (Q1) covers the western portion of the DES footprint from $-45^\circ \lesssim \alpha \lesssim 10^\circ$ and $-65^\circ \lesssim \delta \lesssim -40^\circ$. While the DES data extend to $\alpha \gtrsim -55^\circ$, the low-order polynomial background fit has difficulty modeling the rapidly varying stellar density at these lower Galactic latitudes. Q1 includes the Tucana III satellite and stream, the two most prominent new stellar streams, Indus and Jhelum, and two lower significance streams, Chenab and Ravi. In addition, diffuse stellar overdensities are found at the northern $(\alpha, \delta \sim -28^\circ, -42^\circ)$ and southern $(\alpha, \delta \sim -10^\circ, -63^\circ)$ edges of Q1; however, the footprint boundary makes it difficult to perform a quantitative evaluation of these structures.

8. Due to overlap with the constellation Indus, which shares a name with a Pakistani and Indian river, and to honor the tradition of astronomy in the region, new stellar stream candidates in this quadrant are named after rivers in Pakistan and India (including the Indus River itself).

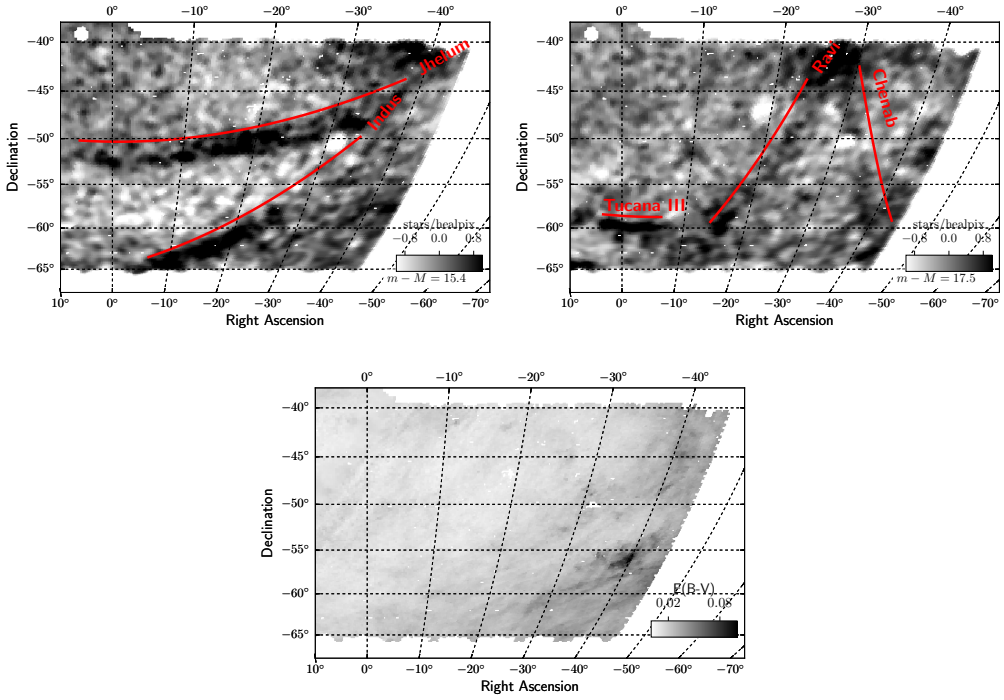

Figure 4.5 Residual stellar density map in Q1 after subtracting a smooth background model from the distribution of isochrone filtered stars (equal area McBryde-Thomas flat-polar quartic projection). Streams are marked with great circles that are aligned with the major axis of the stream and offset perpendicularly by 1.°5. (Top) Isochrone selection with $m - M = 16.4$. (Middle) Isochrone selection with $m - M = 17.5$. (Bottom) Interstellar reddening, $E(B-V)$, from Schlegel et al. (1998). An animated version of this figure can be found online at this url.

Tucana III Stream

The Tucana III stellar stream is located at a distance of $\sim 25\,\mathrm{kpc}$, extending at least $\pm 2^\circ$ from the ultra-faint satellite Tucana III (Drlica-Wagner et al., 2015). We find that Tucana III appears prominently in the Q1 residual density maps with a projected length of 5° extending from $(-6.^\circ 3, -59.^\circ 7)$ to $(3.^\circ 2, -59.^\circ 4)$ (Figure 4.5).

In Figure 4.6, we show a Hess diagram calculated by subtracting a local background estimate derived from off-stream regions on either side of the Tucana III stream. Despite a well-defined MS and visible RGB, our likelihood analysis has trouble simultaneously fitting the richness, distance modulus, age, and metallicity of the Tucana III stream. Assuming a distance modulus of $m - M = 17.0$ and a metallicity of $Z = 0.0001$ ([Fe/H] $= -2.24$) from Drlica-Wagner et al. (2015), we find that the MSTO of Tucana III is well-described by an age of $\tau = 13.5\,\mathrm{Gyr}$. This is older than the $\tau = 10.9\,\mathrm{Gyr}$ reported by Drlica-Wagner et al. (2015), which is due in part to a correction to the synthetic isochrones using an updated version of the DECam filter throughput (Li et al., 2018). In addition, the change in photometric calibration between the DES Y2Q1 and Y3A2 data sets is found to introduce a small color shift.

Spectroscopic observations have been unable to conclusively classify Tucana III as an ultra-faint galaxy or star cluster (Simon et al., 2017). The unresolved velocity dispersion ($\sigma_v < 1.5\,\mathrm{km\,s^{-1}}$ at 95.5% confidence) and metallicity spread ($\sigma_{[\mathrm{Fe/H}]} < 0.19$ at 95% confidence) are both low for an ultra-faint dwarf galaxy. However, the mean metallicity ([Fe/H] $= -2.42^{+0.07}_{-0.08}$) and large physical size ($\mathrm{r}_{1/2} = 44 \pm 6$ pc) are both unusual for a globular cluster. In addition, Simon et al. (2017) argue that the mass-to-light ratio of the core of Tucana III is larger than that of a globular cluster, $M/L > 20\,\mathrm{M}_\odot/\,\mathrm{L}_\odot$, based on its proximity to the Galactic center and the non-detection of a velocity gradient out to 90 pc. The core of Tucana III lies slightly offset from the luminosity-metallicity relationship for ultra-faint galaxies (Kirby et al., 2013). Simon et al. (2017) note that if Tucana III has been

stripped of $\sim 70\%$ of its stellar mass, then it would lie directly on the metallicity-luminosity relation of ultra-faint dwarfs. We find that the total stellar mass of the Tucana III stream, including the core and the tidal tails, is $3.8 \times 10^3\,\mathrm{M}_\odot$, which is 4.75 times the stellar mass of the Tucana III core (Drlica-Wagner et al., 2015). This corresponds to a mass loss of 79%, which moves the Tucana III progenitor system onto the luminosity-metallicity relationship for dwarf galaxies.

We search for indications of a distance gradient following a similar procedure to that applied to the Sagittarius stream by Koposov et al. (2012). We transform to a coordinate system oriented along the stream axis and divide the stellar counts into 8 longitudinal bins. Within each longitudinal bin, we examine the mean magnitude of MSTO stars satisfying the criteria $0.20 < (g - r) < 0.24$. We find that the mean magnitude of the MSTO changes from $g \sim 16.75$ at the western end of the stream to $g \sim 17.19$ on the eastern end. Fitting a linear gradient model to these data yields a distance gradient of $0.16 \pm 0.06\,\mathrm{mag\,deg^{-1}}$. This measurement implies that the Tucana III stream spans $\sim 4\,\mathrm{kpc}$ in distance with a total physical extent of $\sim 4.5\,\mathrm{kpc}$ and that it is on a radial orbit.

Indus Stream

Indus is the first of 4 new stellar stream candidates detected in Q1. Indus has an angular extent of $20\overset{\circ}{.}3$ with a projected width of $0\overset{\circ}{.}83$. It may extend beyond the southern edge of the DES footprint in the direction of the SMC; however, at a best-fit distance of 16.6 kpc ($m - M = 16.1$), it is unlikely that there is a physical association between the Indus stream and the Magellanic Clouds (located ~ 3 times farther away). The physical width of the Indus stream, $\sigma = 240\,\mathrm{pc}$ (FWHM = 565 pc), is comparable to that of the Orphan stream (FWHM = 688 pc; Belokurov et al., 2007a), and considerably larger than known globular cluster streams. There is no obvious progenitor for Indus (Section 4.5.1); however, its width may indicate that the Indus stream is the disrupted remains of a faint dwarf galaxy.

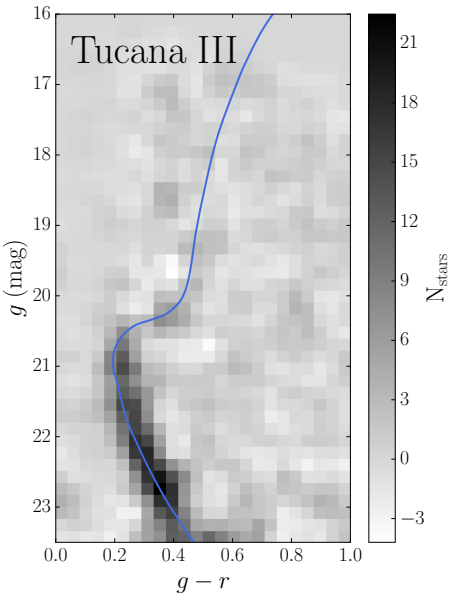

Figure 4.6 Background-subtracted binned color-magnitude Hess diagram for stars associated with the Tucana III stellar stream. The background is estimated from an off-stream region parallel to the stream and is area corrected and subtracted from the on-stream region. The Hess diagram is smoothed with a 2D-Gaussian kernel with a standard deviation of 0.75 pixels. Darkly colored pixels correspond to higher residual stellar density while lighter pixels represent underdense regions in color-magnitude space. A synthetic isochrone from Dotter et al. (2008) is over-plotted with best-fit parameters described in Table 4.1. The isochrone fitting procedures are described in Section 4.3.3 and Section 4.4.

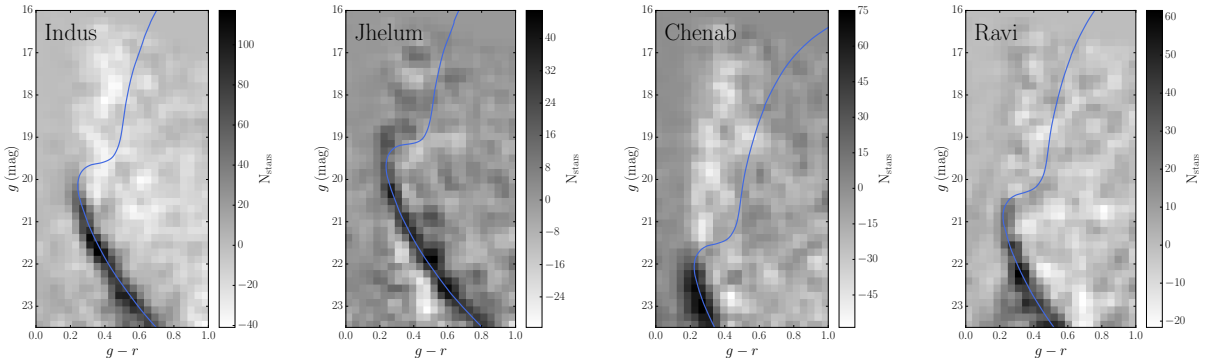

Figure 4.7 Hess diagrams for Indus (far left), Jhelum (center left), Chenab (center right), and Ravi (far right) stellar stream candidates in DES quadrant one. Over-plotted in each panel is a Dotter et al. (2008) synthetic stellar isochrone with parameters determined from the best-fit in Table 4.1. These panels are similar to Figure 4.6.

The MS of the Indus stream is seen prominently in color-magnitude space (Figure 4.7), with an estimated absolute magnitude of $M_V = -6.2$ (Table 4.2). The measured metallicity of the Indus stream, $Z = 0.0007$ ([Fe/H] $= -1.4$), is considerably higher than would be expected for a dwarf galaxy with similar luminosity (Kirby et al., 2013). The proximity of the Galactic bulge makes it difficult to model the stellar foreground in the vicinity of Indus, and it is possible that foreground contamination in the RGB of Indus may be artificially inflating the measured metallicity (an even more pronounced example can be seen in Jhelum).

The southern portion of the Indus stream becomes confused with a more distant diffuse stellar structure ($m - M \geq 16.5$) that extends towards the Tucana III stream. Due to the incomplete southern coverage of DES, we cannot determine whether this is the signature of another stream or a diffuse stellar cloud. Other DECam imaging in the regions of the Magellanic Clouds – e.g. the Survey of the Magellanic Stellar History (SMASH; Nidever et al., 2017) and the Magellanic Satellites Survey (Drlica-Wagner et al., 2016; Pieres et al., 2017, MagLiteS;) – may be able to clarify this question in the near future. However, kinematic information will be necessary to test for any physical connection between Indus/Tucana III and this putative diffuse structure.

Jhelum Stream

The Jhelum stream is comparable to Indus in width, $w = 1\overset{\circ}{.}16$, and due to its orientation on the sky, a longer portion of the stream is contained within the DES footprint ($L \sim 29\overset{\circ}{.}2$). At a distance of 13.2 kpc ($m - M = 15.6$), Jhelum is closer than Indus; however, both streams can be detected by our isochrone selection simultaneously for distance moduli $15.0 \lesssim m - M \lesssim 16.2$. The average physical width of Jhelum is 267 pc, though narrowing is seen at the eastern end of the stream. While Jhelum appears curved in Figure 4.5, the observed curvature is well-matched by a great circle on the sky.

The Hess diagram for the Jhelum stream shows a prominent MS, but also shows some

foreground contamination above the MSTO as well as some evidence of over-subtraction. In order to reduce contamination, we selected a narrower on-stream region of width $\pm w$. Additionally, to reduce the impact of Galactic foreground stars, we first fit the richness, distance modulus, age, and metallicity using just the eastern portion of the stream (higher Galactic latitude). We fix the age and metallicity at the best-fit values from this initial fit and then refit the richness and distance modulus using the full extent of the stream. Similar to Indus, we find a high metallicity, $Z = 0.0009$, which is likely influenced by foreground contamination.

The physical similarity and proximity of the Indus and Jhelum streams is suggestive of a possible physical connection between the two streams. To investigate the possibility that Indus and Jhelum may be different orbital arms of the same progenitor, we transformed both into Galactocentric coordinates (Table 4.3). We find that the two streams are at a similar Galactocentric radius, $R_{\rm GC} \sim 11 - 13\,{\rm kpc}$, but that the Galactocentric great-circle orbits have poles that differ by $\sim 22^\circ$. For a flattening $q = 0.9$ and an initial polar angle $\psi = 75^\circ$, the expected precession after one orbit is $\Delta\phi \sim -10^\circ$ Erkal et al. (2016b). This suggests that if Indus and Jhelum are associated with the same progenitor, that progenitor has experienced a more highly asymmetric gravitational potential. Such precession is possible if the progenitor is on an eccentric orbit that takes it close to the Galactic plane, or if the Milky Way halo is more heavily flattened than previously expected. Additional kinematic information is necessary to confirm or refute this hypothesis.

Ravi Stream

The Ravi stream candidate is a tenuous feature detected in Q1. It extends from the lower region of the DES footprint up to the Q1 northern overdensity described in Section 4.4.1. The Ravi stream crosses the Tucana II dwarf galaxy in projection; however, a fit to the Hess diagram in Figure 4.7 puts it at less than half the distance. Due to its higher Galactic

latitude and orientation nearly parallel to the Galactic plane, the CMD of Ravi appears considerably cleaner than some of the other streams in this quadrant, with a pronounced main sequence, and less indication of foreground contamination at bright magnitudes. We report the best-fit the age, metallicity, and distance modulus in Table 4.1.

Chenab Stream

The Chenab stream candidate runs nearly perpendicular to Indus and Jhelum, but at a significantly larger distance of 39.8 kpc ($m - M = 18.0$). Like the other new streams in this quadrant, Chenab has a large angular size, $0\overset{\circ}{.}71$, and a physical width of $\sigma = 493$ pc. The measured extent of Chenab is $18\overset{\circ}{.}5$ (12.9 kpc). The analysis of the Chenab stream is complicated by contamination from Milky Way foreground.

Chenab intersects a diffuse stellar overdensity near the northern edge of the DES footprint. This overdensity spans from $-32^\circ \lesssim \alpha \lesssim -22^\circ$ and $-45^\circ \lesssim \delta \lesssim -40^\circ$ and is apparent in the residual density maps selected for isochrones between $17 < m - M < 19$. It is possible that this overdensity could be an extended spur of the Sagittarius stream, the ridge line of which passes $\sim 11^\circ$ from the northwest corner of the DES footprint at a heliocentric distance of ~ 25 kpc ($m - M \sim 17$) (Majewski et al., 2004; Law et al., 2005).

4.4.2 Second Quadrant[9]

The second quadrant (Q2) spans from $0^\circ < \alpha \lesssim 60^\circ$ and $-42^\circ < \delta < 7^\circ$ (Figure 4.8). This quadrant contains the Sagittarius stream, which we have masked from our analysis in order to increase our sensitivity to fainter new streams. We detect 4 narrow streams in this region, including the previously known ATLAS (Koposov et al., 2014) stream and a possible extension of the Molonglo (Grillmair, 2017a) stream, and two newly detected streams that

9. To honor the long astronomical tradition in Chile (home of the Blanco telescope), we name stellar streams in Q2 and Q3 after Chilean rivers and aquatic terms in native Chilean tongues. Aliqa Uma is the Aymara term for "peaceful water" and Willka Yaku is the Quechua term for "sacred water."

we name Elqui and Aliqa Uma. In addition, we find a long, diffuse structure that extends along the height of Q2 intersecting the Eridanus-Phoenix stellar overdensity lower in the DES footprint (Li et al., 2016). We name this structure the Palca stream and discuss it in more detail in Section 4.4.5.

ATLAS Stream

The ATLAS stream is a narrow stellar stream discovered in the first data release of the VST ATLAS survey, which covered a declination slice around the stream from $-37^\circ \lesssim \delta \lesssim -25^\circ$ to a limiting magnitude of $r \sim 22$ (Koposov et al., 2014). The ATLAS stream was later studied by Bernard et al. (2016) using the larger sky coverage provided by Pan-STARRS. The DES analysis is deeper than both VST ATLAS and Pan-STARRS, $g = 23.5$, and extends the sky coverage around ATLAS to lower declinations. The ATLAS stream does not appear to extend significantly beyond the length described by Koposov et al. (2014), ending at $(\alpha, \delta) \sim (30\overset{\circ}{.}7, -33\overset{\circ}{.}2)$. At higher declination it becomes difficult to disentangle the ATLAS stream from the much more luminous Sagittarius stream before hitting the boundary of the DES footprint at $(\alpha, \delta) \sim (9\overset{\circ}{.}3, -20\overset{\circ}{.}9)$. Using Pan-STARRS data, Bernard et al. (2016) have extended ATLAS to $\delta \sim -15^\circ$ leading to a total length of $\sim 28^\circ$, of which $22\overset{\circ}{.}6$ is contained within DES.

We follow the procedure described in Section 4.3.2 to characterize the physical properties of the ATLAS stream. The deeper DES data prefer a slightly larger distance of 22.9 kpc ($m - M \sim 16.8$), which is marginally consistent with the previously measured distance, 20 ± 2 kpc, derived using the VST ATLAS data (Koposov et al., 2014). At a distance of 22.9 kpc, the visible portion of the ATLAS stream extends 9.0 kpc. We independently fit the distance modulus to each half of the ATLAS stream and find evidence that the southwestern portion of ATLAS has a distance modulus that is ~ 0.3 mag larger than the northeastern portion. The southwestern portion of ATLAS is detectable in the residual

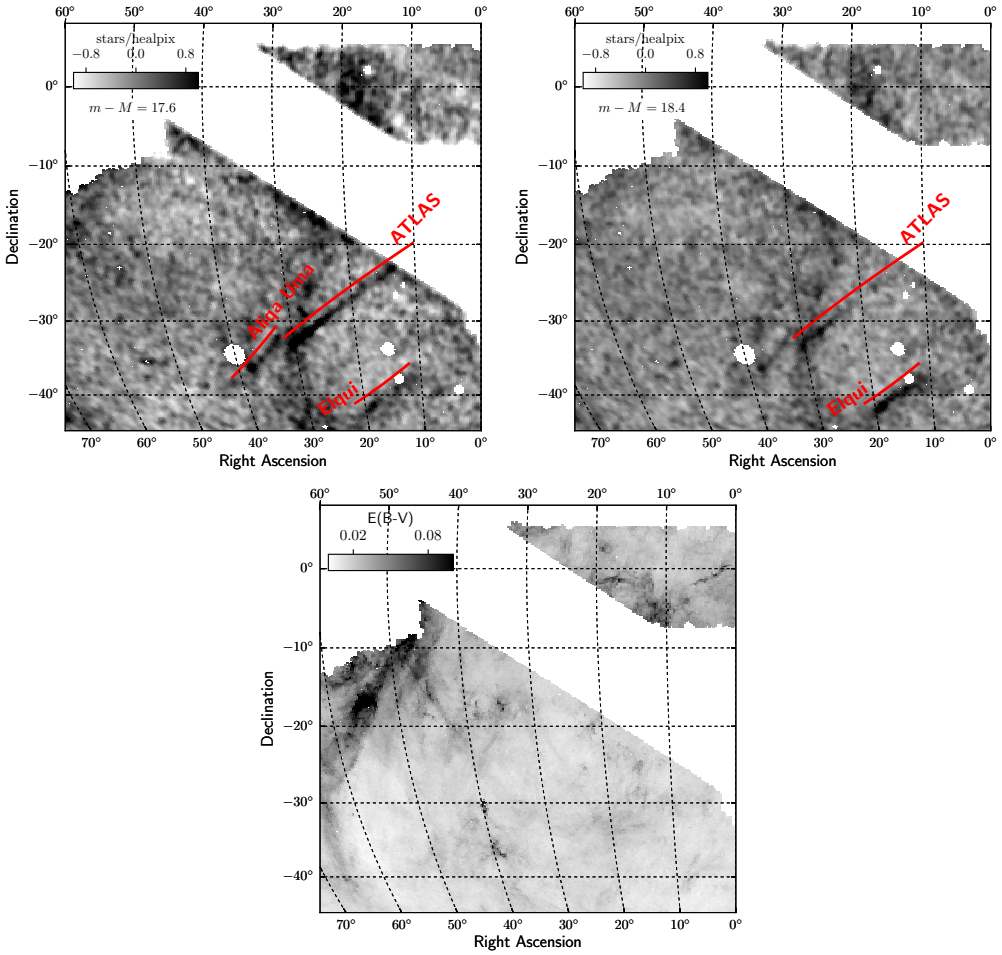

Figure 4.8 Residual density maps in Q2 (similar to Figure 4.5). The Sagittarius stream has been masked to optimize the search for faint stellar streams. The Fornax ($\alpha, \delta = 40\overset{\circ}{.}0, -34\overset{\circ}{.}4$) and Sculptor ($\alpha, \delta = 15\overset{\circ}{.}0, -33\overset{\circ}{.}7$) dwarf galaxies have been masked along with several globular clusters and Local Group galaxies. (Left) The residual density map for $m - M = 16.4$ showing the ATLAS and Aliqa Uma streams, with a hint of the Elqui stream. (Middle) The residual density map for $m - M = 18.4$. The Elqui stream appears prominently, while the southeastern portion of ATLAS is still visible. Molonglo has a relatively high metallicity (Z=0.001) and is therefore not visible with this selection. (Right) Interstellar reddening, $E(B-V)$, from Schlegel et al. (1998). An animated version can be found online at this url.

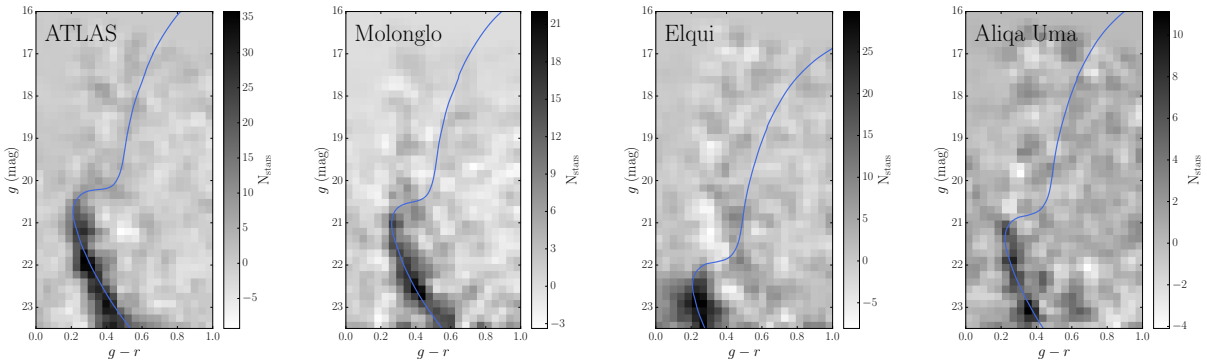

Figure 4.9 Hess diagrams for the ATLAS (far left), Molonglo (center left), Elqui (center right), and Aliqa Uma (far right) stream candidates in DES quadrant two (Q2). Overplotted in each panel is a Dotter et al. (2008) synthetic stellar isochrone with parameters determined from the best-fit in Table 4.1. These panels are similar to Figure 4.6.

density maps at distance modulus of $m - M > 18.0$. The stellar density is not uniform along the length of ATLAS and we note a roughly spherical overdensity in the southwestern portion at $(\alpha, \delta) = (25\overset{\circ}{.}37, -30\overset{\circ}{.}13)$. This overdensity is visible at lower significance in Figure 1 of Koposov et al. 2014. The DES data suggest a fainter absolute magnitude for the ATLAS stream, $M_V = -4.5$, compared to that estimated in the VST ATLAS data, $M_V \sim -6$ (Koposov et al., 2014).

Figure 4.10 shows the spatial distribution of stars in a coordinate system aligned with the endpoints of the ATLAS stream. Following the procedure described in Section 4.3.3, we fit the width of the ATLAS stream with a Gaussian model on top of a linear background. Our measured width of the ATLAS stream, $w = 0\overset{\circ}{.}24$, is consistent with $w = 0\overset{\circ}{.}25$ reported by Koposov et al. (2014), where w corresponds to the Gaussian standard deviation. However, it is also clear in Figure 4.10 that the ATLAS stream deviates appreciably from a great circle on the sky, which would lie along the equator. We find that the ridgeline of the ATLAS stream is well-described over the range $9\overset{\circ}{.}3 < \alpha < 30\overset{\circ}{.}7$ by a second-order polynomial of the form

$$\delta = -15.637 - 0.545(\alpha) - 0.001(\alpha)^2. \tag{4.6}$$

Interestingly, Figure 4.10 also appears to show an underdensity in the stream at $\Lambda \sim 4^\circ$ which is approximately $2.^\circ5$ in size. We caution that this underdensity occurs in a region where the polynomial background fit is complicated by the proximity of the Sagittarius stream. Over-subtraction of the background could manifest as an underdensity in the residual map. To check for the reality of this gap, we also analyzed the raw isochrone-selected counts without any background subtraction and found that in this region there is in fact a deficit with respect to the mean stream density. While the existence of this underdensity remains uncertain, if it is real it could be due to perturbations by subhalos around the Milky Way (e.g. Ibata et al., 2002; Johnston et al., 2002). Erkal et al. (2016a) estimated the typical size and number of gaps in the ATLAS stream due to subhalos and found a characteristic gap size of $\sim 4^\circ$ with 0.1 gaps expected. However, this prediction depends on the length and orbital trajectory of the ATLAS stream, and therefore given the increased length of the ATLAS stream detected in this work and in Pan-STARRS (Bernard et al., 2016), as well as the uncertainty in its trajectory, the predicted number of gaps is likely an underestimate. If the underdensity is confirmed then the gap can be used to infer the properties of the subhalo which created the gap (Erkal & Belokurov, 2015b) and the statistical properties of the stream density can be used to place constraints on the number of subhalos in the Milky Way (Bovy et al., 2017).

Molonglo Stream

The Molonglo stream was identified as a faint, narrow feature in data from Pan-STARRS (Grillmair, 2017a). We extrapolate Equation (2) from Grillmair (2017a) to detect a narrow, $\sim 8^\circ$ extension of the Molonglo stream in the DES data offset by $\lesssim 2^\circ$. Molonglo is the only stream that is detected based on prior information from another survey and there is some risk of confirmation bias. In fact, Molonglo is the least apparent feature in the residual density maps, due in part to its proximity to the Sagittarius stream. However, the Hess diagram

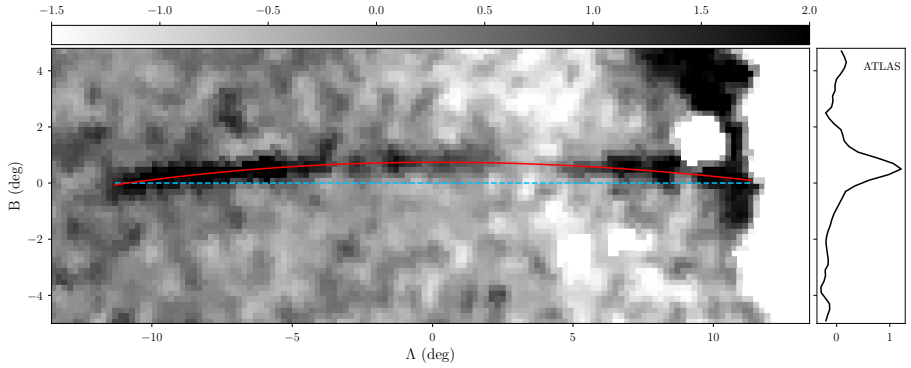

Figure 4.10 Residual stellar density along the ATLAS stream for a distance modulus selection of $m - M = 16.8$. Both the stellar counts and background model have been smoothed by a Gaussian kernel with width $0.^{\circ}3$. The ATLAS stream has noticeable curvature, which can be seen by comparing the best-fit second-order polynomial from Equation (4.6) (red solid line) to the plane of a great circle on the sky (blue dashed line).

for Molonglo shows a clear MS and MSTO (Figure 4.9), and the stream has a detection significance of 5.2σ. After fixing the age ($\tau = 13.5\,\mathrm{Gyr}$) and metallicity ($Z = 0.0010$) to match the Hess diagram, we fit the distance modulus and richness of Molonglo. We determine a distance of 22.9 kpc ($m - M = 16.8$), which agrees with the estimated distance of 20 kpc from Grillmair (2017a). However, the foreground subtraction in this region is difficult, and the remaining contamination may have artificially inflated the metallicity. Our best-fit width of $0.^{\circ}32$ is narrower than the $\sim 0.^{\circ}5$ reported by Grillmair (2017a); however, it is unclear whether his width was measured after convolving with a $0.^{\circ}4$ Gaussian kernel. We do not find evidence of the other three streams identified by Grillmair (2017a).

Elqui Stream

At a heliocentric distance of $D_{\odot} = 50.1\,\mathrm{kpc}$, the Elqui stream is the most distant stream discovered in the DES Y3A2 data. Fitting the southwestern and northeastern halves of Elqui independently shows a shift in distance modulus from 18.2 to 18.5, corresponding to a physical change in distance of 6.5 kpc over a length of 8.2 kpc. The Elqui stream is broad and may show slight curvature on the sky, which is unexpected for a stream at large

Galactocentric radius. The background galaxy NGC 300 resides at $(\alpha, \delta) \sim (13.^\circ7, -37.^\circ7)$, but is unrelated to the much closer Elqui stream.

Elqui resides at similar Galactocentric distance to the LMC and overlaps (in projection) the gaseous component of the Magellanic Stream (Nidever et al., 2008). Transforming to the Magellanic Stream coordinates defined by Nidever et al. (2008), the endpoints of Elqui are located at $L_{\rm MS}, B_{\rm MS} \approx (-49.^\circ1, 1.^\circ8), (-40.^\circ7, 6.^\circ1)$. The proximity between Elqui and the Magellanic Stream suggests that Elqui may in fact be stellar ejecta from a past collision between the LMC and SMC (Besla et al., 2010, 2012). Besla et al. (2012) suggests that a recent collision between the LMC and SMC could explain many of the observed features of the Magellanic system. If Elqui indeed formed as the result of such a collision, its existence could be used to further constrain the infall history of the Magellanic Clouds.

Evidence of stellar ejecta from the Magellanic Clouds is observed elsewhere in the DES footprint. The so-called "SMC northern overdensity" (Pieres et al., 2016) is located $\sim 8^\circ$ from the SMC on the southern edge of the DES footprint $(\alpha, \delta) \sim (15^\circ, -65^\circ)$ and is visible in isochrone selections with $m - M \gtrsim 18$. Establishing complete DECam coverage around the Magellanic Clouds promises additional insight into how the Magellanic Clouds have shaped the Milky Way halo.

Aliqa Uma Stream

The Aliqa Uma stream resides at the southern end of the ATLAS stream, extending from $\alpha, \delta \sim (31.^\circ7, -31.^\circ5)$ to $\alpha, \delta \sim (40.^\circ6, -38.^\circ3)$. While the northern end of this stream is in close proximity to the southern end of the ATLAS stream, the difference in orientation and distance modulus, $m - M = 17.3$, leads us to classify it as a distinct system rather than an extension of ATLAS. While this stream crosses close to the Fornax dwarf galaxy in projection, it is substantially closer and the two systems are very unlikely to be physically associated. The presence of Fornax and ATLAS bracketing the much fainter Aliqa Uma

stream makes it difficult to establish a good background selection region.

4.4.3 Third Quadrant

The third DES quadrant (Q3) covers the region from $5^\circ \lesssim \alpha \lesssim 60^\circ$ and $-65^\circ \lesssim \delta \lesssim -42^\circ$. This quadrant resides above the LMC and SMC, and overlaps heavily with the EriPhe stellar overdensity (Li et al., 2016). Several linear structures are detected in this region; however, it is difficult to conclusively differentiate them from a diffuse component of EriPhe. In addition to the Phoenix stream (Balbinot et al., 2016), we identify two new stream candidates, Turbio and Willka Yaku.

Phoenix Stream

The Phoenix stream is a narrow stellar stream discovered in the DES Y1A1 data (Balbinot et al., 2016). Since the DES analysis of the Phoenix stream is discussed in great detail in Balbinot et al. (2016), we offer only a brief discussion here. The Y3A2 data provide a deeper and more complete catalog with improved photometric accuracy; however, the qualitative characteristics of the Phoenix stream are predominantly unchanged. It remains a clumpy and knotted stream, consisting of a more-or-less symmetric distribution of overdensities. The parameters that we derive for the Phoenix stream largely agree with those of Balbinot et al. (2016). We measure a distance of 19.1 kpc ($m - M = 16.4$), which is slightly larger than the value measured previously (17.5 ± 9 kpc). Similar to Balbinot et al. (2016) we find no indication of a distance gradient.

Turbio Stream

We find a linear feature near the center of the EriPhe stellar overdensity, which constitutes a candidate stream named Turbio. While Turbio is detected above the background of EriPhe with a significance of 7.9σ, it would be very surprising if the two were not physically associ-

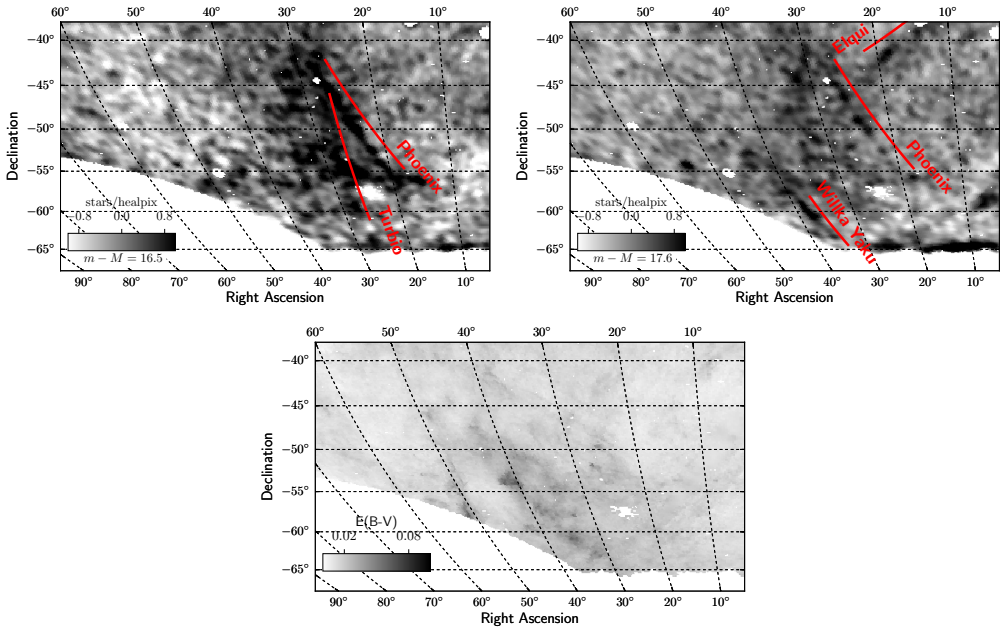

Figure 4.11 Residual density maps in Q3 (similar to Figure 4.5). (Top) An isochrone selection with $m - M = 16.5$ shows the Phoenix and Turbio streams superposed on the EriPhe overdensity. (Middle) The Willka Yaku stream can be seen in a selection for $m - M = 17.6$. (Bottom) Interstellar reddening, $E(B-V)$, from Schlegel et al. (1998). An animated version of this figure can be found online at this url.

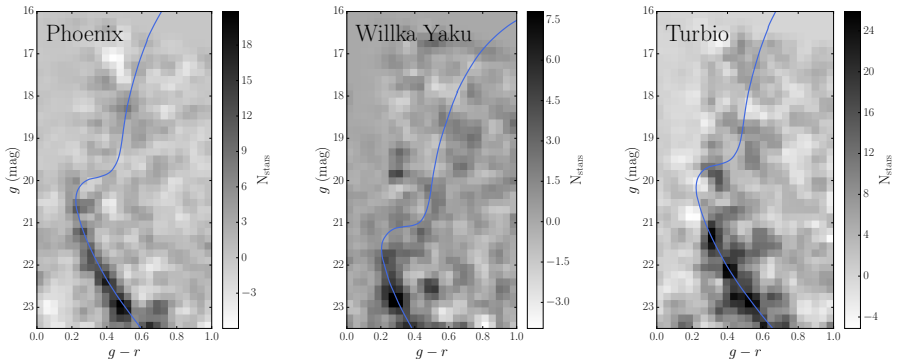

Figure 4.12 Hess diagrams for the Phoenix (left), Willka Yaku (center), and Turbio (right) streams found in DES Q3. Over-plotted in each panel is a Dotter et al. (2008) synthetic stellar isochrone with parameters determined from the best-fit in Table 4.1. These panels are similar to Figure 4.6.

ated. It is likely that Turbio stands out more prominently in our analysis compared to that of Li et al. (2016) due to improved photometric calibration ($\sim 0.7\%$ vs. $\sim 2\%$), increased depth ($g < 23.5$ vs. $g < 22.5$), and improved spatial resolution (smoothing kernel of $0\overset{\circ}{.}3$ vs. $0\overset{\circ}{.}5$).

The MS of Turbio is detected in a Hess diagram that subtracts a neighboring region of EriPhe to the east of the structure (Figure 4.12). We fit an isochrone with fixed age and metallicity ($\tau = 13.0\,\mathrm{Gyr}$, $Z = 0.0004$) and find a best-fit distance modulus of $m - M = 16.1$, which is indistinguishable from that of EriPhe and the nearby globular cluster NGC 1261. Li et al. (2016) suggest that EriPhe may have a common origin with the Virgo Overdensity (Jurić et al., 2008) and the Hercules-Aquila cloud (Belokurov et al., 2007c). However, the orientation of Turbio is nearly perpendicular with the orbit necessary to connect these three diffuse structures. In addition, Turbio may constitute a dense portion of the larger Palca structure that is seen to extend northward from the EriPhe cloud.

Willka Yaku Stream

Willka Yaku is a short and relatively narrow stream that extends $\sim 6^\circ$ from the southern edge of the DES footprint. Willka Yaku sits on the south eastern boundary of the EriPhe cloud and we find a significant gradient in the stellar density transverse to the stream. To reduce the effects of foreground contamination, we fit only the more prominent northern half of the stream (Figure 4.12). A simultaneous fit of age, metallicity, and distance modulus yields a best-fit distance of 34.7 kpc ($m - M = 17.7$). This places Willka Yaku at a significantly larger distance than EriPhe, and makes a physical association less likely.

4.4.4 Fourth Quadrant[10]

The fourth quadrant of DES (Q4) spans from $60^\circ \lesssim \alpha \lesssim 95^\circ$ and $-65^\circ < \delta < -15^\circ$. It contains the globular clusters NGC 1851 and NGC 1904, and structure from the Monoceros Ring can be seen in the direction of the Galactic anti-center. The proximity of the Monoceros and the Galactic plane make background subtraction difficult near the eastern edge of this region. Inspection of the residual density maps yields two stellar stream candidates, Turranburra and Wambelong, which are reasonably wide ($w \sim 0\overset{\circ}{.}5$) and detected at moderate significance.

Turranburra Stream

The Turranburra stream stretches across the northern portion of Q4, extending from $(\alpha, \delta) = (59\overset{\circ}{.}3, -18\overset{\circ}{.}0)$ to $(\alpha, \delta) = (75\overset{\circ}{.}2, -26\overset{\circ}{.}4)$. The Hess diagram of this stream shows a prominent MS and a hint of an RGB (Figure 4.14). We estimate that this structure resides at a distance of 27.5 kpc and has a width of 288 pc. The physical width of Turranburra is more consistent with a dwarf galaxy progenitor, and the photometric estimate of metallicity of $Z = 0.0003$

10. To honor the long tradition of astronomy in Australia (stretching back tens of thousands of years), stellar stream candidates in this quadrant are named after Aboriginal terms for rivers in Australia.

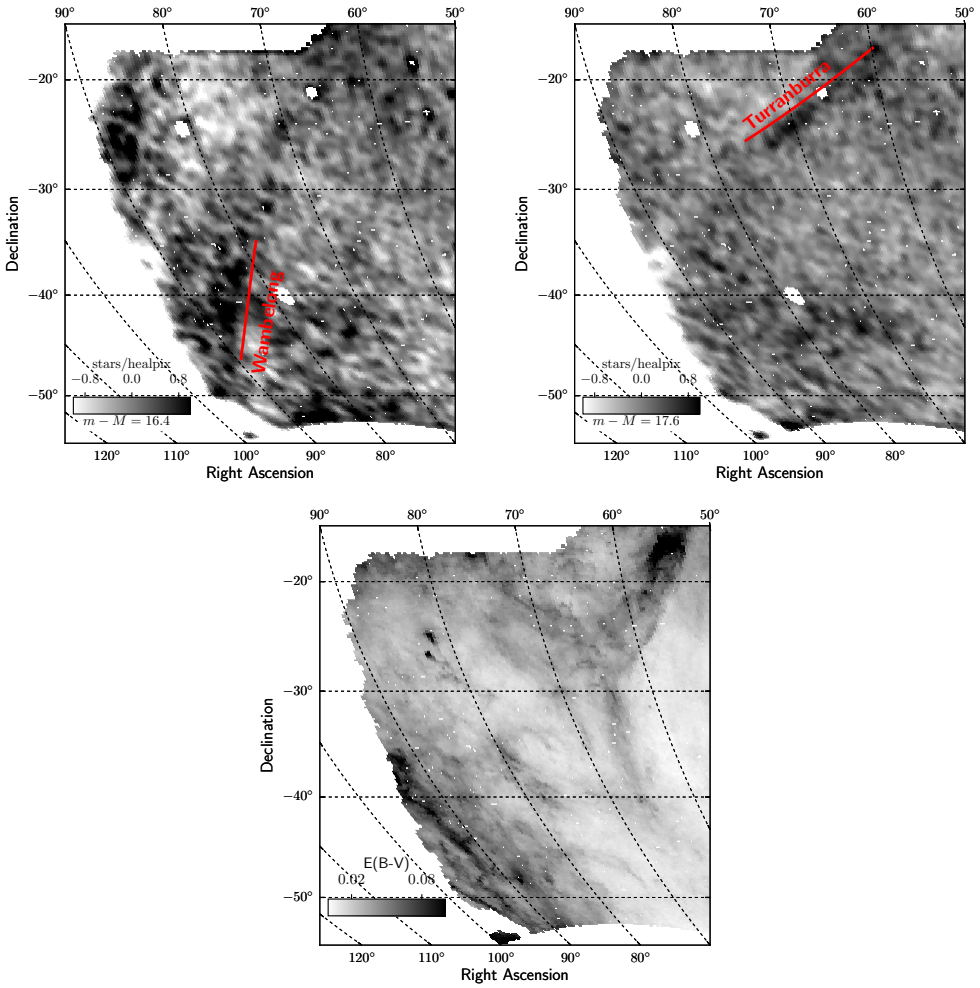

Figure 4.13 Residual density maps in Q4 (similar to Figure 4.5). (Left) Residual stellar density at $m-M = 16.4$ showing the Wambelong stream. (Middle) The Turranburra stream can be seen in a selection with $m - M = 17.6$. (Right) Interstellar reddening, $E(B - V)$, from Schlegel et al. (1998). An animated version of this figure can be found online at this url.

is comparable to photometric metallicities determined for ultra-faint galaxies (e.g., Bechtol et al., 2015). The extent of Turranburra is somewhat uncertain due to its proximity to the edge of the DES footprint and its diffuse nature, especially at its north western end. The orbit of Turranburra appears to be distinct from other known streams and globular clusters, without any obvious association or potential progenitor.

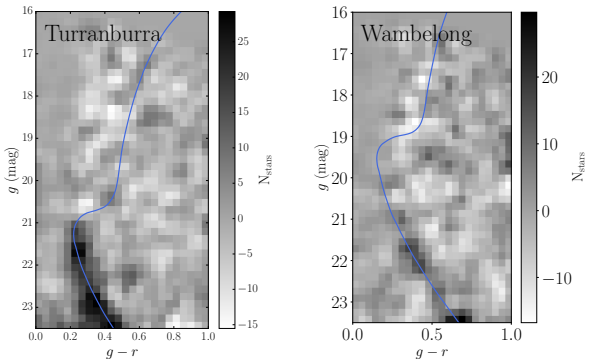

Figure 4.14 Hess diagrams for the Turranburra (left) and Wambelong (right) stream candidates found in DES quadrant four (Q4). Over-plotted in each panel is a Dotter et al. (2008) synthetic stellar isochrone with parameters determined from the best-fit in Table 4.1. These panels are similar to Figure 4.6.

Wambelong Stream

The Wambelong stream stretches northward from the eastern edge of the DES footprint, spanning $\sim 14^\circ$ from $(\alpha, \delta) \sim (90.^\circ 5, -45.^\circ 6)$ to $(\alpha, \delta) \sim (79.^\circ 3, -34.^\circ 3)$. The eastern extent of Wambelong is difficult to determine due to confusion with foreground stars associated with the Galactic anticenter and the Monoceros Ring (Newberg et al., 2002; Yanny et al., 2003). The signature of Wambelong peaks at a heliocentric distance of $\sim 15.1\,\mathrm{kpc}$ ($m - M \sim 15.9$) with no strong indication of a distance gradient. A residual overdensity at $(\alpha, \delta) \sim (70.^\circ 4, -23.^\circ 9)$ is aligned with the Wambelong stream and may suggest that this stream is nearly twice as long as our conservative estimate.

4.4.5 Diffuse Overdensities

While the search described here is optimized for $\lesssim 1^\circ$-wide stellar features, we note that we are sensitive to more diffuse stellar systems. Without the directionality of a narrow stream, interpreting the origin and physical parameters of these diffuse structures becomes much more difficult. However, we do note that the DES Y3A2 data unambiguously confirms the existence of the EriPhe overdensity (Li et al., 2016), and shows strong indications of addi-

tional substructure around or within this system. Apart from the aforementioned Phoenix, Turbio, and Willka Yaku streams, there are several lower significance linear structures that overlap EriPhe at a heliocentric distances of $\sim 16.6\,\mathrm{kpc}$ ($m - M = 16.1$). One pronounced feature runs nearly east-west with $\delta \approx -56^\circ$ (Figure 4.11). Unfortunately, image-level masking around the super-saturated star Achernar ($\alpha, \delta = 24\overset{\circ}{.}43, -57\overset{\circ}{.}24$) complicates the interpretation of the southern portion of EriPhe.

The Palca [11] stream is a broad curvilinear overdensity in the Y3A2 data that extends northward from EriPhe at $\alpha \sim 30^\circ$. Palca extends from the Turbio stream in the south to the northern boundary of the DES footprint, crossing the Sagittarius stream at $\alpha \sim 20^\circ$. Palca is more diffuse than the other streams discovered in DES Y3A2 (FWHM $\sim 2^\circ$). To increase our sensitivity to this broad feature, we convolve the residual density maps by a 1° kernel and plot in Equatorial coordinates (Figure 4.15). We find that the northern part of Palca is at a significantly larger distance, $\sim 36\,\mathrm{kpc}$ ($m - M \sim 17.8$), than EriPhe. It is unclear whether this is a signature of a distance gradient from EriPhe to Palca, or whether these are two distinct systems. Assuming that Palca spans the DES footprint (i.e., overlapping with EriPhe), the ridgeline of this structure can be approximated with a second-order polynomial of the form:

$$\alpha = 17.277 - 0.495\delta - 0.0046\delta^2. \tag{4.7}$$

The above equation is found to be valid for $-55^\circ < \delta < 2\overset{\circ}{.}5$. Palca shows appreciable curvature on the sky, suggesting that it may be in a modestly elliptical orbit. The orbital trajectory of Palca is strongly misaligned with the proposed polar orbit connecting EriPhe with the Virgo Overdensity and the Hercules-Aquila cloud (Li et al., 2016). A physical association between Palca and EriPhe would disfavor this hypothesis. However, the orbit of Palca may be broadly consistent with another scenario proposed by Li et al. (2016) suggesting that EriPhe may be the remnants of a disrupted dwarf galaxy originally associated with NGC

11. Palca is the Quechua word for "cross of rivers."

1261 and the Phoenix stream.

4.4.6 Globular Clusters

The DES Y3A2 footprint contains five classical globular clusters (NGC 288, NGC 1261, NGC 1851, NGC 1904, and NGC 7089) and four more distant clusters (Whiting 1, AM-1, Eridanus, and Reticulum). While a full investigation of globular clusters is outside the scope of the current paper, we note that our analysis is sensitive to stellar features around these clusters. Four of the classical globular classical clusters (NGC 288, NGC 1261, NGC 1851, and NGC 1904) show hints of extended stellar structure.[12] These features are detectable with the generic isochrone selection described in Section 4.3 and can be seen in the animations associated with Figure 4.4. However, to optimize our sensitivity to faint features, we built individual matched-filter selections for each cluster using the CMD of stars within an annulus of $4\farcm2 < r < 7\farcm2$ around each cluster. We create an optimal weighting by taking the ratio between the density (in color-magnitude space) of cluster member stars compared to the Milky Way foreground population averaged over the DES footprint,

$$w_{i,j} = f_{\rm gc}(i,j)/f_{\rm mw}(i,j) \tag{4.8}$$

where i, j index the color and magnitude bins, $f_{\rm gc}(i,j)$ is the normalized density of cluster stars per bin, $f_{\rm mw}(i,j)$ is the normalized density of Milky Way stars, and $w_{i,j}$ is the weighting (Rockosi et al., 2002). We mask circular regions comparable to the Jacobi radii of each cluster (Table 4.4) and convolve the selected stellar density with a Gaussian kernel with $\sigma = 0\fdg25$. We follow the same procedure to derive a global polynomial fit to the smoothed density of selected stars and create residual density maps from the difference between the data and the polynomial fit (Figure 4.16).

12. NGC 7089 (M2) is located in the narrow Stripe 82 region of the DES footprint. The narrow width of this region and the large density of foreground stars make a search for extended structure challenging.

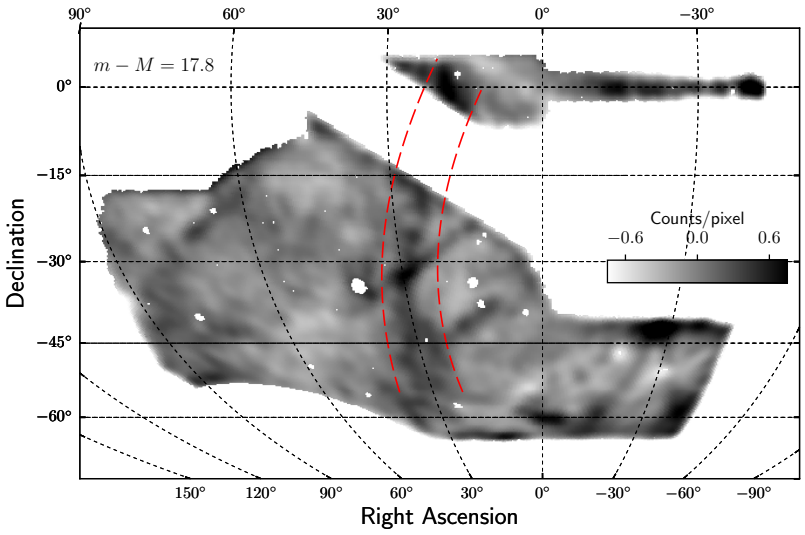

Figure 4.15 Residual density map for an isochrone selection at $m - M = 17.8$ smoothed by a 1° Gaussian kernel. The Palca overdensity (bracketed in red) runs along the north-south direction at $\alpha \sim 30°$. At low declination Palca overlaps the EriPhe stellar overdensity with roughly the same orientation as the Turbio stream. The ATLAS, Elqui, Tucana III, Chenab, Willka Yaku, and Turranburra streams are also visible in this map.

We compare the observed stellar features to predictions about orbital motion and tidal tail formation in each globular cluster. We simulated the orbits of the globular clusters using the spray-particle implementation by Küpper et al. (2012), where the escape velocity was modified to match that observed in N-body simulations with realistic tidal fields (Claydon et al., 2017). We assume a Milky Way potential similar to the best-fit Palomar 5 model (Küpper et al., 2015a), but with a Jaffe bulge. The cluster initial mass is obtained using the method outlined in Balbinot & Gieles (2018). The tidal tail formation was simulated for the last 6 Gyr of the cluster history and particles were released every 1 Myr.

The heliocentric distance, sky position, line-of-sight velocity, and integrated magnitude for each cluster was taken from Harris (updated 2010 1996). Proper motions for NGC 288 and NGC 1851 are taken from Dinescu et al. (1997), for NGC 1904 we used values from Dinescu et al. (1999), and for NGC 1261 we used values from Dambis (2006). These parameters are summarized in Table 4.4. Our simulations assumed a Galactocentric solar position of

$(8.3\,\mathrm{kpc}, 0, 0)$, a local reflex motion of $U, V, W = (11.1, 12.24, 7.25)\,\mathrm{km\,s^{-1}}$ (Schönrich et al., 2010a), and a circular solar velocity of $U, V, W = (0, 233, 0)\,\mathrm{km\,s^{-1}}$ (Küpper et al., 2015a).

NGC 288

NGC 288 is a globular cluster with a dynamical evolution that is strongly driven by tidal shocks (Gnedin & Ostriker, 1997). Grillmair et al. (1995) showed initial evidence for extra-tidal features using photographic photometry. The analysis of NGC 288 was extended to a larger field by Leon et al. (2000), who reported evidence of two sets of tidal tails, extended along the direction of motion and in the direction of the Galactic center. Subsequently, Grillmair et al. (2004) used 2MASS data to suggest a $\sim 17^{\circ}$ tidal tail; however, this claim was later refuted by Piatti (2018) using deeper data from Pan-STARRS PS1. In contrast, Piatti (2018) found evidence for clumpy extra-tidal structure extending 120 pc ($0\overset{\circ}{.}8$) from the cluster center. The DES Y3A2 data is deeper than the Pan-STARRS data analyzed by Piatti (2018) and supports previous reports of clumpy extra-tidal structure extending $\sim 1\overset{\circ}{.}5$ from the core of NGC 288. In addition, there is evidence that these extra tidal features may extend $\sim 5\overset{\circ}{.}5$ southward of NGC 288 (Figure 4.16). This structure is misaligned with the orbital motion of NGC 288 and the vector connecting NGC 288 to the Galactic center.

Table 4.4. Globular Cluster Parameters

Name	α (deg)	δ (deg)	$\mathrm{D}_{\odot}$ (kpc)	r_{J} (pc)	$\mu_\alpha \cos(\delta)$ (mas/ yr)	μ_δ (mas/ yr)
NGC 288	13.189	-26.583	76.4	8.9	4.48	-6.04
NGC 1261	48.068	-55.216	146.4	16.3	1.33	-3.06
NGC 1851	78.528	-40.047	166.5	12.1	1.29	2.38
NGC 1904	81.046	-24.525	153.8	8.9	2.12	-0.02

Note. — Centroids, heliocentric distances, Jacobi radii, and proper motions for four classical globular clusters in the DES footprint. Values taken from: Harris (1996, 2010 edition), Balbinot & Gieles (2018), Dinescu et al. (1997), Dambis (2006), Dinescu et al. (1999)

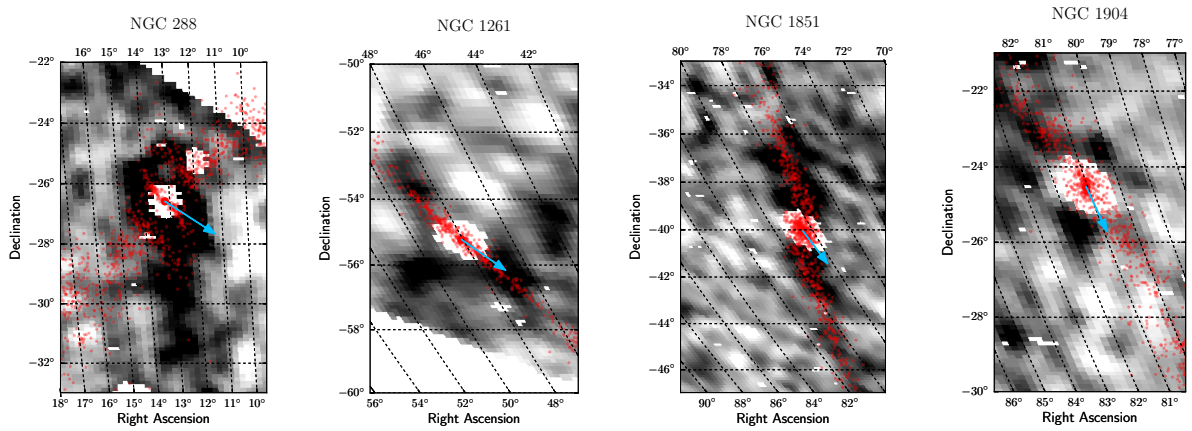

Figure 4.16 Distribution of matched-filtered stars selected around 4 globular clusters (gray-scale image). Stellar counts within the Jacobi radii of each cluster have been masked to show extra-tidal features. Star particles simulated using the spray-particle implementation of Küpper et al. (2012) are shown in red (see text for details), and the blue arrow indicates the projected 3D vector towards the Galactic center. Extra-tidal features in NGC 1261 and NGC 1851 appear aligned with the simulated orbit; however, this is not the case for the other two systems.

NGC 1261

NGC 1261 resides in the southern portion of the DES footprint and it has been suggested that it may be associated with the Phoenix stream (Balbinot et al., 2016) and/or the EriPhe stellar overdensity (Li et al., 2016). The analysis of Leon et al. (2000) suggests the existence of a tidal tail oriented in the direction of the Galactic center. Recent observations with DECam have similarly detected evidence that the stellar halo of NGC 1261 extends beyond its nominal Wilson tidal radius (Kuzma et al., 2018; Carballo-Bello et al., 2018), but do not see any evidence of tail-like structure. Our observations support the existence of extra-tidal structure around NGC 1261. While some of this structure appears to be aligned with the orbital motion of the cluster, it is difficult to draw any firm conclusion without more detailed analysis.

NGC 1851

Tidal tails were reported around NGC 1851 by Leon et al. (2000), who claimed to detect low-surface-brightness features oriented with the direction of motion of the cluster. However, Olszewski et al. (2009) found no evidence of tidal tails in a more recent analysis of deeper data. Rather, Olszewski et al. (2009) reported a low-surface-brightness extended stellar halo extending to $\sim 1\overset{\circ}{.}25$. Our residual density maps shows evidence of both an extended stellar halo around NGC 1851, and a set of faint linear features aligned with the predicted orbit (Figure 4.16). The residual stellar density extends prominently to a radius $>1^\circ$ from the cluster core, agreeing with measurements of an extended stellar halo by Olszewski et al. (2009). The linear feature extends at least 5° to the north and south of NGC 1851. The orientation of these features are well-aligned with the orbital motion of NGC 1851, suggesting that these features may be tidal tails. In fact, the animation associated with Figure 4.4 suggests that these putative tidal tails may extend $\pm 15^\circ$ or more from NGC 1851. The detection of extra-tidal structure associated with NGC 1851 agrees with recent work by Kuzma et al. (2018) and Carballo-Bello et al. (2018). The DES data greatly extend the coverage around NGC 1851, and make a strong case for a "vast stellar structure" (Carballo-Bello et al., 2018) extending both northward and southward of this cluster.

NGC 1904

An extended halo of extra-tidal stars around NGC 1904 was first recognized by Grillmair et al. (1995) and later by Leon et al. (2000). We confirm the existence of extra-tidal structure extending $\sim 1\overset{\circ}{.}5$ from the cluster center. Leon et al. (2000) suggest that the short relaxation time of NGC 1904 would cause mass segregation in the tidal tails. This may explain why these features were not seen with shallower observations. Interestingly, these structures appear to be symmetric, but are misaligned with the orbital motion of the cluster. Observations of NGC 1904 by Carballo-Bello et al. (2018) reach a similar conclusion that the stellar distribution

of this cluster deviates from the conventional King and Wilson models to fill, and slightly overflow, the Jacobi radius of the cluster.

4.5 Discussion

4.5.1 Potential Associations with Known Systems

We use the recent catalog of stellar streams compiled by Mateu et al. (2018a), augmented with the recently discovered Jet stream (Jethwa et al., 2017) to assess whether any of our stream candidates may be associated with previously detected streams located in other regions of the sky. We begin by transforming the endpoints of each stream into Galactocentric Cartesian coordinates. The ellipticity of these streams is poorly constrained so we assume only that the streams orbit in a plane around the Galactic Center. We find the pole of each stream, (ϕ, ψ), defined as the positive normal vector of a plane containing both endpoints. Uncertainties in the pole location for our newly found streams were estimated by assuming a 20% uncertainty on the heliocentric distance before converting to Galactocentric coordinates. The poles for the new and previously discovered streams are shown in Figure 4.17.

The distribution of DES stream poles shown in the left panel of Figure 4.17 is clearly non-uniform. We do not find any strong association of stream poles coinciding with the proposed Vast Polar Structure (VPOS; Pawlowski et al., 2012, 2015). Specifically, in the left panel of Figure 4.17 we plot the VPOS+new pole (Table 1 of Pawlowski et al., 2015) transformed into Galactocentric coordinates assuming a distance of 100 kpc. However, the limited sky coverage of the DES footprint will bias the observable distribution of stream poles. To estimate this bias, we generate a uniform random sample of Galactocenric great-circle orbits with a radius of 25 kpc. We calculate the fraction of each great-circle orbit contained within the DES footprint as a function of Galactocentric orbital pole and show this in the right panel of Figure 4.17. We find that the observed distribution of stream poles

is consistent with the predictions from our simple simulation. The DES footprint is clearly biased against detecting streams having poles with $\psi_{\rm pole} < 30^\circ$ and $-60^\circ < \phi_{\rm pole} < 120^\circ$. We find qualitatively similar results for random samples of orbits with Galactocentric radii of 15 kpc and 50 kpc.

To investigate potential associations for the new DES streams, we plot Galactocentric great-circle orbits for the DES streams and other known streams with similar orbital poles (Figure 4.18). Full phase-space information is necessary to definitively match between streams systems; however, we do note several tentative associations based on the photometrically measured properties of the DES streams. Figure 4.18 shows a strong correspondence between Ravi and the tentative candidate RR Lyrae stream 24.5-1 (Mateu et al., 2018a). The poles of these two stream candidates match within 3° while their distance moduli differ by $\Delta(m-M) \sim 0.2\,{\rm mag}$ (well within the systematic error associated with our isochrone fitting). Such an association supports the robustness of tentative candidates identified below the conservative $> 4\sigma$ significance threshold of Mateu et al. (2018a).

The orbital pole of the Hermus stream (Grillmair, 2014) is only $3\overset{\circ}{.}4$ from that of Willka Yaku, but the Galactocentric distances of the two streams differ by $\sim 16\,{\rm kpc}$. It has previously been suggested that Hermus may be a northern extension of the Phoenix stream (Grillmair & Carlberg, 2016), which resides along a slightly different orbital plane, but is well-matched in distance. Kinematic information would help to resolve this ambiguity.

Globular clusters and dwarf galaxies may provide possible progenitors for the newly discovered streams. The globular cluster candidate with the smallest separation is IC 4499. It is within $1\overset{\circ}{.}2$ of the great circle orbit of Turbio, and has a Galactocentric radius that differs by less than 2 kpc. IC 4499 is a moderate-mass, low-density cluster with signatures of an extra-tidal stellar halo (Walker et al., 2011). Cetus II, an ultra-faint dwarf galaxy (Drlica-Wagner et al., 2015), is another candidate for association. It lies $1\overset{\circ}{.}7$ off of the great circle orbit of Aliqa Uma, has a Galactocentric radius that is 1.1 kpc larger, and is located

43° from the nearest endpoint of the stream. We note also that the tidal tails of Palomar 5 ($R_{GC} = 18.2\,\mathrm{kpc}$) have an orbital pole within 6° of the ATLAS stream (25 kpc).

Agnello (2017) identified four stellar stream candidates overlapping the DES footprint using a WISE-Gaia multiple search. It was proposed that two of these streams, WG3 and WG4, may have associated counterparts in DES (Agnello, 2017). While WG3 and WG4 appear qualitatively similar to Indus and Jhelum, their absolute coordinates are offset by $\Delta\alpha \sim -20°$ (an angular separation of $\sim 15°$). We do not see any significant stellar overdensities associated with the positions of WG3 or WG4 reported by Agnello (2017), though their proximity to the Galactic plane and unknown distance makes it difficult to quantify the lack of a DES counterpart. If we allow $\Delta\alpha$ offsets of $\sim 10°$, then we find a possible correspondence between WG1 and Wambelong. WG1 is offset from Wambelong by $\Delta\alpha \sim -8°$ (angular separation of $\sim 6°$) and extends both northeast and southwest along a similar path. This observation provides circumstantial evidence in support of the longer extent of Wambelong proposed in Section 4.4.4. WG2 does not correspond to any of the high-significance stream candidates reported here. However, WG2 appears qualitatively similar to a lower significance feature found to the southwest of NGC 1851 extending from $\alpha, \delta = (56.1, -50.4)$ to $(78.5, -40.0)$ at a distance modulus of $m - M \sim 17.5$ (animation of Figure 4.4). We expect Gaia DR2 to greatly improve the power of stellar stream searches using astrometric techniques.

4.5.2 Milky Way Gravitational Potential

Stellar streams can be used to constrain the Milky Way gravitational potential (e.g., Johnston et al., 2005; Koposov et al., 2010; Law & Majewski, 2010; Gibbons et al., 2014; Bowden et al., 2015; Küpper et al., 2015b; Bovy et al., 2016). Full potential modeling is beyond the scope of this work; however, we note that the streams discovered by DES span a wide range of Galactocentric radii and should be able to constrain how the Milky Way's density profile

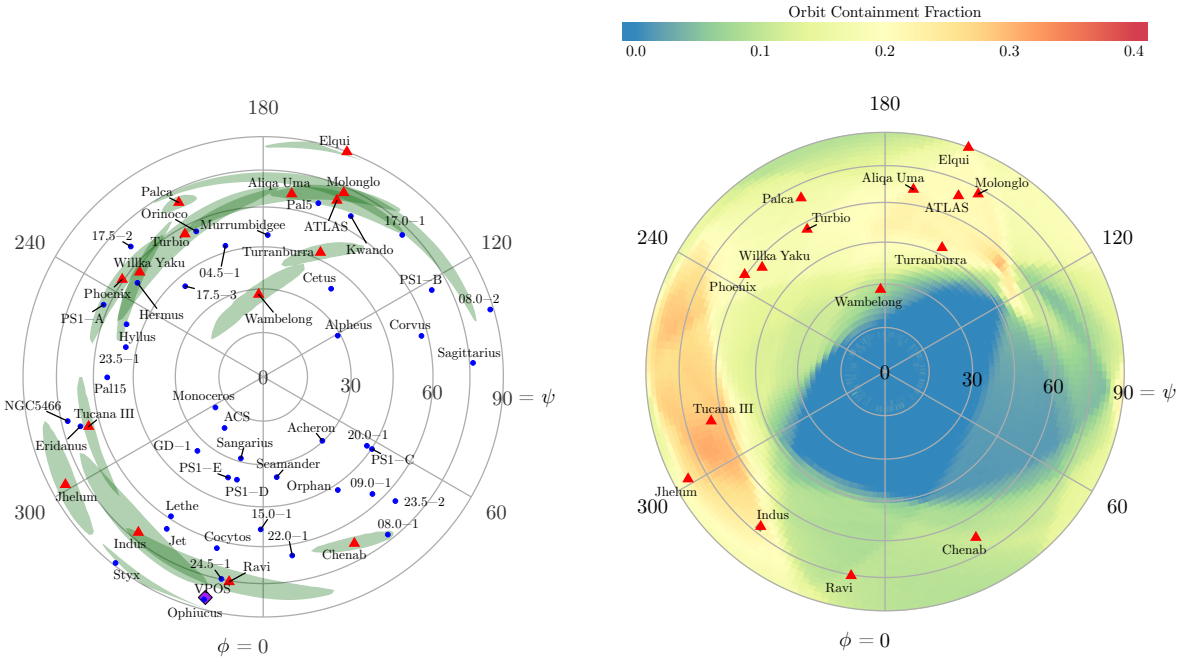

Figure 4.17 (Left) Galactocentric orbital poles for DES stream candidates (red triangles) and previously known streams (blue circles; Mateu et al., 2018a; Jethwa et al., 2017). Green shaded regions represent the 1σ uncertainty ellipses for the poles of the DES streams assuming a distance uncertainty of 20%. The purple diamond shows the mean orbital pole of the proposed vast polar structure (Pawlowski et al., 2015). (Right) The fraction of uniformly distributed Galactocentric great-circle orbits with $R_{GC} = 25\,\mathrm{kpc}$ that are contained within the DES footprint. The DES footprint imposes a geometric bias against the detection of streams with $-60^\circ < \phi_{\mathrm{pole}} < 120^\circ$ and $\psi_{\mathrm{pole}} \lesssim 30^\circ$.

and shape evolves with radius. In this context, we expect that the ATLAS stream will be especially useful since it is long and does not lie on a great circle (see Figure 4.10).

However, even without sophisticated modeling we can make some general observations in the context of the Milky Way potential. Erkal et al. (2016b) suggest that the connection between stream width and orbital inclination could provide an independent constraint on the symmetry axis and flattening of the Milky Way halo. In Figure 4.19, we plot the angular stream width (as would be observed from the Galactic center) against the Galactocentric polar angle, ψ, and the Galactocentric azimuthal angle, ϕ. This figure shows a large scatter, which is to be expected from a heterogeneous population of progenitors. While it is

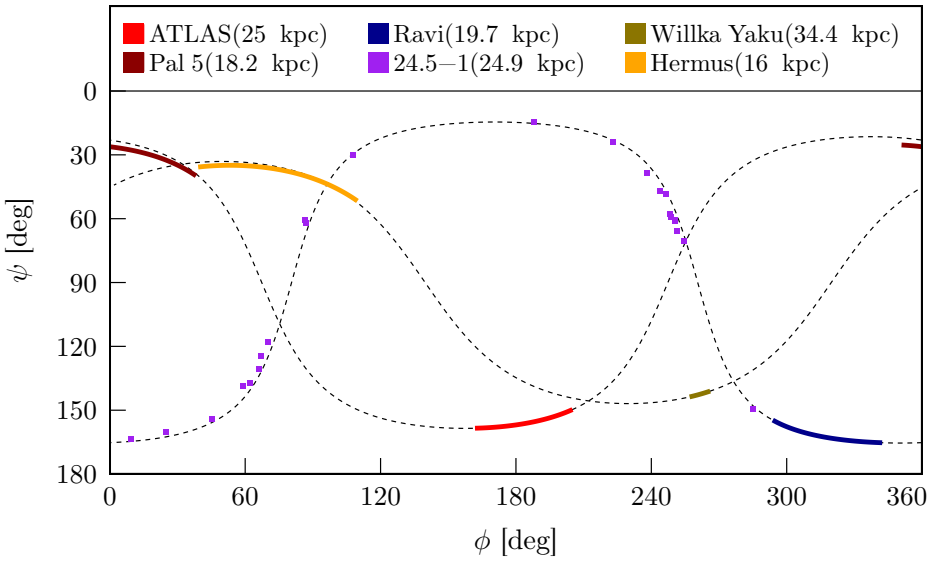

Figure 4.18 Great circle orbital models for 3 of the closest associations between DES and previously-detected streams are plotted in Galactocentric coordinates (ϕ, ψ). The dotted lines are great circle orbits derived from the DES stream endpoints. The solid colored lines show the locations of the streams themselves, the purple squares show the RR Lyrae (Mateu et al., 2018a) that make up the stream 24.5-1.

interesting to note that the streams that appear the widest are also on nearly polar orbits, interpreting any trend in this figure is subject to a number of caveats.

In particular, inferences involving stream widths rely on the assumed mass, structural properties, orbit, and dynamical age of the stream and its progenitor. Geometric effects can cause debris in the stream plane to contribute to the perceived width as calculated by a heliocentric observer. Furthermore, the width can fluctuate along a stream due to the existence of nodes between the progenitor plane and the planes of the stream debris. Nonetheless, it is interesting to note that Figure 4.19 is in general agreement with a model where the Galactic symmetry axis is perpendicular to the plane of the disk.[13]

13. We note that Figure 16 in Erkal et al. (2016b) uses an inconsistent convention for the sign of the azimuthal coordinate ϕ.

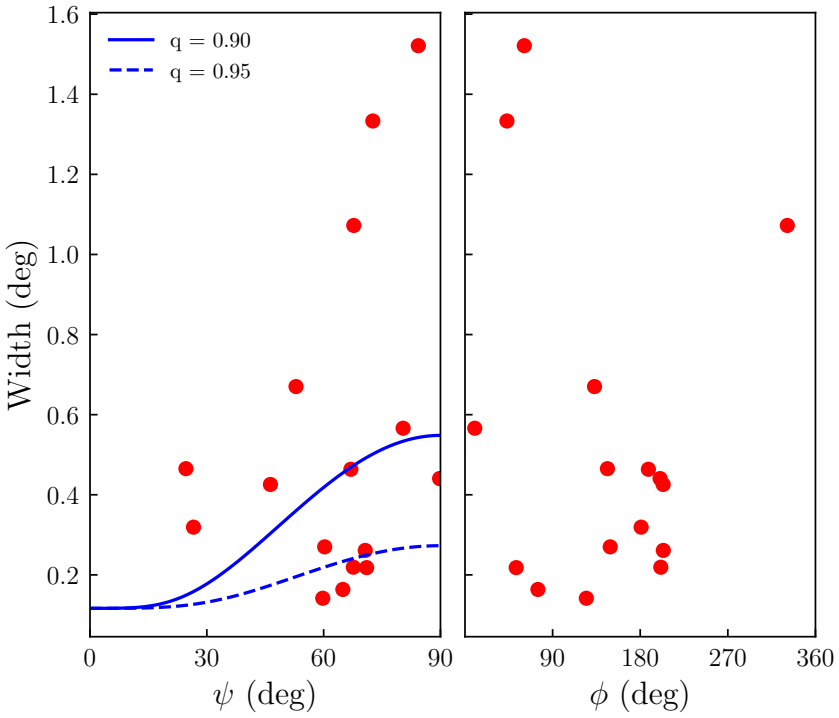

Figure 4.19 Angular widths of stellar streams detected by DES (as perceived by an observer at the Galactic center) as a function of their Galactocentric pole orientation. The left and right panels show the stream width as a function of the Galactocentric polar and azimuthal angle, respectively. The curves show the expected stream width from Erkal et al. (2016b) for streams with age 4 Gyr in a potential with two different flattenings, $q = 0.9$ or $q = 0.95$. These curves are produced assuming a progenitor with a mass of $10^{4.5}\,\mathrm{M}_\odot$ on an orbit with a pericenter of 15 kpc and an apocenter of 30 kpc in a logarithmic potential with a circular velocity of 220 km/s. The bunching of the polar angles of observed streams around low azimuthal angles is caused by the coverage of DES. Interestingly, the widest streams (Jhelum, Indus, Ravi, and Chenab) are close to polar orientations.

4.5.3 Stream progenitors

In Table 4.2 we provided estimates of the stellar mass and progenitor mass (based on the stream width, see Erkal et al., 2016b) of each stream. These can be combined to give a mass-to-light ratio for the progenitor. Doing this, we find that five of the streams (Tucana III, ATLAS, Phoenix, Willka Yaku, and Turbio) have mass-to-light ratios less than ~ 30, while the other eight streams have significantly higher mass-to-light ratios. Given this seeming dichotomy, it is possible that the progenitors with low mass-to-light ratios are globular clusters while those with the higher ratios are dwarf galaxies. However, since the mass-to-light ratios are all higher than expected for a globular cluster (Phoenix stream has the lowest ratio of 10) we cannot make any firm conclusions.

These higher than expected mass-to-light ratios could be due to a variety of reasons. As discussed in 4.3.3, the progenitor mass estimate is only approximate and only works on average for streams on eccentric orbits. Furthermore, if the stream widths have fanned out due to evolving in a non-spherical potential (e.g. Erkal et al., 2016b), the inferred progenitor masses will be overestimated. Finally, the stellar masses will be underestimated for streams that are not fully contained within the DES footprint.

4.6 Conclusions

We searched for Milky Way stellar streams by applying a matched-filter for old, metal-poor stellar populations to three years of data from DES. The unprecedented photometric calibration, depth, and coverage area of the DES data allow us to detect stellar streams out to a distance of $> 50\,\mathrm{kpc}$. Our analysis recovers four narrow stellar streams previously identified within the DES footprint. In addition, we detect eleven new stellar stream candidates. In general, these newly detected streams are wider and lower surface brightness than those detected in previous surveys. We find several tentative associations of these new stream candidates with stellar structures detected in other regions of the sky. In addition, we find

evidence for extra-tidal stellar features around four classical globular clusters. The current analysis makes use of three years of DES data. We expect that additional DES observations, improved data reduction techniques, and improved stream detection algorithms will allow fainter and more distant streams to be detected in the near future. While the DES data currently provide the most sensitive wide-area view of the southern sky, they are merely a precursor for larger sky coverage that can be achieved with DECam and, eventually, the Large Synoptic Survey Telescope (LSST). LSST is expected to find > 100 stellar streams with sensitivity out to the virial radius of the Milky Way (LSST Science Collaboration, 2009). These wide-area photometric surveys will greatly expand our ability to probe the Milky Way stellar halo, providing unprecedented insights into Galactic archaeology and near-field cosmology.

Acknowledgments

We thank the attendees at the "Science at the Calyx" event at the Royal Botanic Garden Sydney, as well as the students of St. John's School in North Ryde, Sydney, for their enthusiastic contributions to the process of naming our proposed stellar streams. We likewise acknowledge Aunty Maureen Sulter of the Gamilaraay nation and Mr. Drew Roberts of the Bundjalung nation for their gracious support of, and feedback on, this naming process.

We warmly thank Colegio Antonio Varas in Vicuña, Chile, for organizing the search for aquatic terms from the native Quechua and Aymara cultures. In particular, we thank high school students Dánae Rojas and Emerson Carvajal, their teacher Yeimy Vargas, and dozens of enthusiastic kindergarteners and first graders who selected the Chilean stream names.

4.A Stream fit configuration

Table 4.A.1 contains the input specifications for the fits to each stream. The procedure for selecting on- and off-stream regions is described in Section 4.3.3. These regions were derived in a variety of ways in order to optimize foreground subtraction and to avoid contamination by other resolved stellar populations, including other streams, globular clusters, and dwarf galaxies. For the ATLAS stream, when calculating N_*, we selected a region along the polynomial fit in Equation (4.6) to account for the curvature of the stream relative to a great circle. Due to the variation in region definitions, we list here the widths and separations of the selected regions for each stream. Additionally, we list the parameters that were fit for each stream. In many cases the data did not allow for a simultaneous fit of all parameters, so a subset of parameters were set to previously determined values or estimated by eye and held fixed.

Table 4.A.1. Input specifications for stream fits

Name	Width (on) (deg)	Width (off) (deg)	Separation (deg)	$m - M$	Age	Z
Tucana III	0.8	0.8	± 0.8	fixed	fixed	fixed
ATLAS	1.2	1.2	± 1.2	free	free	free
Molonglo	1.5	3.0	-2.6	free	fixed	fixed
Phoenix	0.7	0.7	± 0.8	free	fixed	fixed
Indus	3.3	3.3	± 4.1	free	fixed	fixed
Jhelum	2.5	1.2	$+2.0$	free	fixed	fixed
Ravi	2.9	2.9	± 3.6	free	free	free
Chenab	4.0	4.0	± 4.7	free	fixed	fixed
Elqui	2.0	2.0	± 2.2	free	free	free
Aliqa Uma	0.6	1.2	-1.5	fixed	fixed	fixed
Turbio	1.2	2.4	$+2.0$	free	fixed	fixed
Willka Yaku	0.4	0.8	$+0.8$	free	free	free
Turranburra	2.4	2.4	± 3.0	free	free	free
Wambelong	2.0	2.0	± 2.2	free	free	free
Palca	...	...	...	fixed	fixed	fixed

Note. — Input specifications for stellar stream fits. By default, the widths of the on- and off-stream regions are four times the Gaussian stream width. The separation between on and off regions is measured between the stream axis and the center of the off-stream region.

CHAPTER 5

DISCOVERY OF EXTENDED TIDAL TAILS AROUND THE GLOBULAR CLUSTER PALOMAR 13

The text of this chapter was published in Shipp et al. AJ 160, 5 (2020).

5.1 Introduction

Stellar streams—remnants of tidally-disrupted star clusters and satellite galaxies—provide information about the formation history and dark matter distribution of the Milky Way (e.g., Johnston, 1998; Helmi & White, 1999; Bonaca & Hogg, 2018). Dynamically cold streams from disrupting star clusters are also extremely sensitive to gravitational perturbations from massive substructures (e.g., Erkal & Belokurov, 2015b; Bonaca et al., 2019b). The study of stellar streams is thus a promising avenue for studying the distribution of dark matter at sub-galactic scales.

From our perspective in the Galaxy, the discovery and study of stellar streams requires wide-field sky surveys (e.g., Rockosi et al., 2002; Majewski et al., 2003). The population of known streams has increased substantially due to deep, well-calibrated photometric surveys such as the Dark Energy Survey (DES; DES Collaboration 2016; see Shipp et al. 2018), and our ability to characterize stream motions has been recently revolutionized by the *Gaia* mission (Gaia Collaboration et al. 2018; see, e.g., Price-Whelan & Bonaca 2018; Malhan et al. 2018; Shipp et al. 2019) and coordinated spectroscopic follow-up (e.g., the S^5 survey; Li et al., 2019).

The known population of stellar streams now comprises ~ 70 candidates distributed throughout the Milky Way stellar halo.[1] Most stellar streams likely originated from globular clusters, but the vast majority have no known surviving progenitors. In contrast, many

1. `https://github.com/cmateu/galstreams`

clusters have extended extra-tidal features (Belokurov et al., 2006a; Niederste-Ostholt et al., 2010; Sollima et al., 2011; Myeong et al., 2017; Sollima, 2020; Dalessandro et al., 2015; Röser & Schilbach, 2019; Kuzma et al., 2018), but very few appear to host extended thin, dense tidal tails (Rockosi et al., 2002; Grillmair, 2019; Ibata et al., 2019). It is currently unclear how this discrepancy connects to the surface brightness evolution of tidal tails (e.g., Balbinot & Gieles, 2018).

A well-known example of a thin stream is the globular cluster Palomar 5 (Pal 5) and its tidal tails (e.g., Rockosi et al., 2002), which span $\sim 25^\circ$ on the sky (e.g., Bonaca et al., 2020) and contain a total stellar mass comparable to the surviving cluster (e.g., Ibata et al., 2017). The Pal 5 system is an archetype of stellar stream formation and has provided dynamical constraints on the dark matter distribution around the Milky Way (e.g., Küpper et al., 2015a). However, recent studies have found that the Pal 5 orbit and stream may be perturbed by the time-dependent influence of the Galactic bar (Pearson et al., 2017) and/or massive substructures (Erkal et al., 2017). These realizations motivate the study of other globular cluster streams as a way to disentangle the complex dynamical phenomena affecting streams in the inner Galactic halo.

In order to increase the sample of stellar streams with identified progenitors, we have initiated a systematic search for tidal debris structures using photometric data from the DESI Legacy Imaging Surveys (Dey et al., 2019). A first result from this search is the detection of extended tidal structures associated with the globular cluster Palomar 13 (Pal 13). Pal 13 is a low-luminosity globular cluster ($M_V \sim -2.8$; Bradford et al., 2011) at a Galactocentric distance of $\sim 25\,\mathrm{kpc}$ (Côté et al., 2002). Several studies have previously suggested that Pal 13 is undergoing tidal disruption because of the spatial distribution of its blue straggler population (Siegel et al., 2001), its large radial velocity dispersion (Côté et al., 2002), and its extended radial profile ($r_{1/2} = 1.27' \pm 0.16'$; Bradford et al., 2011). More recently, it was shown that Pal 13 member stars display a significant proper motion

scatter (using *Gaia* DR2 astrometry; Yepez et al., 2019), and its stellar population extends to almost twice the estimated Jacobi radius of ∼5—10' (using photometry from the Dark Energy Camera Legacy Survey, DECaLS; Piatti & Fernández-Trincado 2020). Here, we analyze the DECaLS data and present evidence for a linear debris structure aligned with the proper motion and orbit of the Pal 13 cluster, extending $\sim 5^\circ$ in either direction from the cluster center.

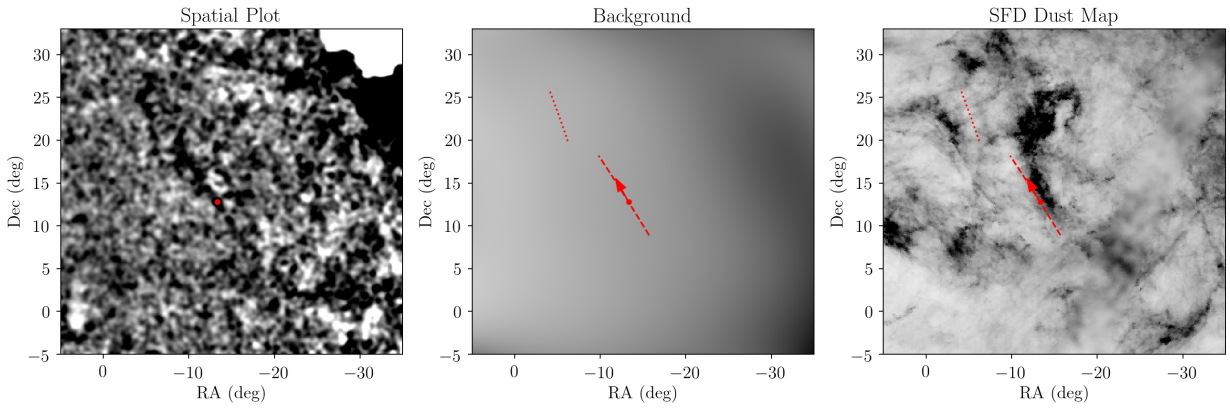

Figure 5.1.1 *Left*: Spatial map of the isochrone-selected residual stellar density at the distance modulus of Pal 13 ($m - M = 16.8$). *Middle*: Smooth polynomial background model in the area around Pal 13. *Right*: The SFD dust map in the area around Pal 13. The red dot represents the location of the Pal 13 cluster, the red dashed line traces the path of the great circle between the endpoints listed in Table 5.3.1, and the red dotted line traces the path of a great circle along the *North-East Arc*. The red arrow indicates the proper motion of Pal 13 from Vasiliev (2019). An animated version of the left-hand panel can be found at this url; a wider-area animation can be found at this url.

5.2 Data & Analysis

We perform our search using DECaLS data distributed in Data Release 8 (DR8) of the DESI Legacy Imaging Surveys (Dey et al., 2019). Source detection is performed with a PSF- and SED-matched-filter detection on the stacked images, with a 6σ detection limit. Morphological fitting and photometry are performed with the `Tractor` code initialized at the positions of detected sources (Lang et al., 2016), and we consider sources with `TYPE =`

'PSF' to be stars. We perform our search on the g, r, z-band data, and we require that sources are detected in all three bands. In addition, we require that sources pass quality cuts: (ANYMASK_G == 0) & (ANYMASK_R == 0) & (ANYMASK_Z == 0) and (FRACFLUX_G < 0.05) & (FRACFLUX_R < 0.05) & (FRACFLUX_Z < 0.05). We correct the measured fluxes for interstellar extinction using the provided extinction values (which make use of Schlafly & Finkbeiner 2011).

We perform an unweighted matched-filter search to this data in color–magnitude (g vs. $g - r$) space (e.g., Rockosi et al., 2002), following the procedure outlined in Section 3.1 of Shipp et al. (2018). We select stars around a synthetic isochrone derived from the stellar evolution models provided by the Dartmouth Stellar Evolution Database (Dotter et al., 2008). These isochrones are accessed programmatically through ugali, a codebase developed for the discovery and analysis of resolved stellar systems in DES (Bechtol et al., 2015; Drlica-Wagner et al., 2015).[2] For the Pal 13 search, we select stars consistent with an isochrone of age 13.5 Gyr and metallicity $Z = 0.0001$ ([Fe/H] $= -2.2$). The selection is defined as in Equation (4) of Shipp et al. (2018), with the selection width parameters determined empirically by comparison to old, metal-poor stellar populations in the data, such as globular clusters and dwarf galaxies (our initial search is not specifically tailored to Pal 13). We limit our isochrone selection to an absolute magnitude of $M_g > 3.5$ to select stars lying along the higher signal-to-noise main sequence. We limit the observed magnitude range of our matched filter to $g < 23$ due to the decreased uniformity of the data at fainter magnitudes.

We scan our isochrone filter in distance modulus from $15 < m - M < 19$ ($10 < D < 63$ kpc) in steps of 0.1 mag. At each distance modulus step, we fit a 5th-order polynomial to the filtered stellar density as a function of α, δ and smooth the data by applying a Gaussian filter with a smoothing kernel of $0.^{\circ}25$. We subtract the background polynomial model

2. https://github.com/DarkEnergySurvey/ugali

from this smoothed data and visually inspect the residual stellar density maps as shown in Figure 5.1.1. We find several known features in the stellar density, including the Triangulum stream (Bonaca et al., 2012) and the Sagittarius stream (Majewski et al., 2003). The most prominent unknown linear feature is coincident with the globular cluster Pal 13, centered at $(\alpha, \delta = 346.^{\circ}7, 12.^{\circ}8)$.

5.3 Extended Tidal Tails Around Pal 13

In order to further examine the linear feature around Pal 13, we first determine optimized isochrone filter parameters (tuned to the stellar population of Pal 13) by-eye via comparison to the Pal 13 color–magnitude diagram in the left-hand panel of Figure 5.2.1. We do not attempt to fit physically significant isochrone parameters to the cluster, and instead empirically determine a filter to most effectively select the Pal 13 signal (outlined in cyan in all panels of Figure 5.2.1). We choose to broaden our filter in the blue direction in order to select stars at the blue edge of the main sequence, which typically provide the highest signal-to-noise in matched-filter searches. We adopt isochrone parameters: $m - M = 16.8$, $\tau = 13.5$ Gyr, and $Z = 0.0001$, where τ refers to the age of the stellar population. These parameters were selected based on the Pal 13 cluster color–magnitude diagram. However, we note that these parameters also appear to maximize the signal-to-noise of the tidal tails. Due to the width of the isochrone filter, the tidal tails are visible at a wide range of isochrone parameters, but we do find that significant adjustments to the age or metallicity noticeably reduces the visibility of the tidal tails in Figure 5.1.1.

The selection region is also defined by a magnitude broadening ($\Delta\mu = 0.5$), an asymmetric color broadening, $C_{1,2} = (-0.02, 1.0)$, and a multiplicative factor on the magnitude uncertainty ($E = 2$), which describes the error-dependent spread in color. All parameters are described in greater detail in Section 3.1 of Shipp et al. (2018).

The linear features detected by our isochrone filter extend $\sim 5^{\circ}$ in each direction from the

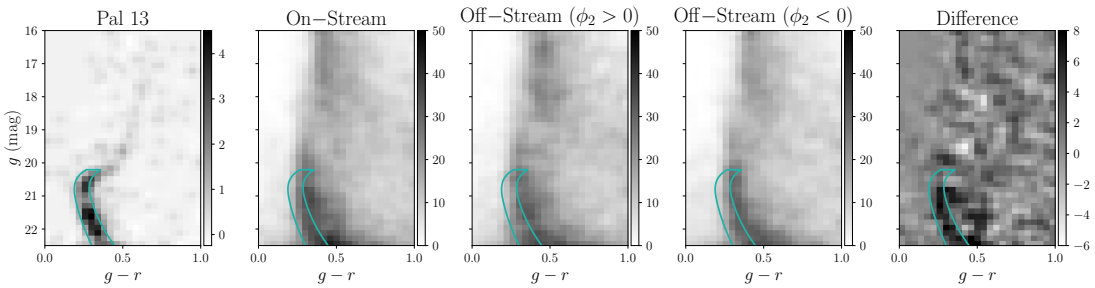

Figure 5.2.1 Color–magnitude diagrams for a region within 0.°4 of the Pal 13 cluster (left), a region within 0.°25 of the track of the Pal 13 tidal features excluding the cluster (left middle), and a background region offset from the Pal 13 track by 2.°0 (right middle). The Hess difference diagram between the on-stream and off-stream regions is shown in the right-most panel. Over-plotted in cyan is the isochrone selection with $m-M = 16.8$, $\tau = 13.5\,\mathrm{Gyr}$, and $Z = 0.0001$.

center of Pal 13. We estimate the endpoints to be $(\alpha, \delta) = (-9.8, 18.2)^\circ$ and $(-15.7, 8.9)^\circ$ and find that the track of the tails is well-matched by the great circle connecting these endpoints. We define a new coordinate system such that the endpoints lie along the x-axis and the cluster is positioned at $(\phi_1, \phi_2) = (0, 0)^\circ$. The coordinate system is defined by the rotation matrix,

$$R = \begin{bmatrix} 0.94906836 & -0.22453560 & 0.22102719 \\ -0.06325861 & 0.55143610 & 0.83181523 \\ -0.30865450 & -0.80343138 & 0.50914675 \end{bmatrix} \quad , \tag{5.1}$$

which transforms from ICRS to stream-aligned coordinates. Throughout the text, we consider the "on-stream" region to be between the endpoints ($-4.°5 < \phi_1 < 6.°4$) and $-0.°25 < \phi_2 < 0.°25$, *excluding* the region within 0.°4 of the globular cluster. We define the radius of the cluster selection to be 0.°4. This area was defined by determining the radius in the direction perpendicular to the tidal tails beyond which there is no visible contribution by the cluster signal in the color–magnitude diagram.

The region around Pal 13 is complicated by a linear feature in the interstellar dust

adjacent to the globular cluster (right panel of Figure 5.1.1). Imperfect reddening corrections can lead to artificial color shifts that could increase or decrease the number of stars passing our isochrone filter. Indeed, we see a deficit of stars to the northwest of Pal 13 coinciding with this dust feature. A more subtle concern is that the underdensity of stars associated with the dust feature could conspire with the rapidly falling foreground stellar density to manifest as an apparent linear overdensity of stars directly adjacent to the dust lane.[3]

To distinguish a spurious density variation from the presence of a distant, metal-poor stellar population associated with Pal 13, we examine the significance of the tidal tails as a function of distance and compare to neighboring, off-stream regions. If the tails are an artifact of the foreground population, they would have the same distance dependence as the neighboring regions, while tidal features associated with Pal 13 would be more prominent at larger distances. In the top two panels of Figure 5.3.1, we show the normalized number of stars along the tidal tails, and in three adjacent equal-area regions above and below the stream. We count the number of stars passing the isochrone selection at a given distance modulus in each of the spatial regions. The counts in the off-stream regions are then normalized to the same maximum value as the on-stream region, in order to highlight the difference in shape between the curves. The number of stars falls off more slowly with distance modulus in the on-stream region than in any of the off-stream regions, including those overlapping with the dust feature visible in Figure 5.1.1. In the lower panel of Figure 5.3.1, we show the ratio of the normalized number of stars in the on-stream region and a region offset by $+2^{\circ}$. We produce 20 realizations of these on-stream and off-stream regions, by selecting regions at the same Galactic latitude, but shifted in Galactic longitude within the DECaLS footprint. We exclude regions that overlap with the Sagittarius stream. In the lower panel of Figure 5.3.1, the solid black line shows the ratio between the on-stream region and the off-stream region at the location of Pal 13. The colored lines represent the ratios of counts

3. This is the 2-dimensional analog of the well-known axiom in particle physics: when analyzing steeply falling spectra, "every dip creates a bump".

in each of the other regions. We consider these ratios to follow a distribution corresponding to the ratio of two Poisson distributions. Given this assumption, the dashed black line represents the mean of the distribution, and the shaded region represents the $\pm 1\sigma$ range. At the distance modulus of Pal 13, the ratio of counts in the Pal 13 on- and off-stream regions is a 4.2σ outlier. We determine that the candidate tidal tails have a different distance dependence than the foreground stars, and that this difference is significantly larger than that of other regions at the same Galactic latitude. We therefore conclude that the tidal tails are more likely associated with the distant stellar population of Pal 13 than with the foreground stellar population.

In addition, we note the presence of a second feature extending from $(\alpha, \delta) = (-6.^\circ 2, 19.^\circ 9)$ to $(-4.^\circ 0, 26.^\circ 0)$, which we refer to as the "*North-East Arc*" (dotted red line in Figure 5.1.1). The feature is disconnected from the observed Pal 13 tidal tails; however, the orientation of the two features bears some resemblance to known "broken" streams, such as the ATLAS and Aliqa Uma stream (Li et al., 2019). Therefore, although we find no concrete evidence of an association between this *North-East Arc* and Pal 13, this feature may be worth investigating further.

5.3.1 Color–Magnitude Diagram

We examine the tidal features in color–magnitude space to characterize the stellar population and compare to the globular cluster itself. Figure 5.2.1 shows binned color–magnitude diagrams in four different regions. The first panel shows stars selected within $0.^\circ 4$ of the Pal 13 globular cluster, the second panel shows stars within the on-stream region (excluding the cluster), and the third and fourth panels shows stars within equal-area off-stream regions, offset from the stream by $\pm 2.^\circ 0$ in ϕ_2. The fifth panel shows the background-subtracted Hess diagram of the on-stream region. The faint overdensity in the fifth panel is plausibly consistent with the globular cluster signal, and suggests that the cluster stellar population

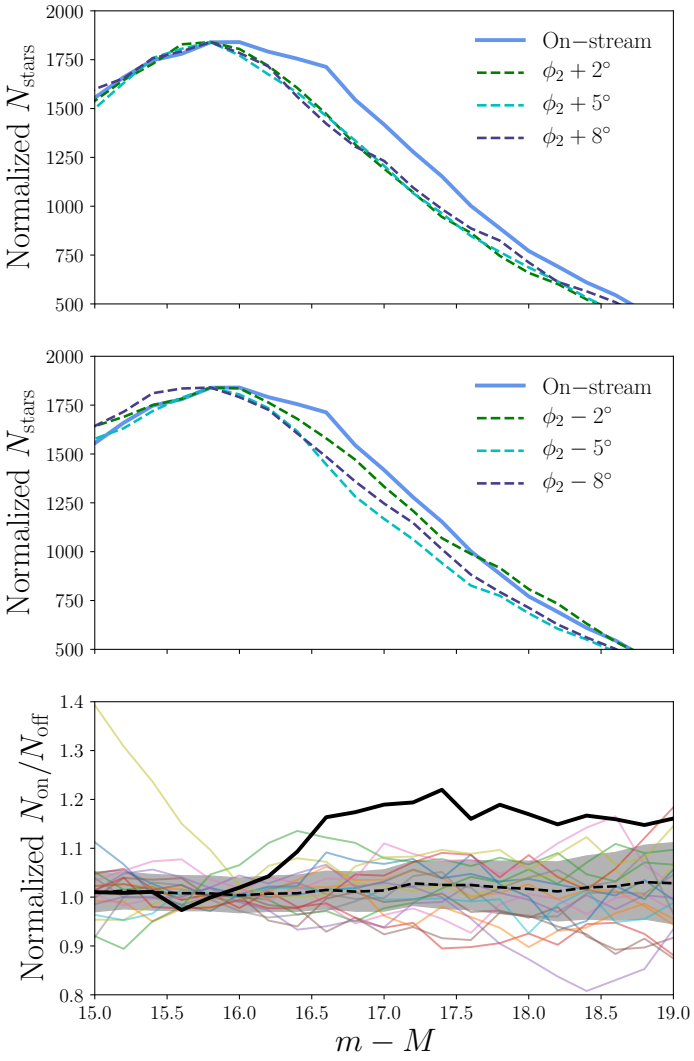

Figure 5.3.1 *Upper and middle:* Relative number of stars as a function of distance modulus in the on-stream region (blue, solid line) and six equal-area regions offset by ± 2°, 5°, and 8° (dashed lines). The number of stars in the off-stream regions are normalized to the maximum value of the on-stream region to emphasize the difference in shape of the curves. The measured stellar density in the on-stream region decreases more slowly with increasing distance than the density in the off-stream regions, suggesting that the observed overdensity is distinct from the foreground population. *Lower*: The ratio of the number of stars in the on-stream region to the number of stars in a region offset by +2°. The black solid line shows the Pal 13 region, and each colored line represents a similar region at equal Galactic latitude. The dashed black line and the shaded region show the mean and $\pm 1\sigma$ range, assuming the distribution follows that of the ratio of two Poisson distributions. At the distance modulus of Pal 13, the ratio of stars in the Pal 13 region is a 4.2σ outlier.

may in fact extend in the direction of the candidate tidal tails, which would support the association between the candidate tails and the Pal 13 globular cluster. We also look for evidence of the *North-East Arc* in color–magnitude space and are unable recover a strong signal, making it difficult to claim association between the *North-East Arc* and Pal 13.

We estimate the significance of the Pal 13 signal based on these selections, as $S \equiv (N_{\rm on} - N_{\rm off})/\sqrt{N_{\rm off}}$. $N_{\rm on}$ represents the number of stars within the on-stream selection and passing the isochrone filter outlined in cyan in Figure 5.2.1. Similarly, $N_{\rm off}$ represents the number of stars passing the isochrone filter and within the area-corrected off-stream region. Following this method, we calculate a significance of the Pal 13 tidal tails of 6.8.

We also find the significance of the stream following the peak detection method of significance calculation in Bernard et al. (2016). We find that when using the best-fit fifth-degree polynomial model background model, the peak of the stellar density profile lies at 4.6σ above the mean of the region within $\pm 3^\circ$ of the tidal tails, excluding the on-stream region. We have verified that the uncertainty on the polynomial model does not greatly impact the tail detection by repeating the process with both a sixth-order and fourth-order polynomial background, and by varying the coefficients of the fifth-order polynomial within their calculated uncertainties. In all cases, the peak detection remains more than 3σ above the mean background level.

[h!]

Table 5.3.1. Measured properties of Pal 13 tidal tails.

Parameter	Value
Endpoint (α, δ)	$(-9.8, 18.2)^\circ$
Endpoint (α, δ)	$(-15.7, 8.9)^\circ$
Length	10.9°
Width	0.25°

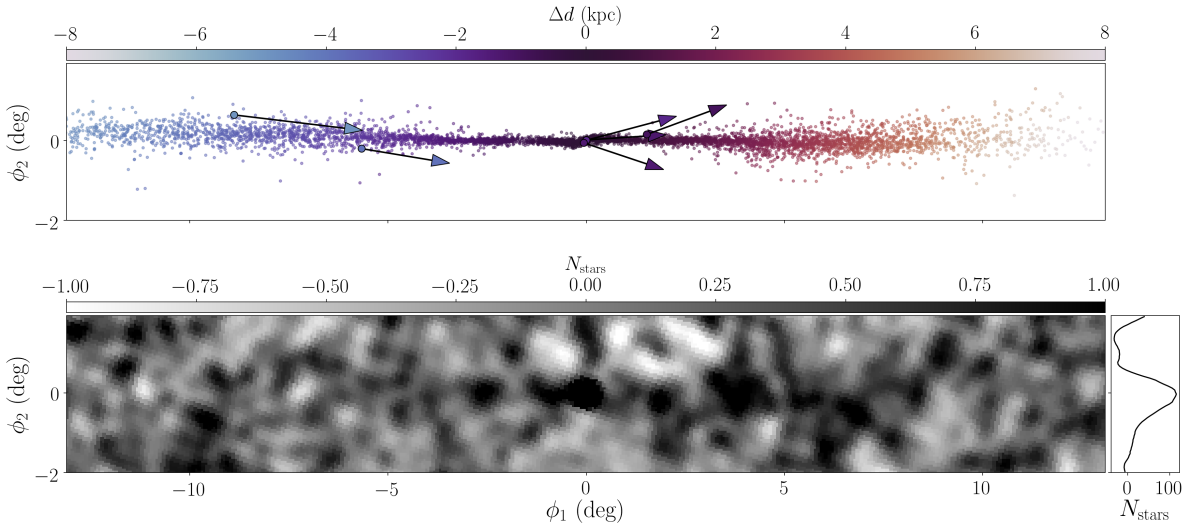

Figure 5.3.2 *Upper:* Star particles in a stream model generated from the best-fit orbit to the measured position and velocity of Pal 13, and the on-sky track of the tidal tails. Likely member RRL stars are overplotted as points with arrows representing their proper motions. The color represents the distance offset from the cluster location at $(\phi_1, \phi_2) = (0, 0)^\circ$. *Lower:* Residual density of stars passing an isochrone selection with $m - M = 16.8$ in the region around Pal 13. The histogram on the right illustrates the area-corrected residual number of stars summed along ϕ_1 within $|\phi_1| < 5^\circ$, excluding the region within 0.4° of the globular cluster.

5.3.2 RR Lyrae Stars

We search for RR Lyrae stars (RRLs) associated with the cluster and tidal tails using the Pan-STARRS1 (PS1) RRL catalog (Sesar et al., 2017). Following the same procedure as in Price-Whelan et al. (2019), we perform the search using the 61,795 RRLs selected by Sesar et al. (2017) as *bona fide* based on their classification scores, plus the 6,459 *non-bona fide* PS1 stars also identified as RRLs in the *Gaia* Specific Objects Study (SOS) catalog. We adopt photometric distances for the RRLs reported by Sesar et al. (2017), which are based on the PS1 (dust-corrected) i-band magnitudes. We also correct for the systematic offset in the distance of RRc stars present in the data published in Sesar et al. (2017) by recomputing their distances using their fundamentalised periods (see Price-Whelan et al., 2019, for full details). The resulting distances have a precision of $\sim 3\%$ (Sesar et al., 2017). We retrieve astrometric information for these RRLs by cross-matching to the *Gaia* DR2 catalog with a

$1''$ tolerance.

Pal 13 is known to have four type *ab* RRLs (V1–V4) (Rosino, 1957), which were recently confirmed as members based on *Gaia* proper motions Yepez et al. (2019) Stars V1, V3, and V4 are present in the PS1 RRL catalog, but V2 is missing from both the PS1 and *Gaia* DR2 RRL catalogs (likely due to crowding, as it is within $3''$of the cluster center). Although this star was not identified as an RRL in *Gaia* DR2, it is present in the main catalog table `gaia_source` where it's proper motion is available, which allowed Yepez et al. (2019) to confirm its membership to the cluster. Since it is missing from the PS1 catalog, we will not include it in our distance analysis to avoid its G or V-band inferred distance introducing potential systematics due to differences in the PLZ calibrations.

We select RRLs with distances (17–35 kpc), positions ($|\phi_2| < 1^\circ$), and a prograde proper motions (corrected for the solar reflex motion) ($\mu_{\phi_1} > 0$) consistent with Pal 13. This selection yields a total of eight type *ab* RRLs: the three stars in the cluster plus another five in the tails. Of these five, two are likely contaminants as they have proper motions ($\mu_{\phi_1}, \mu_{\phi_2}$) close to zero, consistent with the background distribution. The other three RRLs have μ_{ϕ_1} similar to the cluster RRLs. Our search does not reveal any significant overdensity of RRLs near the *North-East Arc*.

The six likely members (three in the cluster, three in the tails) are shown as large markers in the upper panel of Figure 5.3.2. The arrows represent the proper motion of each star, and the color shows the distance offset in kpc from the cluster at $(\phi_1, \phi_2) = (0, 0)^\circ$. The *Gaia* DR2 `source_id`'s for the RRLs are `2814894112367752192`, `2814893910504601600`, `2811888666052959232` (cluster) and `2712246494232725120`, `2815432636842520960`, `2705495870795198464` (tails).

Using the three RRLs in the cluster, we compute a mean distance of 23.6 ± 0.2 kpc. We have not corrected for metallicity since the expected systematic error will be negligible ($< 0.3\%$), as the cluster almost matches the metallicity assumed by Sesar et al. (2017) in

the PLZ relation to compute RR Lyrae distances. Our distance estimate is in excellent agreement with the previous estimate of 23.67 ± 0.57 kpc based on RR Lyrae stars (Yepez et al., 2019) and is slightly shorter than previous isochrone distances $24.3^{+1.2}_{-1.1}$ kpc (Côté et al., 2002). Although well within the random uncertainties, this offset is accounted for by the differences in the assumed metallicity (-0.4 dex lower) and extinction law coefficients (they used the coefficients from Schlegel et al., 1998, available at the time; our distances are based on the new ones from Schlafly & Finkbeiner 2011).

We use the number of RRLs N_{RR} found to provide a rough estimation of the cluster's initial total luminosity, following the procedure described in Mateu et al. (2018b), which uses the $\log N_{RR} - M_V$ relation observed for globular clusters and dwarf galaxies. The observed number of 7(3) type *ab* RRLs in total (tails) yields an estimate $L_V = 5.1^{+9.7}_{-3.4} \times 10^3 L_\odot$ ($1.4^{+2.6}_{-0.9} \times 10^3 L_\odot$), slightly higher than the cluster luminosity estimated by Bradford et al. (2011, $L_V = 1.1^{+0.5}_{-0.3} \times 10^3 L_\odot$), but consistent within the uncertainties. Assuming a stellar mass-to-light ratio $M/L = 2.4$ estimated for the cluster by Bradford et al. (2011), we estimate the stellar mass to be $1.2^{+2.3}_{-0.8} \times 10^4 M_\odot$ in total and $3.3^{+6.3}_{-2.2} \times 10^3 M_\odot$ for the tails. Our findings for the total luminosity and stellar mass therefore supports the claim made by Siegel et al. (2001) and Bradford et al. (2011) that the abnormally large blue straggler population observed in the cluster suggests a higher initial mass and, therefore, luminosity.

5.3.3 Stream Model

The cluster Pal 13 is thought to be on a highly eccentric orbit (e.g., Siegel et al., 2001; Vasiliev, 2019), but satellites that disrupt on very radial orbits are expected to form more diffuse tidal debris structures rather than linear streams (e.g., Helmi & White, 1999). Is it then surprising that the tidal tails of Pal 13 appear stream-like? We use the sky track of the tidal tails determined here and the kinematics of the cluster to fit for the Galactic orbit of the stream, then use the best-fit orbit to generate simulated tidal debris.

We compile measurements of the Pal 13 mean sky position, proper motion, and line-of-sight velocity—$(\alpha, \delta) = (346.^{\circ}685, 12.^{\circ}772)$ (Vasiliev, 2019), $(\mu_{\alpha^*}, \mu_\delta) = (1.615, 0.142)\,\mathrm{mas\ yr}^{-1}$ (Vasiliev, 2019), and $v_{\rm los} = 25.9\,\mathrm{km\,s}^{-1}$ (Baumgardt et al., 2019)—and their associated uncertainties. We adopt a distance to Pal 13 based on the 3 cluster RRLs with PS1 measurements (Section 5.3.2), $d = 23.6 \pm 0.2\,\mathrm{kpc}$. We adopt recently-compiled Galactocentric solar position and velocity measurements (Drimmel & Poggio, 2018) to transform between heliocentric and Galactocentric quantities. We use a standard, three-component mass model (implemented in `gala`; Price-Whelan 2017) to represent the Milky Way, with all disk and bulge parameters fixed to fiducial values (Price-Whelan, 2017; Bovy, 2015), but we fit for the mass and scale radius of the NFW halo component, and treat the cluster distance, proper motion, and radial velocity as free parameters. We include information about the sky track of the stream in our likelihood by adding "control points" spaced by 1° along $\phi_2 = 0$ between $\phi_1 \in [-5, 5]^\circ$; We evaluate the orbit fit at each of these control points, assuming a constant Gaussian width of the stream as given in Table 5.3.1. We note that the spacing of these stream-track control points is arbitrary, but we did not find any major qualitative changes to the orbit fits after varying the number of control points by a factor of two in either direction. We use `BFGS` optimization (Jones et al., 2001–) to maximize the likelihood of the orbit given the data described above.

Our best-fit orbit for Pal 13 has a pericenter of ~ 9 kpc and an apocenter of $\sim 69\,\mathrm{kpc}$ and suggests that the cluster passed through pericenter $\approx 75\,\mathrm{Myr}$ ago. We use this best-fit orbit to run an approximate N-body simulation of the stream formation (we do not resolve the internal dynamics or disruption process, but include a mass model for the progenitor cluster and generate tidally-stripped stars following Fardal et al. 2015). Figure 5.3.2 (top) shows the sky positions (in stream-aligned coordinates) of star particles from this simulation, colored by relative distance to the cluster. The candidate RRL stars associated with the Pal 13 tails—identified from proper motions alone—are generally consistent with the distance trend

and on-sky distribution of star particles in the stream model. At most earlier simulation snapshots (i.e. at different orbital phases), the tidal debris tends to be much more diffuse, so the coherence of the tidal tails may be another indicator that the cluster is near pericenter. This also highlights the importance of present-day orbital phase in determining whether tidal tails are observable.

5.4 Discussion & Conclusions

We have applied an isochrone matched-filter technique to stars in DECaLS to detect evidence for tidal tails coincident with the Pal 13 globular cluster. This observation complements previous studies, which have shown evidence for tidal disruption of Pal 13, including the recent discovery of an extended low-density halo beyond the Jacobi radius (Piatti & Fernández-Trincado, 2020).

The detected tidal tails extend $\sim 5^\circ$ in either direction from the cluster and are well-aligned with the proper motion of Pal 13 (Vasiliev, 2019). We identify a color–magnitude signal in the on-stream region that is consistent with the stellar population of the Pal 13 cluster. In addition, we find three new RRL stars likely associated with the tidal tails, along with four RRLs known to be associated with the cluster. We generate a model of the tails using an orbit fit to the cluster kinematics and find that the model is consistent with the orientation and spatial distribution of the observed tidal tails, and the distance gradient of the RRLs.

The detection of the Pal 13 tidal tails is complicated by nearby structures in the interstellar dust maps, highlighting the importance of deep, precise photometry and the need for additional phase-space information to confirm and model stellar streams. Future observations, such as radial velocity and metallicity measurements by S^5 (Li et al., 2019), and deeper photometric and proper motion measurements by the Rubin Observatory (Ivezić et al., 2019), will allow for higher-precision characterization and modeling of the tidal features of Pal 13.

If confirmed, Pal 13 will be one of only a handful of thin, extended stellar streams that has been confidently associated with a bound progenitor, and, conversely, one of the few globular clusters with detectable long tidal tails. Future observations by *Gaia*, the Rubin Observatory, and WFIRST will allow for the discovery of many more such systems in the coming years. Increasing the population of streams with known progenitors will provide crucial insight into the tidal disruption of globular clusters, the formation of the stellar halo, and the gravitational field of our Galaxy.

CHAPTER 6

PROPER MOTIONS OF STELLAR STREAMS DISCOVERED IN THE DARK ENERGY SURVEY

The text of this chapter was published in Shipp et al. ApJ 885, 3 (2019).

6.1 Introduction

Stellar streams, the tidal remnants of accreted globular clusters and dwarf galaxies, are powerful tools for studying the distribution of matter and the accretion history of our Galaxy (Johnston, 1998; Bullock & Johnston, 2005). Stellar streams arise naturally in hierarchical models of galaxy formation; however, their low surface brightness makes them historically difficult to detect. The advent of large sky surveys has rapidly increased the number of known streams around the Milky Way (e.g., Mateu et al., 2018b, and references therein) and other nearby galaxies (e.g., Zucker et al., 2004; Martínez-Delgado et al., 2010). This explosion in the known population of stellar streams promises to enable detailed statistical modeling of the stream population in the near future (e.g., Bonaca & Hogg, 2018).

Stellar streams are excellent dynamical tools for measuring the properties of the Milky Way, including the total enclosed mass within their orbits (e.g., Gibbons et al., 2014; Bowden et al., 2015; Bovy et al., 2016; Bonaca & Hogg, 2018) and the shape and radial profile of the gravitational field (Law & Majewski, 2010; Erkal et al., 2016b). An individual stream can probe the Milky Way's potential across tens of kiloparsecs (Law & Majewski, 2010; Koposov et al., 2010), while a population of a dozen stellar streams with full kinematic information is expected to constrain the gravitational potential of the Milky Way at sub-percent levels (Bonaca & Hogg, 2018).

Stellar streams are also sensitive tracers of perturbations in the Milky Way's gravitational field. Streams can be used to detect perturbations in the gravitational field of the halo from

known satellites (e.g. Vera-Ciro & Helmi, 2013; Gómez et al., 2015; Erkal et al., 2018, 2019b) and smaller dark matter substructure (e.g. Ibata et al., 2002; Johnston et al., 2002; Yoon et al., 2011b; Carlberg, 2009, 2012; Erkal & Belokurov, 2015a). The Milky Way's largest satellite, the Large Magellanic Cloud (LMC), resides in a dark matter halo that may be 10% as massive as that of the Milky Way (Busha et al., 2011; Boylan-Kolchin et al., 2012). Direct measurements of the LMC mass exist only within $\sim 9\,\mathrm{kpc}$ yielding values of $\sim 2 \times 10^{10}\,\mathrm{M}_{\odot}$ (e.g., Schommer et al., 1992; van der Marel & Kallivayalil, 2014a); however, cosmological arguments predict that the mass of the LMC is nearly an order of magnitude larger (Busha et al., 2011; Boylan-Kolchin et al., 2012). Such a large gravitational perturber located at a distance of only 50 kpc would have an appreciable affect on measurements of the gravitational field in the halo of the Milky Way. Stellar streams, particularly those in spatial proximity to the LMC, offer a sensitive mechanism to independently measure the mass of the LMC at large radii (e.g., Erkal et al., 2018, 2019b).

Large-area, ground-based, digital photometric surveys like the Sloan Digital Sky Survey (SDSS; York et al., 2000), Pan-STARRS (Chambers et al., 2016), VST ATLAS (Shanks et al., 2015), and the Dark Energy Survey (DES; DES Collaboration, 2016) have rapidly increased the number of known stellar streams (e.g., Odenkirchen et al., 2001; Grillmair, 2006; Grillmair & Dionatos, 2006; Belokurov et al., 2006a; Grillmair, 2009; Bonaca et al., 2012; Koposov et al., 2014; Grillmair, 2014; Drlica-Wagner et al., 2015; Balbinot et al., 2016; Bernard et al., 2016; Grillmair, 2017a,b; Myeong et al., 2017; Shipp et al., 2018; Jethwa et al., 2018). The population of stellar streams discovered in DES is of particular interest for constraining the gravitational field in the Milky Way's outer halo (Shipp et al., 2018). The DES streams constitute some of the faintest and most distant streams discovered around the Milky Way and, due to the excellent photometry provided by DES, they can be distinguished from foreground stellar populations with unprecedented accuracy. Furthermore, the location of these streams in the Southern Hemisphere makes them sensitive probes of the joint potential

of the Milky Way and LMC.

While deep photometric surveys are excellent for detecting faint stellar structures at large distances, additional phase space information is necessary for comprehensive dynamical modeling (e.g. Eyre & Binney, 2009; Bowden et al., 2015; Law & Majewski, 2010; Bovy, 2014; Bovy et al., 2016; Erkal et al., 2019b). The 3D kinematics of faint stream stars can be obtained via a combination of proper motion measurements from high-precision astrometric surveys and radial velocity measurements from deep spectroscopic observations. The second data release from the *Gaia* satellite (*Gaia* DR2; Gaia Collaboration et al., 2018) provides unprecedented proper motion measurements for more that 1 billion stars. *Gaia* DR2 has enabled proper motion measurements for stellar streams at distances of tens of kiloparsecs (e.g., Price-Whelan & Bonaca, 2018; Koposov et al., 2019; Fardal et al., 2019), as well as joint photometric and astrometric discovery of previously unknown streams (Malhan & Ibata, 2018; Malhan et al., 2018).

In addition to providing kinematic information, the systemic proper motions of stellar streams can also greatly improve the efficiency of target selection for spectroscopic follow-up surveys. Proper motions can be used to discriminate likely stream members from foreground Milky Way stars and other halo stars. For example, the Southern Stellar Stream Spectroscopic Survey (S^5; Li et al., submitted), an on-going program to map the line-of-sight velocities and metallicities of the DES streams using the 3.9-m Anglo-Australian Telescope's 2-degree-Field (2dF) fibre position and AAOmega spectrograph, efficiently selects targets following the techniques described here.

In this paper, we cross-matched data from DES DR1 and *Gaia* DR2 to measure proper motions for stellar streams in the DES footprint.[1] We performed two distinct analyses that each combined precise photometry from DES DR1 with precise astrometry from *Gaia* DR2. First, we performed a simple "by-eye" analysis to visibly highlight the proper motion signal

1. We excluded the Palca stream from this analysis due to its large width and extent on the sky, which make it difficult to characterize.

of stellar streams by removing the majority of the Milky Way foreground contamination with physically motivated cuts. Next, we performed a more statistically rigorous Gaussian mixture model (GMM) fit, in which we applied a less-strict data selection, and then fit a two-component Gaussian model in proper motion space to account for both the Milky Way foreground and the stream signal.

We detected and confirmed proper motion signatures for nine of the 14 streams (Aliqa Uma, ATLAS, Chenab, Elqui, Indus, Jhelum, Phoenix, Tucana III, Turranburra), including the most distant DES stream, Elqui, at $\sim 50\,\mathrm{kpc}$. The proper motions of eight of these streams were confirmed in preliminary data from S^5 (Li et al., submitted), while one of these streams (Turranburra) has a corresponding signal in the proper motion of coincident RR Lyrae stars. We report low-confidence proper motion signatures of four additional streams (Ravi, Wambelong, Willka Yaku, and Turbio), and no significant proper motion signature for the Molonglo stream (Grillmair, 2017a). Interestingly, we found that several of the DES streams have systemic proper motions that are misaligned with their tracks on the sky. Such an offset is expected due perturbative gravitational influence of the LMC (Erkal et al., 2019b; Koposov et al., 2019).

This paper is organized as follows. In Section 6.2, we describe our cross-matched sample of data from DES DR1 and *Gaia* DR2. In Section 6.3, we discuss the two methods used to obtain proper motion measurements. In Section 6.4, we present our results, and in Section 6.5, we discuss some of the implications of our measurements. We conclude in Section 6.6.

6.2 Data Preparation

Our data set consists of wide-area ground-based photometry from DES DR1 (DES Collaboration et al., 2018) and precision space-based astrometric measurements from *Gaia* DR2 (Gaia Collaboration et al., 2018). We performed an angular cross-match between these cata-

logs based on a matching radius of $0\farcs5$. There is a systematic astrometric offset of ~ 150 mas between DES DR1 and *Gaia* DR2.[2] Before performing the cross-match, we corrected the DES astrometry by fitting two 2D polynomials to the offsets in right ascension and declination between DES and *Gaia* as a function of location in the DES footprint. After applying this correction we find the median offset between DES and *Gaia* to be ~ 55 mas. The *Gaia* DR2 source catalog consists predominantly of stellar objects. To further ensure our population is not contaminated by galaxies, we cut on the DES quantity, `EXTENDED_COADD` $= 0$, which selects high-confidence stars by comparing to the DES point spread function (PSF; Section 4.5 of DES Collaboration et al., 2018). We found that this cut removes very few objects from our final catalog, and a looser selection on the DES star/galaxy separation (i.e., `EXTENDED_COADD` ≤ 1) had no effect on the results of this analysis.

We also removed objects with bad astrometric fits in *Gaia* DR2. As described in Lindegren et al. (2018), we define $u \equiv (\texttt{astrom\_chi2\_al}/(\texttt{astrom\_n\_good\_obs\_al} - 5))^{1/2}$, and we remove stars with $u > 1.2 \times \max(1, \exp(-0.2(G - 19.5)))$. Here `astrom_chi2_al` and `astrom_n_good_obs_al` are the astrometric quantities available in the *Gaia* DR2 catalog.

In addition, we removed nearby stars by making a parallax cut of $\varpi < 0.5$ mas. We explored a more inclusive parallax cut that incorporated the uncertainty on the parallax measurement (similar to Pace & Li 2019), but we found that such a cut increased contamination from faint foreground stars with large parallax uncertainties. We thus chose to retain our strict cut on parallax alone, though we recognize that such a cut will exclude some fainter members with larger parallax uncertainties. This cut was applied for both analyses.

For flux measurements, we used the `SExtractor` PSF magnitudes derived from the DES DR1 data. These magnitudes were corrected for interstellar reddening according to the procedure described in Section 4.2 of DES Collaboration et al. (2018). We calculated a correction to the DES DR1 calibrated magnitudes in each band, b, according to $A_b =$

2. The offset between DES DR1 and *Gaia* DR2 is due to the fact that the DES DR1 absolute astrometry was tied to 2MASS (DES Collaboration et al., 2018).

$E(B-V) \times R_b$, where the fiducial coefficients were derived using the Fitzpatrick (1999) reddening law with $R_V = 3.1$ and the $E(B-V)$ values come from Schlegel et al. (1998). The coefficients R_b were taken from DES Collaboration et al. (2018): $R_g = 3.186$ and $R_r = 2.140$. Throughout this paper, we use g and r to refer to the dereddened PSF magnitudes derived from DES DR1. Our cross-matched sample ranges in magnitude from $16 \lesssim g \lesssim 21$, where the bright threshold is set by the saturation limit of DES and the faint threshold is set by the sensitivity of *Gaia*.

For each stream, we transformed the data into a coordinate system aligned with the track of the stream, such that ϕ_1 and ϕ_2 are the coordinates along and across the track of the stream, respectively (e.g., Koposov et al., 2010). This transformation is performed by rotating the celestial equator to the great circle defined by the poles listed in Table 3 of Shipp et al. (2018), so that $(\phi_1, \phi_2) = (0^\circ, 0^\circ)$ lies at the center of the observed portion of the stream. The rotation matrix for each stream is included in Appendix 6.C.

When analyzing each stream, we used proper motions converted into the rotated coordinate system and corrected for the solar reflex motion. We refer to these proper motions as $\mu_{\phi_1}, \mu_{\phi_2}$, where μ_{ϕ_1} includes the $\cos\phi_2$ correction. The velocity of the Sun relative to the Galactic standard of rest is taken to be $(U_\odot, V_\odot, W_\odot) = (11.1, 240.0, 7.3)\,\mathrm{km\,s^{-1}}$ (Schönrich et al., 2010b; Bovy et al., 2012) and we used the stream distances reported in Shipp et al. (2018).

We then performed several data selections, some of which were applied generically to the data set, and some of which were applied selectively, depending on the stream and the analysis method. We enumerate these selection criteria below.

(i) **Color-magnitude:** We selected stars in $g-r$ vs. g color-magnitude space following a method similar to that described in Pace & Li (2019). Red-giant branch (RGB) and main-sequence (MS) stars were selected based on the best-fit Dotter isochrones (Dotter et al., 2008) to the DES data. We began with the isochrone parameters listed

in Shipp et al. (2018), then updated the age and metallicity of the isochrones based on the likely members after an iteration of the proper motion fit. The final isochrone values are listed in Table 6.B.1. For a given isochrone, we selected stars within either $\Delta(g-r) \pm 0.05$ mag or $\Delta g \pm 0.4$ mag of the Dotter isochrone. In addition, we selected blue horizontal branch (BHB) stars using an empirical isochrone of M92 from Clem (2005) transformed to the DES photometric system. For the BHB selection, we used a wider color window, $\Delta(g-r) \pm 0.10$, due to the reduced foreground contamination at bluer colors. We did not select any red horizontal branch stars.

(ii) **Magnitude:** In some cases, we made an additional magnitude cut that selected reasonably bright stars with smaller proper motion uncertainties. For the by-eye analysis of the brightest streams (i.e. ATLAS, Chenab, Jhelum, Phoenix, Ravi, Tucana III, Turranburra, and Wambelong), we selected stars with $g < 19$. In the Gaussian mixture model analysis, all streams had a cutoff at an absolute magnitude in the g-band of $M_g = 2$.

(iii) **Metal-poor:** We performed a cut in $(g-r)$ vs. $(r-i)$ color-color space to select for metal-poor stars. Stars that lie along more metal-poor isochrones tend to have redder $r-i$ colors at a given $g-r$ color, as shown in Li et al. (2018) and Pace & Li (2019). We selected stars that lie between 0.02 and 0.06 mag in $r-i$ above the empirical ridgeline of the stellar locus in DES. This selection was made only when necessary to further eliminate foreground contamination (i.e., Indus, Jhelum, Ravi, Turbio, Turranburra, and Wambelong).

(iv) **Spatial:** We selected a spatial region along each stream. For most streams, this is a region along the great circle connecting the stream's endpoints, as specified in Shipp et al. (2018). However, for ATLAS, which shows significant deviation from a great circle, the on-stream region was selected along the track defined by Equation 6 in Shipp et al. (2018). The widths of the on-stream selection varied between the two

analysis methods. For the by-eye fit, we used the regions described in Table A.1 of Shipp et al. (2018). In contrast, for the Gaussian mixture model analysis, we define the on-stream region to be $3w$, where w represents the width of the stream, as reported in Table 1 of Shipp et al. (2018).

(v) **Escape velocity:** When performing the GMM analysis (Section 6.3.2), we removed stars with tangential velocities greater than the Milky Way escape velocity at the distance of each stream. We calculated the escape velocity, $v_{\rm esc}$, using the `MWPotential2014` from `galpy` (Bovy, 2015), with a Milky Way halo mass of $M_{\rm vir} = 1.6 \times 10^{12}\,{\rm M}_{\odot}$, as in Pace & Li (2019). We calculated the tangential velocity, $v_{\rm tan}$, from the proper motion of each star, assuming the distance of the target stream, and removed all stars with $v_{\rm tan} > v_{\rm esc}$, in order to filter out nearby and possible hypervelocity stars. We verified that the analysis was changes to this cut, e.g. by removing stars with $v_{\rm tan} - 3\sigma_{v_{\rm tan}} > v_{\rm esc}$.

6.3 Methods

We obtained measurements of the proper motion of each stream with two complementary methods. First, we applied a set of physically-motivated cuts to increase the prominence of the stellar stream signal, which was estimated by eye based on the clustering of stars in proper-motion space. Second, we fit a GMM to the data to obtain a statistically robust measurement of the proper motion, proper motion gradient, and corresponding uncertainties for each stream. The by-eye fit yields a quick and intuitive measurement of the proper motion, while the GMM provides a more rigorous measurement including statistical uncertainties.

6.3.1 By-Eye Fit

We applied a set of physically-motivated selection criteria to the data coincident with each stream to decrease foreground contamination and enhance the proper motion signature of

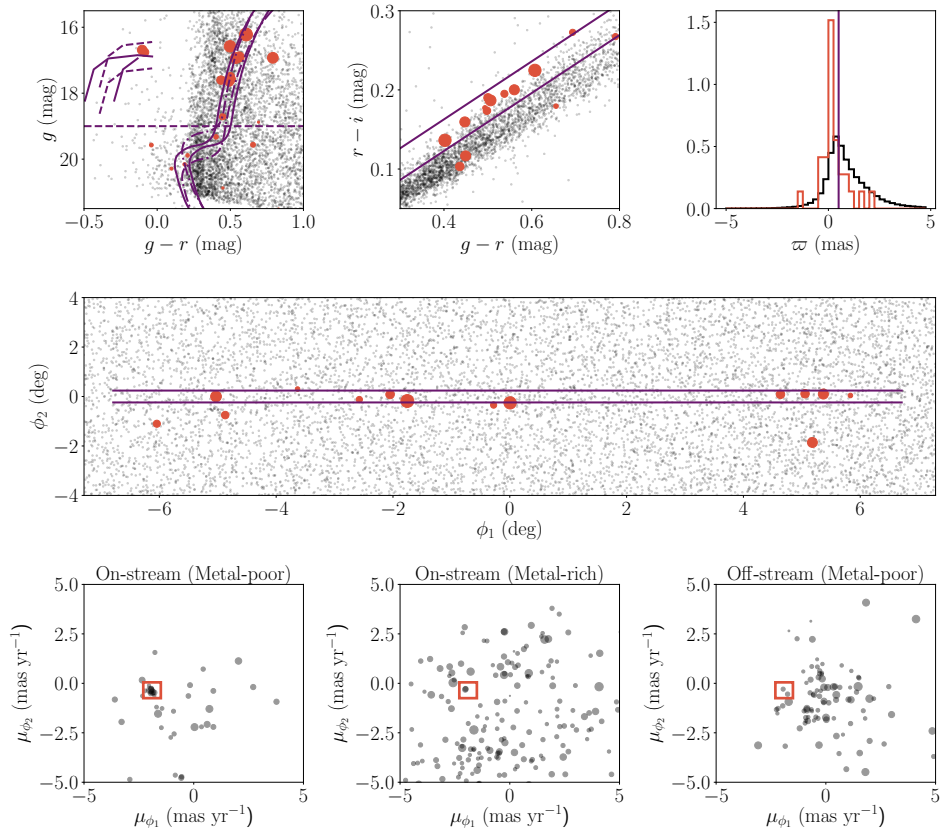

Figure 6.3.1 Example of the by-eye analysis for the Phoenix stream. The gray points illustrate the stars included in the cross-matched catalog surrounding the Phoenix stream. The purple lines indicate the selections made on color-magnitude (top left), color-color (top middle), parallax (top right), and spatial parameters (center). The lower three panels illustrate the proper motions of stars passing all selections (left), failing the metal poor cut (via color-color selection) but passing other selections (middle), and failing the on-stream cut but passing other selections (right). A clear overdensity corresponding to the proper motion of the Phoenix stream (orange box) can be seen in the lower-left panel when all selections are applied. Orange points in the color-magnitude and color-color panels reside within the orange box in proper motion and pass the parallax and spatial selections. The orange histogram in the parallax panel contains stars that reside within the orange box and pass the color-magnitude, color-color, and spatial sections. Orange points in the center panel reside within the orange box and pass the color-magnitude, color-color, and parallax selections. The size of the orange points in the upper panels and the black points in the lower panels is inversely proportional to the uncertainty in the measured proper motion.

stellar streams (enumerated in Section 6.2). We selected on-stream and off-stream regions for comparison with the local Milky Way foreground (iv). In addition, for a subset of bright streams (ATLAS, Chenab, Jhelum, Phoenix, Ravi, Tucana III, Turranburra, and Wambelong), to remove stars with larger proper motion uncertainties (ii). We visually inspected the cleaned data to identify clusters of stars in proper motion space that could correspond to the signatures of the stellar streams. We identified possible proper motion signatures of thirteen streams (Table 6.A.1); nine of these are similarly identified by the GMM procedure described in Section 6.3.2. Since the GMM procedure is more objective and statistically rigorous, we choose to report those values as our results; however, the by-eye fit proved to be a valuable diagnostic for validating the GMM fit.

Figure 6.3.1 shows a graphical representation of these cuts applied to the Phoenix data. In the lower panels of Figure 6.3.1, the proper motions of stars passing three different selections are shown. The lower-left panel shows stars passing all selections, and the proper motion signal of the Phoenix stream is highlighted by the orange box. The lower-middle panel contains metal-rich stars that lie along the stream, and the lower-right panel shows metal-poor stars in the off-stream region. As expected, the proper motion signal is only visible in metal-poor stars that lie along the track of the Phoenix stream. Stars with a proper motion consistent with our measurement of the Phoenix stream (within the orange box) are plotted in the other panels of Figure 6.3.1 and are found to be consistent with the Phoenix stream in color, magnitude, and location on the sky.

6.3.2 Gaussian Mixture Model Fit

After obtaining measurements by eye, we fit a Gaussian mixture model to the data. We performed the fit on all 14 streams, and obtained results consistent with the by-eye method for the nine streams. The fitting procedure follows that of Pace & Li (2019) and is described briefly below.

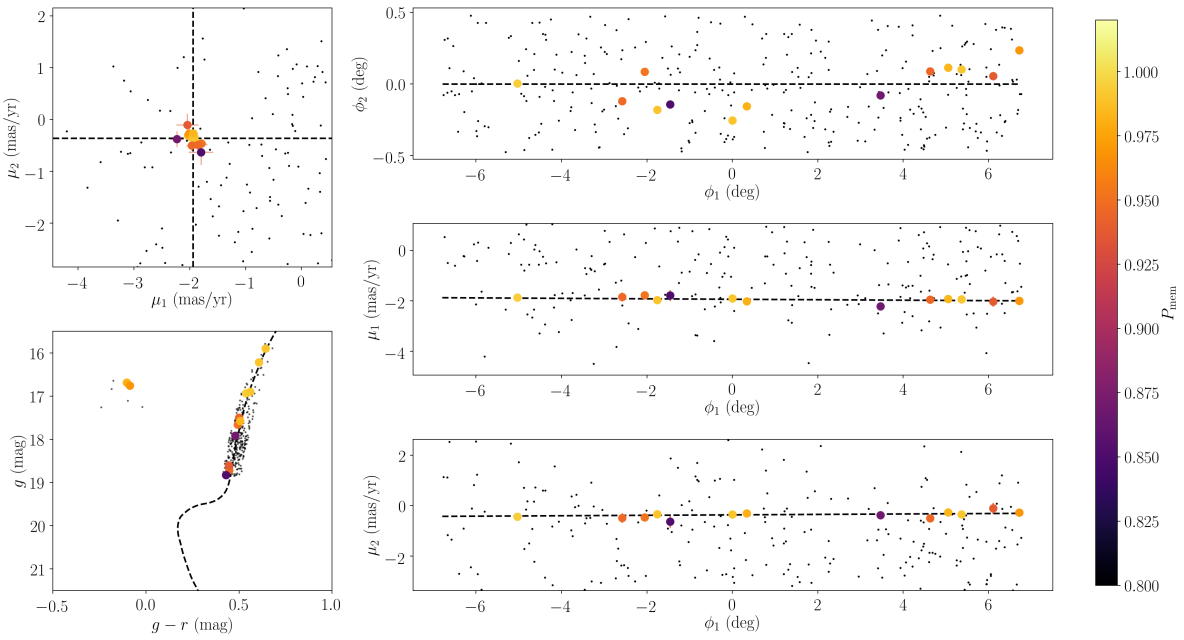

Figure 6.3.2 Results of the Gaussian mixture model fit to the Phoenix stream. The black points illustrate the data that was included in the fit; stars with membership probabilities $P_{\rm mem} > 0.8$ are color-coded by their membership probabilities.

The mixture model includes two multivariate Gaussian components in proper motion space. The first describes the stream, and has a dispersion fixed to zero. The second component accounts for the Milky Way foreground and any other contaminating stellar populations. For each stream, we also tried introducing a third component to test whether the background would be better described by two Gaussians and in no case were the resulting stream parameters affected by the additional component. We therefore model the background by a single Gaussian component in the results presented here.

The likelihood is calculated as a product of two parts, the proper motion distribution and the spatial distribution. The proper motion term is modeled as,

$$\ln \mathcal{L}_{\rm PM} = -\frac{1}{2}(\chi - \overline{\chi})^\top C^{-1} (\chi - \overline{\chi}) - \frac{1}{2} \ln \Big(4\pi^2 \det C \Big), \tag{6.1}$$

where $\chi = (\mu_{\phi_1}, \mu_{\phi_2})$ is the data vector and $\overline{\chi} = (\overline{\mu_{\phi_1}}(\phi_1), \overline{\mu_{\phi_2}}(\phi_1))$ is the vector containing

the systemic proper motion of the stream as a function of ϕ_1. Allowing the systemic proper motion to vary with ϕ_1 gives us a measurement of the proper motion gradient along the length of the stream. The covariance matrix, C, includes the correlation between the proper motion errors and a term for the intrinsic proper motion dispersion . The covariance matrix is:

$$C = \begin{bmatrix} \epsilon^2_{\mu_{\phi_1}} + \sigma^2_{\mu_{\phi_1}} & \epsilon^2_{[\mu_{\phi_1} \times \mu_{\phi_2}]} \\ \epsilon^2_{[\mu_{\phi_1} \times \mu_{\phi_2}]} & \epsilon^2_{\mu_{\phi_2}} + \sigma^2_{\mu_{\phi_2}} \end{bmatrix} \tag{6.2}$$

The second part of the mixture model is a spatial prior based on the distance between stars and the stream axis in ϕ_2. We included the spatial stream prior probability as a truncated normal distribution, with a standard deviation equal to the stream width listed in Table 1 of Shipp et al. (2018). For the Milky Way, the spatial prior probability was approximated as a uniform distribution across the narrow region included in the fit. The complete set of free parameters and their priors are listed in Table 6.3.1.

Before performing the mixture model fit, we first made several data selections as described in Section 6.2.

Following Pace & Li (2019), we use the `MultiNest` algorithm (Feroz & Hobson, 2008; Feroz et al., 2009) to determine the posterior distribution. We compute a Bayes factor to assess the significance of each stream signal, comparing models with only the Milky Way component, and with both the Milky Way and stream components.

As an example, we show the results of the Gaussian mixture model fit to Phoenix in Figure 6.3.2. All stars included in the fit are plotted, with stars with $P_{\rm mem} > 0.8$ colored by their membership probability.

Table 6.3.1. Priors on Gaussian Mixture Model.

Parameter	Prior	Range	Units
$\mu_{\phi_{1,2}}$	Uniform	(-10, 10)	mas/yr
$d\mu_{\phi_{1,2}}/d\phi_1$	Uniform	(-3, 3)	mas/yr/deg
$\mu_{\phi_{1,2},\mathrm{MW}}$	Uniform	(-10, 10)	mas/yr
		(-1, 3)	mas/yr
f_{MW}	Uniform	(0, 1)	

Note. — Priors on the nine free parameters in the Gaussian mixture model fits. $\mu_{\phi_{1,2}}$ are the mean stream proper motions at $\phi_1 = 0$. $d\mu_{\phi_{1,2}}/d\phi_1$ are the gradients of the stream proper motions with respect to ϕ_1. $\mu_{\phi_{1,2},\mathrm{MW}}$ are the mean proper motions of the Milky Way foreground component. $\sigma_{\mu_{\phi_{1,2}},\mathrm{MW}}$ are the dispersions of the Milky Way proper motions. f_{MW} is the fraction of stars belonging to the Milky Way component.

Table 6.3.2. Derived proper motion of DES streams.

	$\mu_\alpha cos\delta$ (mas/yr)	μ_δ (mas/yr)	μ_{ϕ_1} (mas/yr)	μ_{ϕ_2} (mas/yr)	$d\mu_{\phi_1}/d\phi_1$ (mas/yr/deg)	$d\mu_{\phi_2}/d\phi_1$ (mas/yr/deg)	$v_{\rm tan}$ (km/s)	Bayes Factor
Aliqa Uma	0.25 ± 0.03	-0.71 ± 0.05	0.98 ± 0.04	-0.34 ± 0.03	-0.02 ± 0.03	-0.04 ± 0.02	141	-2.3
ATLAS	0.09 ± 0.03	-0.88 ± 0.03	1.66 ± 0.04	-0.15 ± 0.05	0.02 ± 0.005	-0.02 ± 0.005	181	18.0
Chenab	0.32 ± 0.03	-2.47 ± 0.04	1.03 ± 0.05	-0.60 ± 0.03	0.04 ± 0.01	-0.02 ± 0.01	225	15.2
Elqui	0.13 ± 0.04	-0.33 ± 0.09	0.56 ± 0.06	-0.03 ± 0.05	-0.03 ± 0.02	-0.04 ± 0.01	133	13.2
Indus	–	–	-3.09 ± 0.03	0.21 ± 0.03	0.05 ± 0.004	0.04 ± 0.004	245	15.5
Jhelum	–	–	-6.00 ± 0.03	-0.83 ± 0.05	–	–	378	9.4
Jhelum-a	–	–	-6.01 ± 0.02	-0.84 ± 0.04	–	–	379	22.9
Jhelum-b	–	–	-4.97 ± 0.03	0.11 ± 0.06	–	–	310	
Phoenix	2.76 ± 0.02	-0.05 ± 0.02	-1.94 ± 0.02	-0.36 ± 0.02	-0.01 ± 0.01	0.01 ± 0.01	179	7.8
Tucana III	-0.10 ± 0.04	-1.64 ± 0.04	1.08 ± 0.03	-0.03 ± 0.03	0.12 ± 0.03	-0.06 ± 0.03	129	28.2
Turranburra	0.43 ± 0.04	-0.89 ± 0.04	0.69 ± 0.04	-0.22 ± 0.04	0.00 ± 0.02	-0.03 ± 0.01	95	2.7

Note. — The first two columns are proper motion measurements in the observed equatorial coordinate system. Fits to Indus and Jhelum did not converge without first correcting for the solar reflex motion. All uncertainties reported here are statistical uncertainties from the mixture model fitting. Additional uncertainties, including the uncertainty propagated from the distance measurement through the correction for the solar reflex motion, are not included. We find that Jhelum is best fit by a two-stream-component model. The first row lists the result of fitting a single stream component to Jhelum, and Jhelum-a and Jhelum-b are the results of each component from the two-component fit. The tangential velocity is calculated by $v_{\rm tan} = 4.74 d\mu$ km/s, where d is the distance measured in kpc, and μ is the proper motion measured in mas yr^{-1}.

6.4 Results

The by-eye and GMM analyses yield proper motion measurements for nine streams: Aliqa Uma, ATLAS, Chenab, Elqui, Indus, Phoenix, Jhelum, Tucana III, and Turranburra, as illustrated in Figure 6.4.1. In the Figure, the points indicate stars included in the by-eye analysis. The solid crosshairs indicate the by-eye measurement, and the dashed crosshairs mark the result of the GMM fit. The by-eye and GMM measurements agree quite well for the majority of the streams, with the exception of the long, thick Indus and Jhelum streams. The Indus stream has an offset in μ_{ϕ_1} derived from the by-eye and the GMM measurements, which can be attributed to the significant proper motion gradient fit by the GMM analysis. In contrast, the discrepancy in the Jhelum stream can be attributed to the existence of two distinct components of the stream (Bonaca et al., 2019a). Individual streams are discussed in more detail in Section 6.5.1.

Initial proper motion measurements from the by-eye analysis were used to target S^5 (Li et al., submitted). Seven of the nine streams measured here (Aliqa Uma, ATLAS, Chenab, Elqui, Indus, Phoenix, and Jhelum) have been observed by S^5, and a preliminary analysis of the S^5 data shows that the stars used to derive our proper motion measurements have relatively small dispersions in radial velocity space (Li et al. submitted). We take this as a spectroscopic confirmation of the proper motion measurements quoted here. An eighth stream, Tucana III, has been previously observed spectroscopically by Li et al. (2018), and we again find that the proper-motion members are tightly grouped in radial velocity space. The ninth stream, Turranburra, has not been fully observed by S^5; however, we find that the proper motion measured here is consistent with the proper motion of RR Lyrae stars observed by *Gaia* that are spatially consistent with the stream. We describe the analysis of these RR Lyrae in more detail in Section 6.5.1 and take this to be a secondary confirmation of the proper motion of this stream.

We also report lower-confidence proper motion by-eye measurements for four streams,

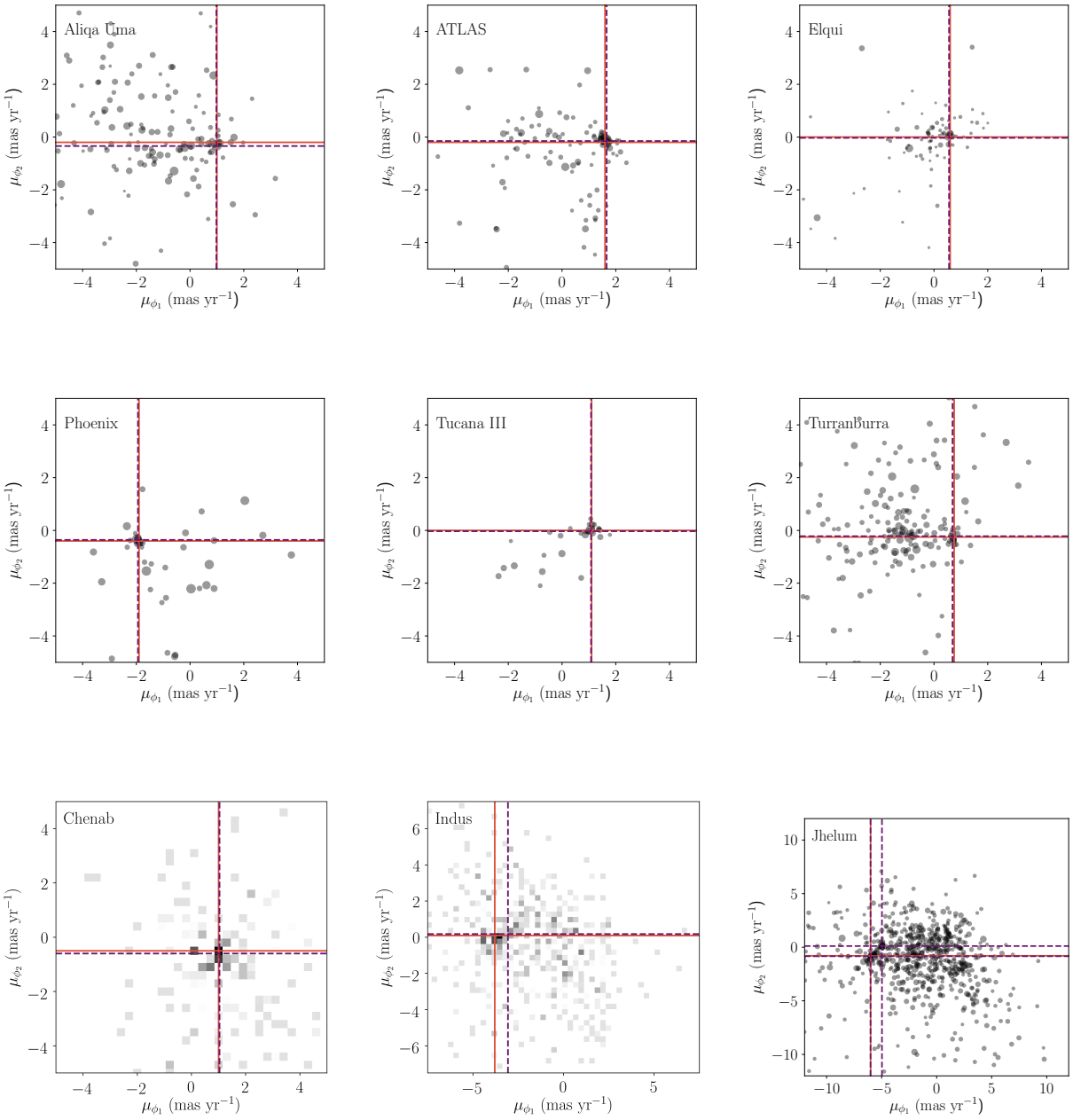

Figure 6.4.1 Proper motions are transformed to stream coordinates, $\mu_{\phi_1}, \mu_{\phi_2}$. Best-fit proper motion estimates fit by eye are shown by the solid orange crosshairs, while the best-fit results from the GMM are shown in purple. In the scatter plots, the size of the points is inversely proportional to the 1σ uncertainty on the proper motion of each star. Chenab and Indus, two of the thicker streams, are better shown by

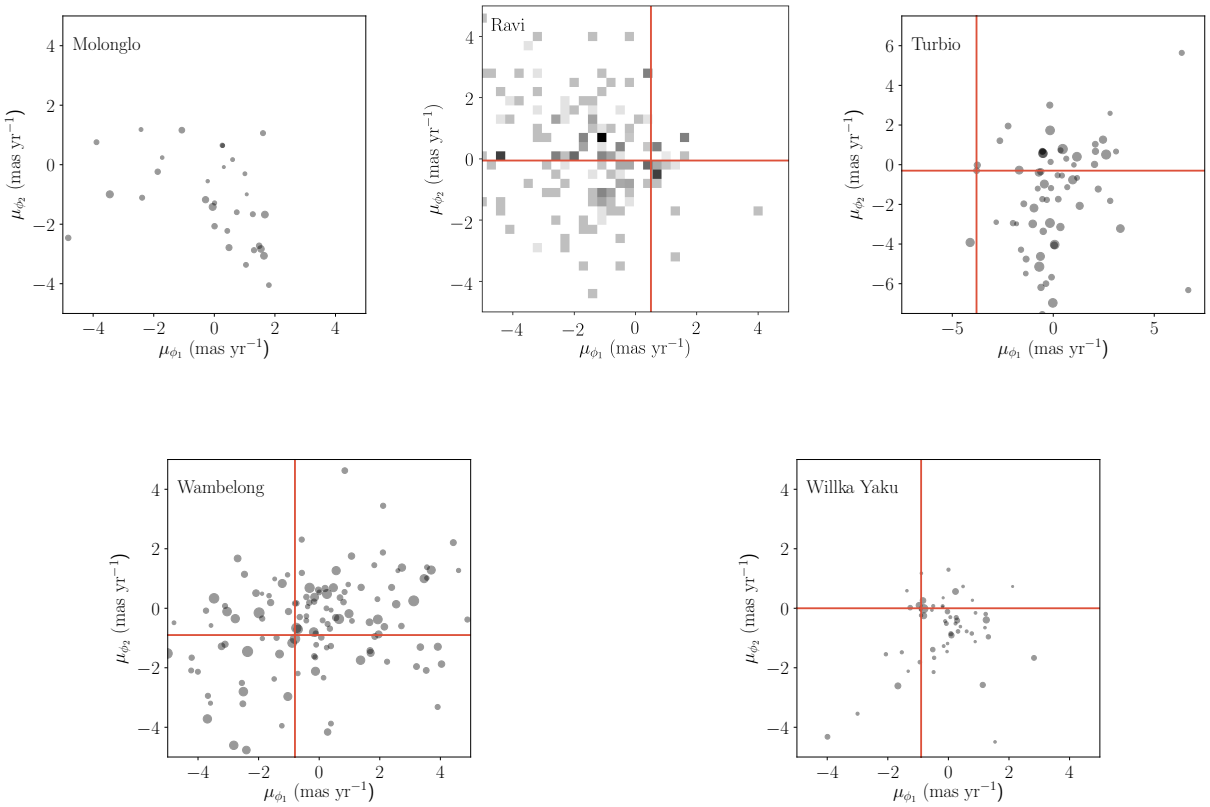

Figure 6.4.2 Low-confidence by-eye proper motion measurements are shown by the orange crosshairs.

Ravi, Turbio, Wambelong, and Willka Yaku (Figure 6.4.2). Early versions of the by-eye measurements were used to target S^5, but the GMM fits to these streams failed to converge. This suggests that these by-eye measurements are less confident than those mentioned previously. Upcoming observations from S^5 should help resolve the proper motions of these streams. We find no promising proper motion signal for Molonglo using either method. The best-fit proper motions and proper motion gradients for all streams are reported in Table 6.3.2, and the by-eye results for all streams, including the low-confidence measurements, are reported in Table 6.A.1.

6.5 Discussion

In this section, we discuss the proper motions of the DES streams individually and as a population. These observations are summarized most concisely in Figure 6.5.1, which compares the proper motions measured here to the stream tracks measured with DES imaging. The black lines show the stream tracks approximated as great circles passing through the endpoints measured in Shipp et al. (2018); the purple arrows show the direction of the proper motion; and the orange line shows the past 1 Gyr of the trailing orbit of the LMC, with the star indicating its present-day position, and the dashed line indicating the segment of the orbit at which the LMC is at a distance beyond 100 kpc. This orbit is performed in the standard `MWPotential2014` from `galpy` (Bovy, 2015) with LMC proper motions from Kallivayalil et al. (2013a), distance from Pietrzyński et al. (2013a), and radial velocity from van der Marel et al. (2002a). In the following subsections, we present a discussion of individual streams (Section 6.5.1) and the influence of the LMC (Section 6.5.2).

6.5.1 Discussion of Individual Streams

Aliqa Uma

Aliqa Uma is a narrow stream that is among the 11 streams discovered in the DES by Shipp et al. (2018). Aliqa Uma lies in a complicated region, bordering the southern end of the ATLAS stream and passing near to the Fornax dwarf galaxy in projection. For this reason, it is difficult to select likely members of Aliqa Uma without contamination from these nearby populations. Aliqa Uma has the lowest Bayes factor of the nine streams presented here, and in fact the Bayes factor is negative. However, confirmation by early S^5 observations merits the inclusion of these measurements among the "high confidence" list.

ATLAS

The ATLAS stream is the most significant narrow stream in the DES footprint. Originally discovered in data from the ATLAS survey (Koposov et al., 2014), this stream extends over $> 30^\circ$ and has been detected by both Pan-STARRS (Bernard et al., 2016) and DES (Shipp et al., 2018). Shipp et al. (2018) note that the track of the ATLAS stream deviates appreciably from a great circle on the sky. Due to the relatively large number of bright stars in ATLAS, it is possible to measure proper motions at multiple positions along the curved track of the stream. We note that the offset between the stream track and the proper motion changes along the path of the stream (Figure 6.5.2).

The ATLAS and Aliqa Uma streams are nearly adjacent, but are offset by $\sim 6^\circ$ in apparent orbital orientation and $\sim 6\,\mathrm{kpc}$ in mean distance (Shipp et al., 2018). However, we find that the reflex-corrected proper motions of these two streams, $\mu'_\alpha \cos\delta, \mu'_\delta = -1.47, 0.78$ mas/yr for ATLAS and $\mu'_\alpha \cos\delta, \mu'_\delta = -0.95, 0.42$ mas/yr for Aliqa Uma, are found to be nearly aligned on the sky (Figure 6.5.1). A potential association has been noted using preliminary radial velocity data from S^5 (Li et al., submitted).

Chenab

The Chenab stream was originally discovered photometrically with data from DES. Recently, using measurements of RR Lyrae stars from *Gaia* DR2, Koposov et al. (2019) showed evidence for a Southern Galactic extension of the Orphan stream that overlaps with Chenab. We independently measure the proper motion of the Chenab stream and find that the proper motions of the RGB stars in Chenab are consistent with those of the RR Lyrae identified by Koposov et al. (2019). We show a comparison between the RGB and RR Lyrae members in Figure 6.5.3.

The association between Chenab and the Orphan stream was initially unclear due to the $> 20^\circ$ offset between their Galactocentric orbital poles (Shipp et al., 2018). Erkal et al. (2019b) showed that this shift in the orbital pole can be caused by the perturbative influence of the LMC. Moreover, this effect is strongest for the southern extension of the Orphan stream, i.e. Chenab, which has passed closer to the LMC than the northern extension. Furthermore, the large number of bright RGB members improves the precision of the proper motions of Chenab to better constrain the mass of the LMC.

Elqui

Elqui is the most distant stream discovered in DES at a distance of $\sim 50\,\mathrm{kpc}$. Shipp et al. (2018) suggest that the location, distance, and orientation of Elqui may be a signature of a possible association with the Magellanic Stream. Though the distance is similar to that of the LMC, we find here from its proper motion that Elqui is moving in the opposite sense to the direction of LMC infall (see Figure 6.5.1). This makes it unlikely that Elqui originated as part of the Magellanic System. It is also unlikely that Elqui would have experienced a temporally extended encounter with the LMC, making it unlikely for the LMC to impart a large gravitational perturbation on the motion of the stream. This is similar to how streams on retrograde orbits are distorted less by the bar (e.g. Hattori et al., 2016) or substructure in

the Milky Way disk (Amorisco et al., 2016) than streams on prograde orbits. Indeed, we see here no significant proper motion offset with respect to the stream track: $\mu_{\phi_2} = -0.03 \pm 0.05$ mas/yr.

Indus

We find that Indus has the largest measured change in proper motion along the stream, with a gradient of $d\mu_{\phi_1}/d\phi_1, d\mu_{\phi_2}/d\phi_1 = 0.05, 0.04$ mas/yr/deg, resulting in a total change of 1.0 and 0.8 mas/yr across the 20° length of the stream, respectively.

Malhan et al. (2018) recover Indus within the *Gaia* DR2 data. They find a proper motion range of $0.50 < \mu_\alpha \cos\delta < 6.0$ mas/yr, $-8.0 < \mu_\delta < -2.0$ mas/yr. We find this to be consistent with our by-eye measurement, given uncertainties and the significant proper motion gradient. Fitting the GMM to proper motions in the observed frame without correcting for solar reflex motion fails to converge due to the large extent and proper motion gradient of Indus.

Bonaca et al. (2019a) find that the track of the Indus stream is matched to an orbit fit of Jhelum, suggesting that the two streams may be multiple wraps of the same system. The proper motions and their gradients reported here may be used to further explore this possible scenario as discussed below.

We observe an offset between the track of Indus and the direction of its proper motion. However, we note that this offset can be accounted for by a change in distance modulus of 0.2 mag, which is within reasonable uncertainty on the distance modulus measurement obtained by isochrone fitting in Shipp et al. (2018).

Jhelum

In on-sky coordinates, Jhelum is the longest (29.2°) and widest (1.16°) stellar stream discovered by DES. We find that the proper motion of Jhelum is best-fit by two distinct components

(Figure 6.5.4). We fit the two proper motion components simultaneously by introducing a second Gaussian stream component to our model with the same spatial prior as the first component, but with an independent proper motion. We label the two components Jhelum-a and -b in Table 6.3.2. The Bayes factor between the two-stream and one-stream models is 13.5, indicating a significant preference for the two-stream model. The proper motion of the Jhelum-a component is found to be in good agreement with the by-eye value. We note that for Jhelum, as for Indus, fitting to the proper motions in the original observed frame without correcting for solar reflex motion fails, and thus these observed frame proper motions are left out of Table 6.3.2. The by-eye measurement in the observed equatorial coordinate frame is included in Table 6.A.1.

We also explored the effect of introducing a distance offset between the two components of the stream. Due to the reflex motion correction, there is a degeneracy between the distance separation of the two components and the observed proper motion offset. We find that the mean proper motions of the two components would converge when corrected for the solar reflex motion at a difference in distance modulus of 0.7 ($m - M = 15.6 \pm 0.35$). We note, however, that such discrepant distances (11 kpc and 15 kpc for the two components) would require a low probability coincidence in alignment between the two components and the line of sight. A smaller distance separation between the two components is possible and could reduce the proper-motion offset slightly.

Interestingly, Bonaca et al. (2019a) recently showed that Jhelum has an extended two-component spatial structure. However, they find the two components to have consistent proper motions. Meanwhile, we measure two distinct proper motion components with consistent spatial distributions. Bonaca et al. (2019a) has explored possible physical scenarios for the formation of the complex morphology of Jhelum. For additional insight into the physical origin of the two populations, we call attention to the extensive work on the Sagittarius dwarf tidal stream(s) which have been noted to be split into at least two roughly parallel

components at slightly different distances in the leading tail in the North (Belokurov et al., 2006a). A similar split was then noted in the trailing tail in the South by Koposov et al. (2012). Navarrete et al. (2017) argue that the two southern components are not different wraps of the Sagittarius stream, but could result from either complex or compound structure within the Sagittarius progenitor, or possibly a past interaction with another system, such as the Cetus Polar stream (Newberg et al., 2009).

The GD-1 stream also has a complex morphology, which may have been caused by past interactions (Carlberg & Grillmair, 2013; de Boer et al., 2018; Price-Whelan & Bonaca, 2018). By analogy, we note the possibility that Jhelum, too, could be either a) a compound structure (two previously bound objects moving on similar orbits) or b) have been originally a single object, which due to a close interaction with another body, becomes split into two or disrupted or tidally extended so that it now appears like an object with a pair or range of proper motions. Radial velocities and velocity dispersion measurements of the Jhelum components, along with more detailed orbital modeling of Jhelum, as well as comparison with other halo objects, may be able to differentiate between possibilities a) and b).

Interestingly, Jhelum is on a nearly polar orbit with respect to the Milky Way disk (Shipp et al., 2018). Erkal et al. (2016b) showed that such streams are the most sensitive to the flattening of the halo if the flattening is aligned with the Milky Way disk. This occurs due to differential precession of the stars in the stream and causes the stream to rapidly fan out. Thus, Jhelum's broad morphology in proper motion could be a sensitive probe of the flattening of the Milky Way halo. This will be revisited in future work with radial velocities from S^5 (Li et al., submitted).

We also consider the possible effect of the Indus stream on Jhelum. The distance modulus of Indus is 16.1, while that of Jhelum is 15.6 (Shipp et al., 2018), a difference in distance, and both are traveling in roughly the same direction (see Figure 6.5.1). Therefore one may consider whether these two streams could have had a close encounter in the past or perhaps

share a common origin. Bonaca et al. (2019a) find that an orbit fit to one component of Jhelum passes through the track of the Indus stream, which may indicate that the two streams are different tidal debris wraps from a common progenitor, or that a close approach has occurred between two distinct streams. A close encounter could explain the double structure of Jhelum, though one would require additional radial velocity information from both systems to more confidently determine their orbital histories.

Phoenix

The Phoenix stream was first discovered by Balbinot et al. (2016) using data from the first year of DES. Compared to the other DES streams, the stellar distribution of Phoenix appears considerably more clumpy; however, none of these overdensities has been conclusively determined to be associated with a Phoenix progenitor. We examine the *Gaia* data for evidence of the structures identified by Balbinot et al. (2016); however, the *Gaia* stars passing our selections are too sparse to resolve any of these excesses.

Grillmair & Carlberg (2016) speculated that the Hermus stream (Grillmair, 2014) may be a northern extension of Phoenix. They predict that if Phoenix-Hermus were one stream on a prograde orbit, it would have a proper motion of $\mu_\alpha \cos\delta, \mu_\delta \sim 2.1, 0.1$ mas/yr, while a retrograde orbit would yield $\mu_\alpha \cos\delta, \mu_\delta \sim 1, -3.5$ mas/yr. Our measured proper motion of $\mu_\alpha \cos\delta, \mu_\delta \sim 2.76 \pm 0.02, -0.05 \pm 0.02$ mas/yr disfavors the retrograde model.

Balbinot et al. (2016) also note a possible association between Phoenix and the nearby globular cluster, NGC 1261. Using proper motion measurements from Dambis (2006), $\mu_\alpha \cos\delta, \mu_\delta = 1.33 \pm 0.89, -3.06 \pm 1.06$ mas/yr, Balbinot et al. (2016) find that NGC 1261 is on an orbit aligned with the path of Phoenix, but offset by $\sim 10^\circ$. Recently, Vasiliev (2019) used *Gaia* DR2 to update the proper motion of NGC 1261, yielding a value of $\mu_\alpha \cos\delta, \mu_\delta = 1.632 \pm 0.057, -2.037 \pm 0.057$ mas/yr (consistent values were determined by Baumgardt et al. 2019). The combination of this updated proper motion measurement for

NGC 1261 and our measurement of the proper motion of the Phoenix stream make it increasingly unlikely that these two systems share a physical origin. However, we do note that the proper motion offset of Phoenix is slightly aligned towards the orbit of NGC 1261.

Tucana III

The Tucana III stream is composed of two tidal tails extending from the Tucana III dwarf galaxy (Drlica-Wagner et al., 2015), and is the only stream in the DES footprint with a definitive progenitor. The proper motion of the Tucana III dwarf galaxy has been measured by several groups: Pace & Li (2019) find $\mu_\alpha \cos\delta, \mu_\delta = -0.03 \pm 0.04, -1.65 \pm 0.04$ mas/yr, Simon (2018) finds $\mu_\alpha \cos\delta, \mu_\delta = -0.014 \pm 0.038, -1.673 \pm 0.040$ mas/yr, and Fritz et al. (2018) find $\mu_\alpha \cos\delta, \mu_\delta = -0.025 \pm 0.034 \pm 0.035, -1.661 \pm 0.035 \pm 0.035$ mas/yr. The Tucana III stream is expected to have a similar proper motion to the dwarf itself. We measure a proper motion for Tucana III, including the core and tidal tails, of $\mu_\alpha \cos\delta, \mu_\delta = -0.10 \pm 0.04, -1.64 \pm 0.04$ mas/yr, which is indeed similar to that of the Tucana III dwarf galaxy. We also find that Tucana III has the largest proper motion gradient of the streams measured here, with $d\mu_{\phi_1}/d\phi_1, d\mu_{\phi_2}/d\phi_1 = 0.12 \pm 0.03, -0.06 \pm 0.03$ mas/yr/deg.

Erkal et al. (2018) fit the orbit of Tucana III based on the track of the Tucana III stream and the line-of-sight velocity from Li et al. (2018), prior to *Gaia* DR2. They argued that the orbit of Tucana III was likely perturbed by a recent close passage with the LMC. They predicted that the LMC would have induced a non-zero proper motion perpendicular to the track of the stream and that this non-zero proper motion could be used to constrain the mass of LMC. However, our measurements show that the proper motion perpendicular to the stream, $\mu_{\phi_2} = -0.03 \pm 0.03$ mas/yr, is consistent with zero. Since the lack of a proper motion perpendicular to the Tucana III stream track would set an upper bound on the mass of the LMC that is inconsistent with other direct measurements (e.g. van der Marel & Kallivayalil, 2014a), we suggest three possible explanations for the discrepancy between

our measurements and the model of Erkal et al. (2018). First, μ_{ϕ_2} is corrected for the solar reflex motion, and is therefore distance-dependent. The apparent lack of a perpendicular proper motion might indicate that Tucana III is more distant than the initial isochrone fits suggest. In fact, a similar suggestion was made by Erkal et al. (2018) based on preliminary measurements of 4 RR Lyrae stars in Tucana III. Second, the lack of offset may be due to the fact that Erkal et al. (2018) fit the orbit with a fixed Milky Way potential. The proper motions will also be sensitive to the potential and the mass of the Milky Way. Third, Erkal et al. (2018) did not consider the reflex motion of the Milky Way caused by the infall of the LMC. As shown in Erkal et al. (2019b), the distance and speed of the Milky Way relative to its present day position and velocity is non-negligible, which will affect the modeling of the proper motion of Tucana III.

Turranburra

Turranburra is a relatively thick stream located at the eastern edge of the DES footprint. The morphology of the stream suggests a dwarf galaxy progenitor; Shipp et al. (2018) predict a progenitor mass of 1.8×10^6 $M_\odot$. Interestingly, in spite of its distance from the LMC, Turranburra also shows an appreciable offset between its track and observed proper motion, which is directed towards the LMC.

Unlike the other eight streams previously mentioned, Turranburra has not yet been fully observed by S^5 and we cannot confirm its proper motion signature with radial velocities. However, we have independently confirmed the proper motion measurement by comparison to the sample of *Gaia* DR2 RR Lyrae published by Iorio et al. (2018). We find 12 RR Lyrae that are likely associated with the stellar stream (see Figure 6.5.5).

The RR Lyrae were selected first along the length of the stream ($|\phi_1| < 8.5^\circ$) and within $|\phi_2| < 5^\circ$. Then, we selected stars within 3 kpc of the distance to Turranburra reported in Shipp et al. (2018). The distances to the RR Lyrae are calculated using Equation 2 in Iorio

et al. (2018). The RR Lyrae passing these simple selections, which are listed in Appendix 6.D, all lie within 2.5° of the stream track, and the majority are tightly clustered around the measured value of the proper motion of the stellar stream.

Ravi

While the Ravi stream was not detected with high confidence in our analysis, we do note an interesting association with the RR Lyrae stream 24.5-1 from Mateu et al. (2018b). The close association in the orbital poles of these two streams was previously noted by Shipp et al. (2018). We take the RR Lyrae stars associated with 24.5-1 as reported by Mateu et al. (2018b), and select stars that lie within 50° along the stream track of the mid-point of Ravi. We determine the median proper motion of these RR Lyrae to be $\mu_\alpha \cos\delta, \mu_\delta \sim 0.6, -1.8$ mas/yr, with a large spread in $\mu_\alpha \cos\delta$ of $\sim$ 0.5 mas/yr. This value is similar to our low-confidence proper motion measurement for Ravi of $\mu_\alpha \cos\delta, \mu_\delta \sim 0.2, -1.6$ mas/yr, particularly given the imprecision of the by-eye measurement, which may be further indication of an association between these two streams.

We also note that Ravi crosses the dwarf galaxy Tucana II (Bechtol et al., 2015; Koposov et al., 2015) in projection, although the galaxy is at a much larger distance. (Tucana II is at a distance of 57 kpc (Koposov et al., 2015), while Ravi is at a distance of 23 kpc.) In order to exclude contamination from Tucana II, we selected only the segment of Ravi with $\phi_1 > 0°$, so that the closest stars to Tucana II are separated from the galaxy by $> 7°$. However, the proper motion we measure for Ravi is similar to that of Tucana II, $\mu_\alpha \cos\delta, \mu_\delta \sim 0.91, -1.16$ mas/yr (Pace & Li, 2019), which could indicate that Tucana II has a very extended stellar distribution that is contaminating our analysis, or that the two systems share similar proper motions despite their large physical separation.

Other Streams

We do not find high-confidence measurements for three other streams: Turbio, Wambelong, and Willka Yaku, and we find no good measurement for Molonglo. We note that these streams reside in complex regions of higher stellar density, either nearer to the Galactic plane, or in areas with other known streams or halo structure. Wambelong is located at $b \sim -30°$, while Turbio and Willka Yaku are both in the vicinity of the Eri-Phe overdensity (Li et al., 2016). Molonglo is both near to the ATLAS stream and stretches into the area covered by the complex, massive Sagittarius stream. The complexity of the stellar foreground in these regions may have contributed to the failure of the the GMM fit to converge on valid proper motion measurements for these streams.

6.5.2 Influence of the LMC

The LMC is the largest satellite of the Milky Way and can significantly perturb the orbits of stellar streams (Erkal et al., 2019b). One possible consequence of a perturbation by the LMC is a misalignment between a stream's track on the sky and the direction of its motion. Erkal et al. (2019b) showed that the observed proper motion of the Orphan stream could be explained by a large gravitational perturbation from the LMC. Observation of the Orphan stream can thus be used to constrain the total mass of the LMC to be $1.38^{+0.27}_{-0.24} \times 10^{11}\,\mathrm{M}_\odot$ (Erkal et al., 2019b). Erkal et al. (2018) hypothesized that such a massive LMC would similarly perturb the Tucana III stream; however, such a perturbation has not been found. The extent of the LMC perturbations on other streams is still unknown, and detailed modeling will be required to develop a self-consistent scenario. However, we can use the observed stream tracks and proper motions to make a qualitative comparison.

We note that we are only considering two dimensions of the stream velocity; it is also possible for these streams to have experienced a perturbation to their radial velocities, which will be explored in more detail by S^5.

The magnitude of the measured proper motion offset for a stream depends on the distance assumed in the solar reflex correction. We find that in addition to Elqui and Tucana III (which show very small proper motion offsets), only Indus has an offset that is consistent with zero given a characteristic uncertainty in distance modulus of 0.2 mag. The other streams would require changes in distance modulus ranging from $\sim 0.5 - 4$ mag to account for the observed proper motion offsets.

A visual inspection of Figure 6.5.1 and Table 6.3.2 gives anecdotal evidence that certain groups of streams may exhibit more significant deflections. Streams with right ascension west of the LMC seem to exhibit larger offsets than those to the east of the LMC. Streams with larger widths, which may be indicative of a dwarf galaxy progenitor, generally seem to have larger offsets as well. In addition, streams with proper motion vectors roughly aligned with the direction of motion along the trailing orbit of the LMC also exhibit larger offsets. These possible relationships must be examined in more detail with radial velocities and detailed modeling. In any case, the offsets seen here indicate that the DES streams are excellent candidates for placing strong constraints on the LMC mass, as well as its shape and radial density profile.

Offsets between the track and direction of motion of stellar streams can also be caused by time-dependent oscillations in the Milky Way's potential due to recent accretion events, as shown by Carlberg (2019). The detailed modeling of stellar streams, which will be possible with the combination of these measurements and radial velocities from S^5, will allow for the separation between the effects of the LMC, which may dominate in the southern sky, and other large-scale time-dependent variations in the Milky Way's potential.

6.6 Conclusions

We present measurements of the proper motions of nine stellar streams in the DES footprint. These measurements confirm that these streams are coherent systems and illustrate the

combined power of *Gaia* DR2 and DES DR1 to measure the velocities of distant, low-surface-brightness streams (out to $\sim 50\,\mathrm{kpc}$). In addition, we have obtained low-confidence measurements of proper motions of four additional streams in the DES footprint. Further velocity measurements, both of proper motions and radial velocities, are necessary to confirm the remaining population of stellar streams discovered in DES and other photometric surveys.

Many of these streams are observed to have significant offsets between the direction of their tracks on the sky and the direction of their proper motions. This observation may indicate that the LMC may have significantly perturbed the orbits of these streams, and suggests that this population of streams may be used to place strong constraints on the mass and the radial profile of the Milky Way's largest satellite. Complete orbit modeling requires full 6D phase-space measurements of each stream. The proper motion measurements in this work have been used to efficiently select targets for the ongoing S^5 spectroscopic survey, which aims to obtain radial velocities and metallicities of 20 streams in the Southern Hemisphere (Li et al. submitted).

In the future, imaging surveys such as LSST (LSST Science Collaboration, 2009) and WFIRST (Spergel et al., 2013) will provide sensitive measurements of fainter and more distant streams. Wide-area spectroscopic surveys, such as DESI (DESI Collaboration et al., 2016), WEAVE (Dalton, 2016), 4MOST (de Jong et al., 2019), and/or MSE (The MSE Science Team et al., 2019) will provide complementary radial velocity measurements. With complete 6D phase space measurements of large populations of stellar streams, it will be possible to place strong constraints on the distribution of mass in our Galaxy, ranging from low-mass subhalos to the total mass of the Milky Way.

6.A By-Eye Results

Here we report the by-eye measurements for all streams, including those with low-confidence measurements (Table 6.A.1). For the nine streams with measurements these values are

consistent, considering the imprecision of the by-eye measurements, with the GMM results.

6.B Selection Parameters

Table 6.B.1 gives the isochrone parameters used in the data selections described in Section 6.2. These were modified from the parameters reported in Shipp et al. (2018), based on visual comparison of high-probability members after a first iteration of the proper motion fit.

6.C Coordinate Transformation Matrices

We used 3×3 rotation matrices to transform positions and proper motions from celestial coordinates to stream coordinates. The entries of these matrices, $R_{i,j}$, are shown in Table 6.C.1.

The matrices are written as,

$$R = \begin{bmatrix} R_{0,0} & R_{0,1} & R_{0,2} \\ R_{1,0} & R_{1,1} & R_{1,2} \\ R_{2,0} & R_{2,1} & R_{2,2} \end{bmatrix} \tag{6.3}$$

Table 6.A.1. By-eye results.

	$\mu_\alpha cos\delta$ (mas/yr)	μ_δ (mas/yr)	μ_{ϕ_1} (mas/yr)	μ_{ϕ_2} (mas/yr)
Aliqa Uma	0.3	-0.6	1.0	-0.2
ATLAS	-0.1	-1.0	1.6	-0.2
Chenab	0.3	-2.4	1.0	-0.5
Elqui	0.1	-0.4	0.6	0.0
Indus	3.5	-5.4	-3.8	0.1
Jhelum	6.9	-5.8	-6.0	-0.8
Phoenix	2.8	-0.1	-1.9	-0.4
Tucana III	-0.1	-1.7	1.1	0.0
Turranburra	0.4	-0.9	0.8	-0.3
Ravi	0.2	-1.6	0.5	-0.1
Turbio	2.3	2.0	-3.8	-0.3
Wambelong	2.0	-0.1	-0.8	-0.9
Willka Yaku	1.1	0.3	-0.9	0.0
Molonglo	...	...	...	...

Table 6.B.1. Isochrone parameters.

Name	$m - M$	Age (Gyr)	Z
Aliqa Uma	17.3	12.5	0.0001
ATLAS	16.8	12.5	0.0001
Chenab	18.0	12.5	0.0001
Elqui	18.5	12.5	0.0001
Indus	16.1	12.5	0.0004
Jhelum	15.6	12.5	0.0001
Molonglo	16.8	13.5	0.001
Phoenix	16.4	12.5	0.0001
Ravi	16.8	13.5	0.0003
Tucana III	17.0	13.5	0.0001
Turbio	16.1	12.5	0.0001
Turranburra	17.2	13.5	0.0003
Wambelong	15.9	11.0	0.0001
Willka Yaku	17.7	11.0	0.0006

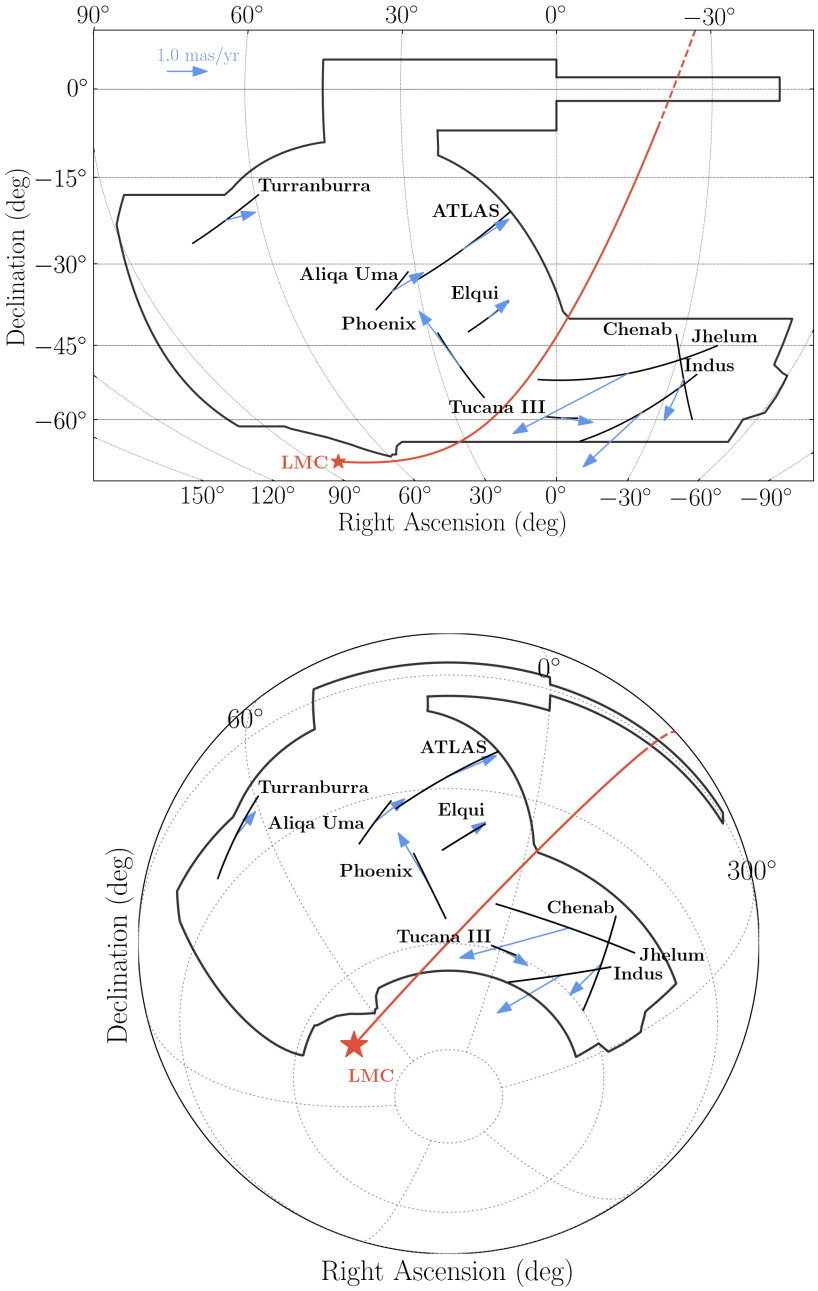

Figure 6.5.1 Proper motions offsets in comparison to the orbit of the LMC (orange line) in two projections. The nine streams with proper motion measurements are shown. All but Tucana III and Elqui show significant proper motion offsets. The black lines indicate the stream tracks, as approximated by a great circle. The arrows show the reflex-corrected proper motions of the streams. The orange line is the trailing orbit of the LMC over the past 1 Gyr, with the current position marked as an orange star, and the dashed line indicating a distance of greater than 100 kpc.

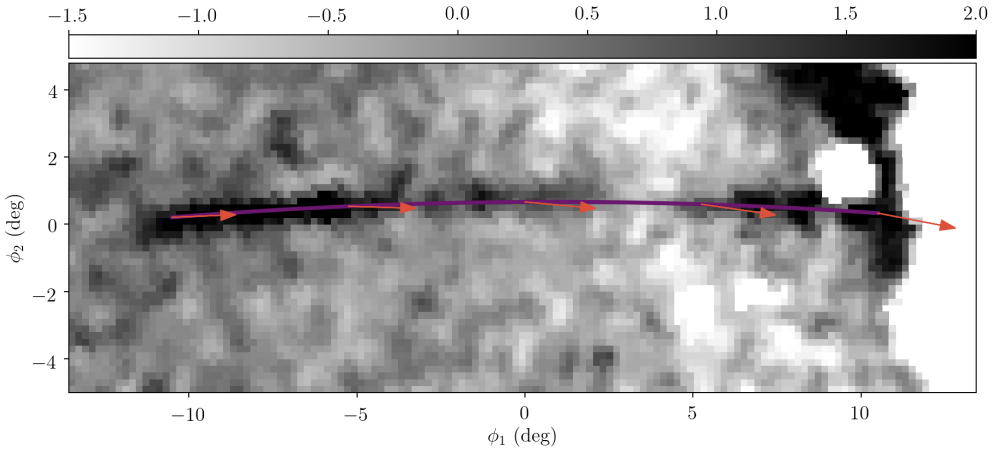

Figure 6.5.2 Proper motions offsets along the track of the ATLAS stream. The purple line indicates the track of ATLAS, and the orange arrows show the direction of the proper motion at points along the stream. The offset between the track and proper motion varies along the length of the stream.

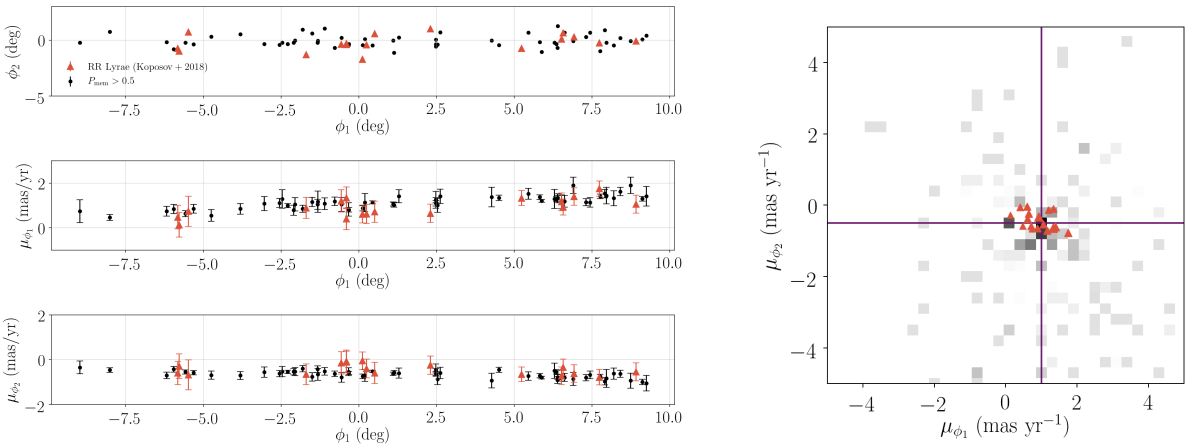

Figure 6.5.3 Comparison between the RGB proper motion measurement of Chenab reported here, and the RR Lyrae members reported by Koposov et al. (2019). The black points are stars with $P_{\rm mem} > 0.5$ from the GMM analysis, and the orange triangles are the RR Lyrae. On the right, the purple crosshair is the GMM proper motion measurement reported here. We find that the high membership probability RGB stars are consistent in proper motion with the reported RR Lyrae members, and generally have smaller proper motion uncertainties.

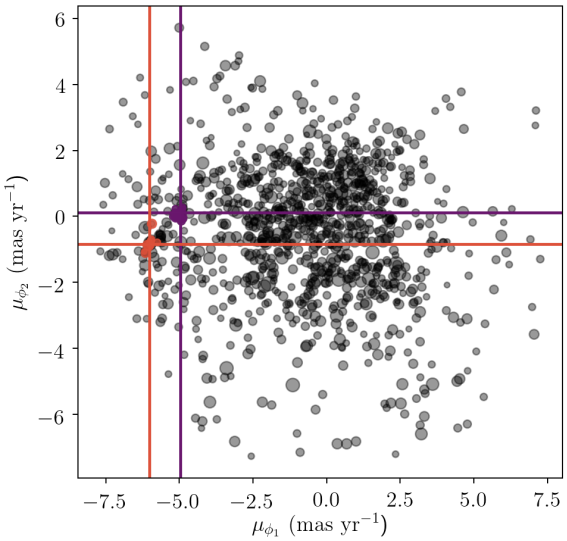

Figure 6.5.4 Proper motion of stars around Jhelum. The black points are the stars passing the by-eye cuts described in Section 6.2. The purple and orange crosshairs indicate the best-fit mean proper motions of the two stream components. The purple and orange points are stars with $P_{\rm mem} > 0.5$ for each of the two components.

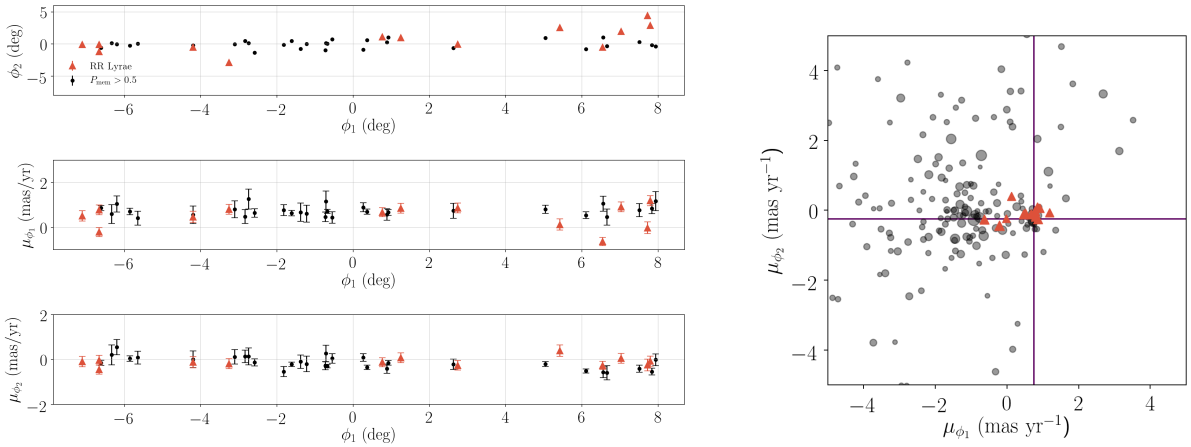

Figure 6.5.5 Comparison between the RGB proper motion measurement of Turranburra, and the RR Lyrae members selected as described in Section 6.5.1. The black points are stars with $\rm P_{mem} > 0.5$ from the GMM analysis, and the orange triangles are the RR Lyrae. On the right, the purple crosshair is the GMM proper motion measurement reported here. We find that the high membership probability RGB stars are consistent in proper motion with the selected RR Lyrae.

Table 6.C.1. Rotation matrix parameters.

Name	$R_{0,0}$	$R_{0,1}$	$R_{0,2}$	$R_{1,0}$	$R_{1,1}$	$R_{1,2}$	$R_{2,0}$	$R_{2,1}$	$R_{2,2}$
Aliqa Uma	0.66315359	0.48119409	-0.57330582	0.74585903	-0.36075668	0.55995440	-0.06262284	0.79894109	0.59814004
ATLAS	0.83697865	0.29481904	-0.46102980	0.51616778	-0.70514011	0.48615660	0.18176238	0.64487142	0.74236331
Chenab	0.51883185	-0.34132444	-0.78378003	-0.81981696	0.06121342	-0.56934442	-0.24230902	-0.93795018	0.24806410
Elqui	0.74099526	0.20483425	-0.63950681	0.57756858	-0.68021616	0.45135409	0.34255009	0.70381028	0.62234278
Indus	0.47348784	-0.22057954	-0.85273321	0.25151201	-0.89396596	0.37089969	0.84412734	0.39008914	0.36780360
Jhelum	0.60334991	-0.20211605	-0.77143890	-0.13408072	-0.97928924	0.15170675	0.78612419	-0.01190283	0.61795395
Molonglo	0.88306113	0.15479520	-0.44299152	0.36694639	-0.81621072	0.44626270	0.29249510	0.55663139	0.77756550
Phoenix	0.59644670	0.27151332	-0.75533559	-0.48595429	-0.62682316	-0.60904938	0.63882686	-0.73032406	0.24192354
Ravi	0.57336113	-0.22475898	-0.78787081	0.57203155	-0.57862539	0.58135407	0.58654661	0.78401279	0.20319208
Tucana III	0.505715	-0.007435	-0.862668	-0.078639	-0.996197	-0.037514	0.859109	-0.086811	0.504377
Turbio	0.52548400	0.27871230	-0.80385697	-0.71193491	-0.37328255	-0.59481831	0.46584896	-0.88486134	-0.00227102
Turranburra	0.36111266	0.85114984	-0.38097455	0.87227667	-0.16384562	0.46074725	-0.32974393	0.49869687	0.80160487
Wambelong	0.07420259	0.76149392	-0.6439107	-0.64686868	-0.45466937	-0.61223907	0.75898279	-0.46195539	-0.45884892
Willka Yaku	0.37978305	0.29001265	-0.87844038	-0.5848418	-0.66046543	-0.47089859	0.71674605	-0.69258795	0.08122206

Note. — All transformations are defined by the stream endpoints reported by Shipp et al. (2018), with the origin located at the center of the stream, apart from that of Tucana III, for which we use the matrix from Li et al. (2018), which centers the stream on the progenitor.

6.D Turranburra RR Lyrae

Table 6.D.1 lists the Gaia DR2 Source ID's of possible RR Lyrae members of Turranburra. The selection of these RR Lyrae is described in Section 6.5.1.

Table 6.D.1. Turranburra RR Lyrae.

Gaia Source ID	α (deg)	δ (deg)
5091448747454278656	64.45486	-21.02018
4881423811590801536	72.81505	-26.62611
4894078026492980480	70.76238	-24.85804
4881772670311841920	73.37994	-25.64553
5097830652242359936	61.52814	-15.87997
5094366743938630016	60.72077	-19.45971
5097133875404904320	61.67817	-17.08474
4881586985989030272	73.82559	-25.84417
4899710545386636160	66.38172	-20.90392
3176477345911441024	62.41282	-14.63724
5096494402017554816	63.44298	-17.42091
4899649801666240896	66.89291	-21.04826
4891992802690351232	68.56002	-26.50784

6.E Stream Members

Table 6.E.1. Probable stream member stars based on proper motion measurements.

Stream	*Gaia* Source ID	α (deg)	δ (deg)	$P_{\rm mem}$
Aliqa Uma	4969932298603707776	34.75908	-33.96308	0.96
Aliqa Uma	4970235699391286016	33.27414	-33.53518	0.82
Aliqa Uma	4970195635936386304	34.31974	-33.42711	0.94
Aliqa Uma	4970244873441388160	33.44620	-33.32170	0.85
Aliqa Uma	4966915105554905344	36.60916	-35.37393	1.00
Aliqa Uma	4966867208079439616	34.85794	-34.74736	0.81
Aliqa Uma	4953555626958854144	39.94765	-37.64483	0.83
Aliqa Uma	4953742509577115520	39.13671	-37.00413	0.98
ATLAS	2350245137034340864	10.19383	-21.12920	0.84
ATLAS	2349268564550587904	12.22904	-22.74946	0.92
...	...	...	...	...

Note. — Member stars are selected with GMM stream membership probability $P_{\rm mem} > 0.8$. The full table is available in the online version in machine-readable format.

CHAPTER 7

MEASURING THE MASS OF THE LARGE MAGELLANIC CLOUD WITH THE S5 STELLAR STREAMS

The text of this chapter is in preparation for submission to ApJ.

7.1 Introduction

The mass of the Large Magellanic Cloud (LMC), the Milky Way's largest satellite galaxy, has proven notoriously difficult to measure. Efforts to directly measure the mass of the LMC from the dynamics of LMC star clusters (Schommer et al., 1992) and the LMC rotation curve (van der Marel & Kallivayalil, 2014a) both yield relatively modest estimates of $\sim 2 \times 10^{10}\,\mathrm{M}_{\odot}$ within $\sim 9\,\mathrm{kpc}$. However, several distinct lines of reasoning suggest that the LMC may have a mass that is up to an order of magnitude larger. First, the LMC's large speed relative to the Milky Way (e.g., Kallivayalil et al., 2006) is consistent with it being on its first passage around the Milky Way (Besla et al., 2007). Given this first passage scenario and the close association of the LMC and the Small Magellanic Cloud (SMC) in both position and velocity, it is reasonable to assume that they were accreted onto the Milky Way together. In order for the SMC to have initially been gravitationally bound to the LMC, the mass of the LMC must be greater than $\sim 10^{11}\,\mathrm{M}_{\odot}$ (Kallivayalil et al., 2013a). Second, accounting for the LMC's effect on the timing argument for the Milky Way and M31, as well as the nearby Hubble flow, gives an LMC mass of $2.5 \times 10^{11}\,\mathrm{M}_{\odot}$ (Peñarrubia et al., 2016). Third, N-body simulations of the LMC on a first-infall orbit favor a massive LMC up to $2.5 \times 10^{11}\,\mathrm{M}_{\odot}$ to explain the warp in the Milky Way's HI disk (Weinberg, 1998; Weinberg & Blitz, 2006; Levine et al., 2006; Laporte et al., 2018). Finally, abundance matching based on the stellar mass of the LMC ($\mathrm{M}_{*} = 2.7 \times 10^{9}\,\mathrm{M}_{\odot}$; van der Marel et al., 2002a) gives a peak halo mass of $\sim 2 \times 10^{11}\,\mathrm{M}_{\odot}$ (Boylan-Kolchin et al., 2010; Moster et al., 2013; Behroozi et al., 2013;

Dooley et al., 2017a,b). These arguments suggest that direct dynamical tracers are only measuring the central region of a much more massive LMC halo.

Stellar streams, the disrupted remnants of dwarf galaxies and globular clusters, provide a direct dynamical tracer of the mass of the LMC at much larger distances. The influence of the LMC on the behavior of stellar streams around the Milky Way was first considered in detail by Law & Majewski (2010), who discussed the interaction of a relatively light LMC ($< 6 \times 10^{10}\,\mathrm{M}_\odot$) with the Sagittarius stream and found that it could have a significant effect. Following the same argument, Vera-Ciro & Helmi (2013) showed that an LMC with a mass of $8 \times 10^{10}\,\mathrm{M}_\odot$ could change the shape of the Milky Way halo inferred by Law & Majewski (2010), making it more spherical. Along these lines, Gómez et al. (2015) found that the infall of a $1.8 \times 10^{11}\,\mathrm{M}_\odot$ LMC would induce a significant reflex motion in the Milky Way, which would affect the Sagittarius stream.

Recently, the Dark Energy Survey (DES) discovered a large number of stellar streams in the southern hemisphere (Shipp et al., 2018). *Gaia* then provided unprecedented measurements of proper motions of greater than 1 billion Milky Way stars, enabling the measurement of the proper motions of the DES streams (Shipp et al., 2019). Many of these streams are close in projection to the LMC, suggesting the exciting opportunity to probe the mass of the LMC at large radii with multiple direct dynamical tracers. Such a measurement was proposed by Erkal et al. (2018), who predicted the effect of the LMC on the Tucana III (Tuc III) stream and found that the LMC could induce a substantial proper motion perpendicular to the track of the stream on the sky. They further argued that the size of this offset could be used to measure the mass of the LMC. Interestingly, the proper motion offset predicted in that paper was not observed by Shipp et al. (2019), using data from *Gaia* DR2 (Gaia Collaboration et al., 2018).

The next attempt to perform this measurement came when Koposov et al. (2019) used data from *Gaia* DR2 to determine that the Orphan stream discovered in SDSS (Grillmair,

2006; Belokurov et al., 2006a) and the Chenab stream discovered in DES (Shipp et al., 2018) likely originated from the same progenitor. Erkal et al. (2019a) proposed that the large-scale wobble of the track of the joint Chenab–Orphan stream, together with the misalignment between the track and proper motion reported by Koposov et al. (2019), could be best explained as a result of an interaction between the stream and the LMC. Furthermore, Erkal et al. (2019a) were able to fit the track of the Chenab–Orphan stream in an aspherical Milky Way potential, including an infalling LMC, to simultaneously measure an LMC mass of $1.38^{+0.27}_{-0.24} \times 10^{11}\,\mathrm{M}_\odot$ and a Milky Way mass of $3.80^{+0.14}_{-0.11} \times 10^{11}\,\mathrm{M}_\odot$ within 50 kpc. Subsequently, Vasiliev et al. (2020) used the Sagittarius stream to simultaneously fit the LMC and Milky Way potential and got an LMC mass of $(1.3 \pm 0.3) \times 10^{11} M_\odot$.

In this paper, we extend the analyses of Erkal et al. (2018) and Erkal et al. (2019a) to five of the DES streams with proper motions measured by *Gaia* EDR3 and radial velocities measured by the Southern Stellar Stream Spectroscopic Survey (S^5; Li et al., 2019). In Section 7.2, we describe the data used in this work. In Section 7.3 we explain how we fit each stream. In Section 7.4, we present our measurement of the LMC mass from each stream. In Section 7.5 we discuss the implications of our results before concluding in Section 7.6.

7.2 Data

The precise modeling of stellar streams requires 6D phase space measurements. Until recently, such measurements were available for only a small number of streams (e.g., Majewski et al., 2004; Koposov et al., 2010; Sesar et al., 2015; Ibata et al., 2016). The S^5 survey, in conjunction with astrometric data from *Gaia* and photometry from DES, has provided unprecedented systematic 6D measurements of over 20 streams in the Southern Hemisphere. Here we provide a brief overview of S^5, and we refer readers to Li et al. (2019) for more details. S^5 uses the Two-degree Field (2dF) fiber positioner (Lewis et al., 2002) coupled with the dual-arm AAOmega spectrograph (Sharp et al., 2006) on the 3.9-m Anglo-Australian

Telescope (AAT). The 2dF provides 392 science fibres that can be distributed across a field of view of $\sim 3\mathrm{deg}^2$. The gratings employed were 580V on the blue arm, and 1700D on the red arm, corresponding to spectral resolutions of ~ 1300 and ~ 10000. The gratings were chosen so that we could have the highest spectral resolution in the red centred on the near-infrared calcium triplet (CaT) lines to derive precise radial velocities of stream members. Both radial velocities (RVs) and stellar atmospheric parameters of each star were derived simultaneously using the `rvspecfit`[1] template fitting code (Li et al., 2019). For each stream field, the average exposure time is about 2 hrs to reach S/N ~ 5 at $r = 18.5$ for RV precision $\sim 1\ \mathrm{km\,s^{-1}}$.

In this study, we consider the southern streams which were observed with AAT by the end of 2018, namely ATLAS, Chenab, Elqui, Indus, Phoenix, Jhelum, Aliqa Uma were observed by S5 in 2018 (Li et al., 2019), while the Tuc III stream was observed with the same setup by an S5 pilot program (Li et al., 2018). We selected five of these streams, ATLAS, Chenab, Elqui, Indus and Phoenix, with which to fit the mass of the LMC. These streams were selected because they have complete 6D phase-space measurements, and they show no signs of significant perturbation beyond the LMC that would require additional model complexity.

We exclude Aliqa Uma, which has been shown to be an extension of the ATLAS stream (Li et al., 2020). Aliqa Uma has been separated from the ATLAS stream by an unknown perturber. Due to the sharp transition between ATLAS and Aliqa Uma, the perturbation was likely caused by the nearby passage of some substructure (Li et al., 2020). Since our fits only include the potential of the Milky Way and the LMC, they are unable to reproduce such features. We also examine the streams observed by S^5 for evidence of perturbation by the Milky Way bar. We do this by including an analytic bar potential, as described in Section 5.2.1 of Li et al. (2020). For each stream, we sample the stream orbital parameters and the bar pattern speed 100 times. For the pattern speed, we use $\Omega = 41 \pm 3\,\mathrm{km\,s^{-1}\,kpc}$ from

1. `https://github.com/segasai/rvspecfit`

Sanders et al. (2019). We compare the resulting stream models by eye to the models excluding the bar, and find that of the S^5 streams, only Tuc III is likely to have been significantly perturbed by the bar. We therefore exclude the Tuc III stream from our analysis. We also exclude the Jhelum stream due to evidence of perturbation reported by Bonaca et al. (2019a) and Shipp et al. (2019). While we exclude these streams from the LMC mass fitting analysis, we do fit models to Tuc III and Jhelum including an LMC mass fixed to $1.5 \times 10^{11}\,\mathrm{M}_\odot$ in order to examine the possible effect of the LMC on these streams (as in Wan et al., 2020; Li et al., 2020).

In order to dynamically model the streams, a clean sample of spectroscopic member stars are needed for the fit. We take the spectroscopic member stars reported in Li et al. (2020) for ATLAS, Wan et al. (2020) for Phoenix, and Li et al. (2018) for Tuc III. These four streams all have narrow spatial widths, small velocity dispersions, and unresolved metallicity dispersions; their progenitors are likely to be globular clusters or very low-luminosity dwarf galaxies. The stream membership is usually unambiguous, and member stars are selected subjectively based on their line-of-sight velocities, proper motions, metallicities, and locations on the color-magnitude diagram in the reference therein.

For the Jhelum, Indus, and Elqui streams that have a large stream width and whose progenitors are likely to be either classical dwarf galaxies or more luminous ultra-faint galaxies, the membership is less obvious since the streams are embedded in foreground contamination. The stream members are therefore determined with a mixture model including multiple multivariate Gaussian components in proper motion, line-of-sight velocity, and metallicity space, detailed in Pace et al. in prep. We selected highly probable members with membership probability, $P_{\mathrm{mem}} > 0.8$ from the mixture models as the stream members for this work. Finally, we consider the Chenab stream. Chenab was identified as the southern extension of the Orphan stream by Koposov et al. (2019). S^5 mapped the entire Chenab–Orphan stream within the DES footprint in 2018, and partially observed some of the northern extension

in 2019 (Li et al., 2019). Throughout this work, we refer to the full observed extent of the Chenab–Orphan stream as Chenab. In this work we use a dataset that combines the S^5 data with data from LAMOST (Zhao et al., 2012) and APOGEE (Majewski et al., 2017) to cover more than 100 degrees along the Chenab stream. For Chenab, rather than fitting individual member stars, we use splines fit to this dataset by Koposov et al. (in prep.) After selecting all stream member stars, we use the RA, Dec, and proper motion measurements from *Gaia* EDR3 and the RVs from S^5 for these individual member stars as input for the modeling. Specifically, the RVs are taken from the second internal data release (DR2.2) which is described in detail in Ji et al. in prep.

Distance is another important component of 6D phase space measurements. Although Shipp et al. (2018) measures the distance for all these streams with isochrone fitting, the distance gradient along the stream is much harder to constrain. In this work, we include the distance measurements from individual blue horizontal branch stars (BHBs) and RR Lyrae stars (RRLs) following the same methods described in Li et al. (2020). We refer readers to the paper for details. In short, we cross match the spectroscopic stream members with the Gaia RRL catalogues (Clementini et al., 2019; Holl et al., 2018) to find the RRL members in these streams. We then determine the distance modulus of RRL stars using the relation from Muraveva et al. (2018) and dereddened Gaia G-band magnitude. The relation is metallicity dependent; we therefore adopt the mean metallicity of each stream from corresponding references for the distance determination. We classify stream members with $g - r < 0.1$ and not in RRL catalogues as BHB members. The distance modulus of each BHB is then calculated using the relation from Belokurov & Koposov (2016) and derenddened DES photometry. We assumed an uncertainty in distance modulus of 0.17 mag from Muraveva et al. (2018) for RRLs, and an uncertainty of 0.1 mag from Deason et al. (2011) for BHBs. We note that we only selected BHB and RRL members from the spectroscopic sample. Although more BHB and RRL members are likely present outside of

AAT fields, especially for the dwarf galaxy streams with large stream widths, we limit our selection to the stars that have line-of-sight velocities available for a purer sample. We list the number of spectroscopic members along with the number of BHBs and RRL members used in each stream in Section 7.4.1 when we discuss individual streams.

7.3 Method

Following the method of Erkal et al. (2019a), we model stream formation and evolution using the modified Lagrange Cloud Stripping (mLCS) technique developed in Gibbons et al. (2014). The method consists of releasing test particles at the Lagrange points of the progenitor, and then evolving them in the combined potential of the the progenitor, the Milky Way and the LMC. As in Erkal et al. (2019a), we model both the Milky Way and LMC as individual particles sourcing their respective gravitational potentials, which is crucial for capturing the response of the Milky Way to the LMC.

We represent the Milky Way potential using the results of McMillan (2017), and evaluate the acceleration from the potential using `galpot` (Dehnen & Binney, 1998). The McMillan (2017) potential includes 6 axisymmetric components, namely bulge, dark matter halo, thin and thick stellar disk, and HI and molecular gas disks. We take the Sun's position and 3D velocity from McMillan (2017). As described in Li et al. (2020); Wan et al. (2020), in order to examine the effects of the choice of Milky Way potential model on our stream fits, we produce ten realizations of this potential by sampling the MCMC chains from the fit in McMillan (2017). We find that the least massive of these realizations ($M_{\rm MW} = 8.3 \times 10^{11} M_\odot$) provides the best fit to the stream data. We provide the potential parameters in Table 7.A in the same format as McMillan (2017).

We model the mass distribution of the LMC as a stellar disk and a dark matter halo. The stellar disk is modelled as a Miyamoto-Nagai disk (Miyamoto & Nagai, 1975) with a mass of $3 \times 10^9 M_\odot$, a scale radius of 1.5 kpc, and a scale height of 0.3 kpc. The orientation

of the LMC disk matches the measurement of van der Marel & Kallivayalil (2014a). The LMC's dark matter halo is modelled as a Hernquist profile (Hernquist, 1990). As in Erkal et al. (2019a), we leave the total mass of the LMC as a free parameter but fix the scale radius to match the circular velocity measurement of 91.7 km/s at 8.7 kpc from van der Marel & Kallivayalil (2014b). Note that this is in agreement with more recent measurements of the LMC's circular velocity (e.g., Cullinane et al., 2020). The total mass and shape of the LMC potential is fixed throughout each simulation, and does not evolve after infall. We account for the dynamical friction of the Milky Way on the LMC using the results of Jethwa et al. (2016). We also fit for the proper motion, distance, and radial velocity of the LMC with priors given by their observed value and uncertainty (Kallivayalil et al., 2013b; Pietrzyński et al., 2013b; van der Marel et al., 2002b).

We model the potential of each stream's progenitor as a Plummer sphere (Plummer, 1911) with a mass and scale radius chosen to match the observed stream width. During the course of tidal disruption, the progenitor's mass decreases linearly in time to account for tidal stripping. The majority of the streams considered in this work do not have a known progenitor, so we assume that the progenitor has completely disrupted, i.e., that its present day mass is zero. Furthermore, we assume that the remnant of the progenitor is in the middle of each stream's observed extent. The only exception is Tuc III, which is one of the few streams known to be associated with a bound progenitor. For this stream, we require a bound progenitor to remain at present day, positioned at $(\phi_1, \phi_2) = (0^\circ, 0^\circ)$ in the stream coordinates of Tuc III. For each stream, we examined the effect of moving the progenitor off of the observed length of the stream in each direction and found no significant effect on the measured LMC mass.

We calculate the likelihood of each stream model by producing mock observations of the simulated stream and comparing them with the data set described above. For each stream model, we calculate the track on the sky, the radial velocity, the proper motions in RA and

Dec, and the distance as functions of ϕ_1, the observed angle along the stream. The likelihood is calculated for each S^5 member star, as described in Section 3.2 of Erkal et al. (2019a), using simulated particles within $\pm 1^\circ$ in ϕ_1 of each S^5 member. When calculating the likelihood for the stream track and the radial velocity, we include additional nuisance parameters, which allow for marginalization over the stream width (σ_{ϕ_2}) and radial velocity dispersion ($\sigma_{\rm vr}$). This allows for slight variations in the stream model to better fit the observed data without varying the progenitor mass. We assign the mass of each progenitor in order to roughly reproduce the observed width of each stream by eye. The progenitor parameters are listed in Table 7.A.

We perform a Markov Chain Monte Carlo (MCMC) fit using `emcee` (Foreman-Mackey et al., 2013). Our model includes 12 free parameters, namely the ϕ_2 position, distance, radial velocity, and proper motion of the progenitor at present day, the stream track and radial velocity nuisance parameters, and the proper motion, radial velocity, distance, and total mass of the LMC. The position of the progenitor along the stream is fixed to $\phi_1 = 0^\circ$ for all streams (i.e., the middle of the stream's observed extent). The only exception is Chenab, where the progenitor is placed at $\phi_1 = 6.34^\circ$ in the coordinate system from Erkal et al. (2019a); Koposov et al. (2019). This is near the center of the full Chenab stream, and is the same progenitor position as Erkal et al. (2019a). The prior distributions on each parameter are listed in Table 7.3. The upper limit of our prior on the LMC mass is selected to ensure that the LMC is on its first infall within our Milky Way potential.

As a demonstration of how the data and stream models look, we show the best-fit model to the ATLAS stream in Figure 7.3.1. The red points are the S^5 members and the blue points represent the stream model. Similar figures for the other streams are included in Appendix 7.A. This shows that the best-fit model can recover all of the observed trends in the ATLAS stream.

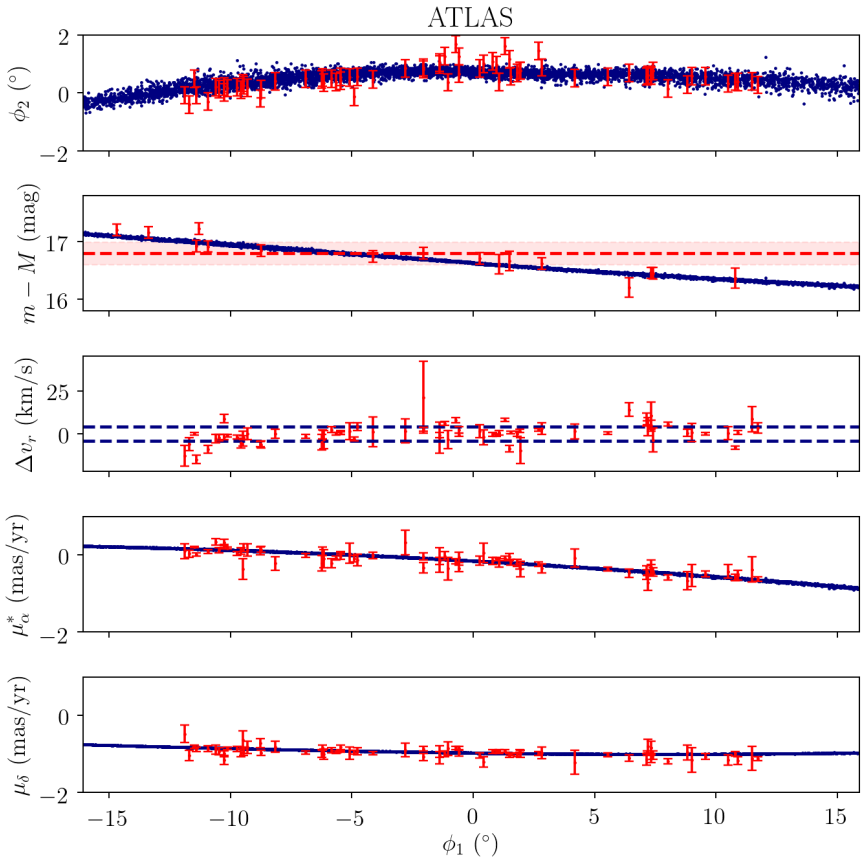

Figure 7.3.1 Model fit to the ATLAS stream. The simulated stream is shown in blue, and the S^5 members included in the MCMC fit are plotted in red. In the first panel, we plot the track in stream coordinates (ϕ_1, ϕ_2), calculated using the rotation matrices from. Shipp et al. (2019) and the RA and Dec measurements from Gaia EDR3. The error bars on the data represent the $\sigma_{\rm track}$ parameter included in the likelihood calculation. In the second panel, we show the distance modulus along the stream. The dashed red line and shaded region represent the distance measurement from Shipp et al. (2018) with a 0.2 mag uncertainty, and the individual points represent the BHB and RRL distance tracers included in the fit. In the third panel, we plot the difference between the measured and model radial velocity at the ϕ_1 position of each member star. The separation of the blue dashed lines is equal to $\pm\sigma_{\rm vr}$. The fourth and fifth panels show the proper motions of the model and the measured proper motions of the S^5 member stars from the *Gaia* EDR3 dataset. Similar figures for each stream are included in Appendix 7.A.

Table 7.3.1. Priors on MCMC fit parameters.

Parameter	Prior	Range	Units	Description
$\phi_{2,\mathrm{prog}}$	Uniform	(-1, 1)	deg	Vertical spatial placement of the progenitor in stream coordinates.
$\sigma_{\phi_2,\mathrm{prog}}$	Uniform	(0, 2)	deg	Nuisance parameter accounting for uncertainty in stream spatial width.
$v_{\mathrm{r,prog}}$	Uniform	(-300, 300)	km/s	Radial velocity of the progenitor.
$\sigma_{\mathrm{v_r,prog}}$	Uniform	(0, 20)	km/s	Nuisance parameter accounting for uncertainty in stream velocity dispersion.
$(m-M)_{\mathrm{prog}}$	Normal	$(m-M)_0 \pm 0.2$	mag	Distance modulus of the progenitor.
$\mu_{\phi_1,\mathrm{prog}}$	Uniform	(-10, 10)	mas yr^{-1}	Proper motion of the progenitor along the stream.
$\mu_{\phi_2,\mathrm{prog}}$	Uniform	(-10, 10)	mas yr^{-1}	Proper motion of the progenitor perpendicular to the stream.
M_{LMC}	Log-Uniform	(2, 30)	$10^{10} M_\odot$	Total mass of the LMC.
$\mu_{\alpha,\mathrm{LMC}}$	Normal	1.91 ± 0.02	mas yr^{-1}	Proper motion of the LMC in RA.
$\mu_{\delta,\mathrm{LMC}}$	Normal	0.229 ± 0.047	mas yr^{-1}	Proper motion of the LMC in Dec.
$v_{\mathrm{r,LMC}}$	Normal	262.2 ± 3.4	km/s	Radial velocity of the LMC.
d_{LMC}	Normal	49970.0 ± 1126.0	pc	Distance of the LMC.
M_{prog}	Fixed	–	$M_\odot$	Mass of the progenitor (see Tab. 7.A).
$r_{\mathrm{s,prog}}$	Fixed	–	kpc	Scale radius of the progenitor (see Tab. 7.A).

Note. — Priors on the twelve free parameters in the MCMC stream model fits. $m - M_{\mathrm{measured}}$ is the distance modulus reported in Table 1 of Shipp et al. (2018).

7.4 Results

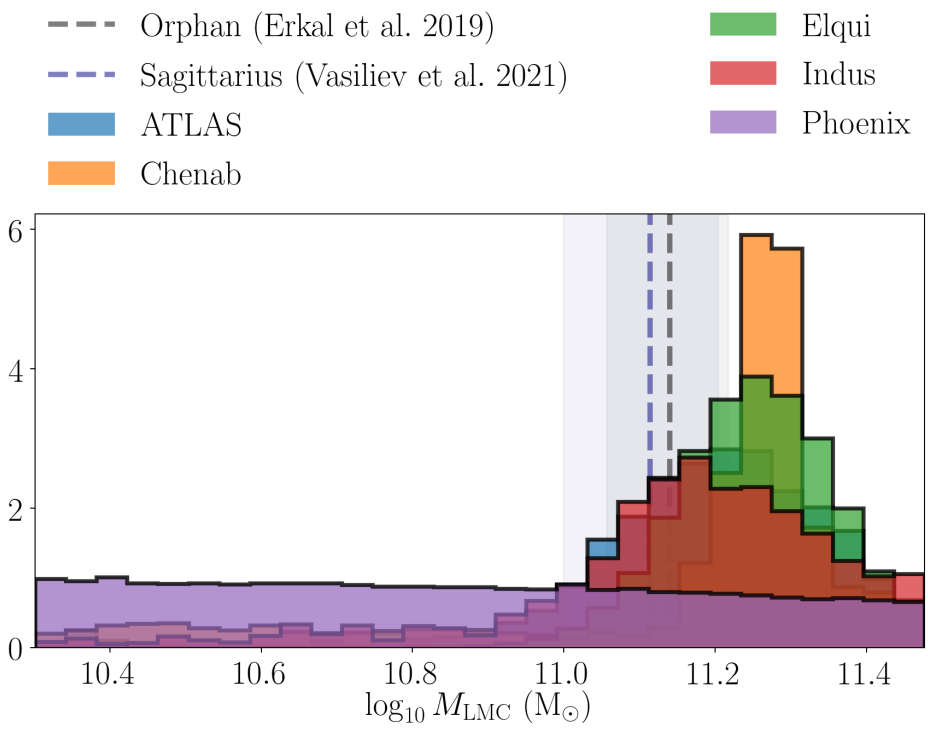

Figure 7.4.1 Marginalized posterior distributions on the total LMC mass from fits to each of the five streams. The gray vertical dashed line and shaded region show the constraint on the LMC mass from the fit to the Chenab stream in Erkal et al. (2019a), and the blue dashed line and. shaded region represent the measurement using the Sagittarius stream by Vasiliev et al. (2021).

Following the method described above, we fit models to each stream and obtain five independent constraints on the total mass of the LMC. In this section, we present the measurements of the mass of the LMC, and discuss the details of the interaction between each stream and the LMC in order to develop a consistent picture of how the Milky Way's largest satellite has perturbed this population of stellar streams.

The constraints on the LMC mass are presented in Table 6.3.2 and Figure 7.4.1. Constraints on the other progenitor and LMC parameters are included in Table 7.A. In Figure 7.4.1, each color represents the posterior distribution on the LMC mass resulting from the fit to each stream and marginalized over the other fit parameters. The gray shaded region

Table 7.4.1. LMC mass measurements and orbital parameters.

Stream	$M_{\rm LMC}$ ($10^{11}\,M_\odot$)	$r_{\rm approach}$ (kpc)	$v_{\rm approach}$ (km/s)	$t_{\rm approach}$ (Myr)
ATLAS	$16.1^{+5.8}_{-4.6}$	23.9	467.1	80.0
Chenab	$18.18^{+2.60}_{-10.20}$	25.4	371.2	310.0
Elqui	$18.0^{+4.6}_{-3.8}$	11.2	419.6	99.0
Indus	$17.3^{+6.5}_{-5.9}$	38.0	268.5	10.5
Phoenix	$6.9^{+10.8}_{-4.0}$	30.7	433.9	49.2
Tucana III	-	4.2	382.4	98.8
Jhelum	-	40.6	367.2	2.8

represents the best-fit LMC mass and uncertainty from an analysis of the Chenab stream (Erkal et al., 2019a), and the blue shaded region represents LMC mass inferred from fits to the Sagittarius stream (Vasiliev et al., 2021). Generally, the results are consistent with each other to within 1σ and with the two previous measurements. We note that the posterior distribution for the Phoenix stream is very broad and provides no meaningful constraint on the LMC mass. Each of these results and the variations between them can be placed into context by examining the orbit of each stream relative to the LMC.

Given the orbits of each stream, we can predict the magnitude of the perturbation on the system by the LMC. Streams that pass close to the LMC with a small relative velocity are predicted to experience the strongest perturbation. For each stream, Table 6.3.2 lists the distance of closest approach to the LMC, the relative velocity between the stream and the LMC at closest approach, and the time at which this interaction occurs. With these parameters, we can predict the magnitude of the perturbation, as illustrated in Figure 7.4.3.

Figure 7.4.3 shows the distance of closest approach and the relative velocity for several points along each stream, spaced by $0\overset{\circ}{.}1$ in ϕ_1. The curves represent lines of constant perturbation strength, assuming the interaction is impulsive, using the results of Section 3.1 of Erkal & Belokurov (2015a),

$$\Delta v = \frac{GM}{bw}, \tag{7.1}$$

where b is the impact parameter, w is the relative velocity, and Δv is the velocity kick

to the stream. Streams that pass very close to the LMC with a small relative velocity are predicted to experience the largest perturbation, therefore Tuc III, Elqui, and Chenab should experience a more significant perturbation by the LMC than ATLAS, Phoenix, Indus, and Jhelum.

The interaction geometry is also an important consideration in predicting the effect of the LMC on each stream since different perturbation geometries will affect different observables. Given the precise measurements of the proper motions, radial velocities, stream tracks from *Gaia* and S^5, and the relative imprecision of the distance measurements, we will most easily be able to identify perturbations manifesting as changes to the stream proper motion and track.

We can characterize the observable effect of the LMC on a given stream by approximating the perturbation as a velocity kick towards the LMC at the point of closest approach. We then break down this velocity kick into components along the direction of the angular momentum, radial, and tangential vectors of the stream's orbit with respect to the Milky Way. This geometry is illustrated in Figure 7.4.2. Velocity kicks out of the orbital plane, along the direction of the angular momentum vector of the stream's orbit, will produce an offset between the track of the stream and the direction of the proper motion, which can be precisely measured with the S^5 and *Gaia* data. Kicks in the radial direction will manifest as an offset between the radial velocity and the distance gradient, which is more difficult to measure due to the difficulty in measuring distances along each stream. Perturbations aligned with the stream's velocity will be the most difficult to measure.

The color scale in Figure 7.4.3 represents the projection of the predicted perturbation in the angular momentum direction. Since perturbations in this direction are the most easily observable, this is a proxy for how observable the LMC's effect will be for the streams in our data set. Figure 7.4.4 gives a more detailed view of the three components of the predicted perturbations. Streams with the largest kicks in the angular momentum direction (yellow)

are predicted to provide the strongest constraints on the LMC mass, while streams with small perturbations overall, or where the perturbations are primarily in the radial or tangential directions will provide weaker constraints. Interestingly, Chenab and ATLAS have the largest predicted perturbations out of the orbital plane, which coincides with the significant proper motion offsets measured for these streams (e.g., Erkal et al., 2019a; Koposov et al., 2019; Shipp et al., 2019; Li et al., 2020).

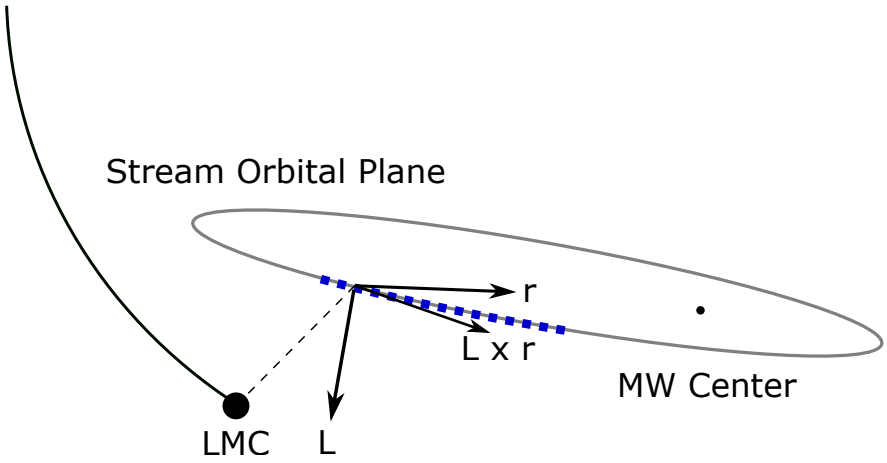

Figure 7.4.2 Diagram illustrating the interaction geometry between a stream and the LMC. The black dashed line represents the vector between the stream and the LMC at closest approach. We decompose this vector into components aligned with the angular momentum vector of the stream's orbit ($\hat{L}$), the radial vector between the stream and the Galactic center ($\hat{r}$), and a third perpendicular vector tangential to the stream's orbit ($\hat{L} \times \hat{r}$).

Another way to examine the predicted and measured effect of the LMC on each stream is to compare the orientation of the stream to the direction of motion (e.g., Erkal et al., 2019a; de Boer et al., 2020; Li et al., 2020). Unperturbed streams roughly follow simple orbits and move in the direction in which they are extended. By combining *Gaia* and S^5 data, we can compare the direction of motion to the extension of each stream in two ways. First, we can compare the track of the stream on the sky to the direction of its proper motion. Second, we can compare the distance gradient along the stream (along ϕ_1) to the ratio of the radial velocity and the proper motion in the ϕ_1 direction. These comparisons

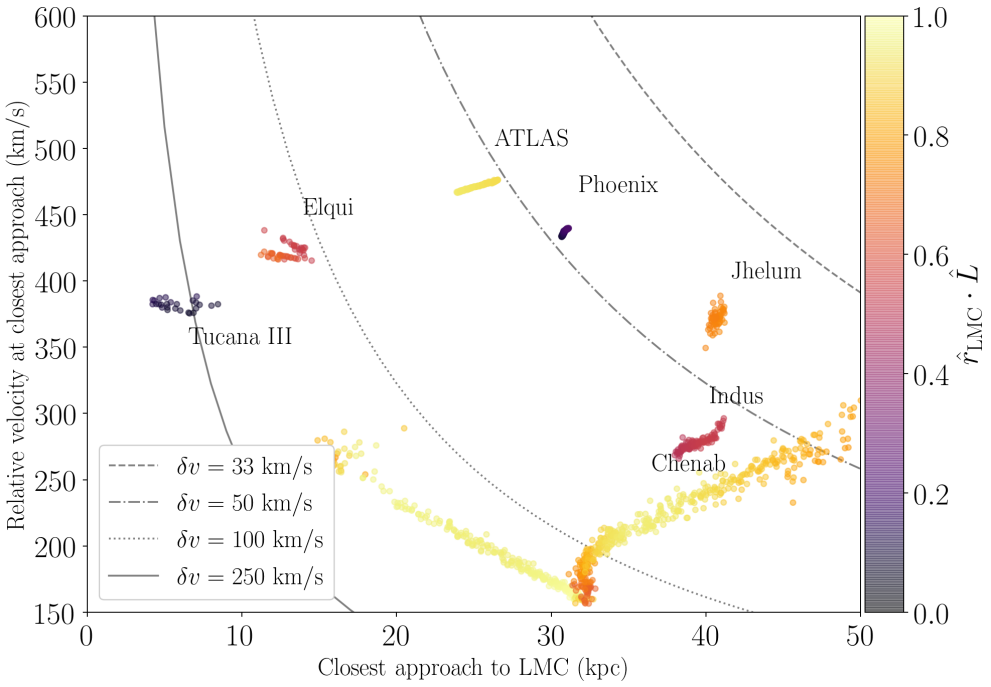

Figure 7.4.3 Predicted perturbation by the LMC on each stream. The x-axis shows the distance of closest approach, and the y-axis is the relative velocity at closest approach. For each stream, we plot points spaced by 0.°1 in ϕ_1. The curves represent lines of constant perturbation, assuming the interaction is impulsive. The color represents the component of the velocity kick in the direction of the angular momentum vector. Kicks in this direction present as offsets between the stream track and the proper motion direction, which are most easily measurable given currently available data.

are illustrated in Figures 7.4.5 and 7.4.6. The lines in these figures are each fit using cubic splines, following the MCMC method described in Section 3.1 of Erkal et al. (2017). The shaded bands represent the 1σ uncertainties resulting from the MCMC spline fit.

Figure 7.4.5 shows the offsets between the stream tracks and the direction of the proper motion for each stream in the model (blue) and the data (red). In each figure the dashed lines show the slope of the stream track ($\frac{d\phi_2}{d\phi_1}$), and the solid lines represent the ratio of the reflex-corrected proper motions ($\mu_{\phi_2}/\mu_{\phi_1}$) along the stream. We note that in this ratio we have used the quantity $\mu_{\phi_1} = \frac{d\phi_1}{dt}$, which does not have a $\cos\phi_2$ term. Unperturbed streams should have no offset between the solid and dashed lines, while streams perturbed out of their orbital plane are predicted to have a significant offset. The offsets in the models

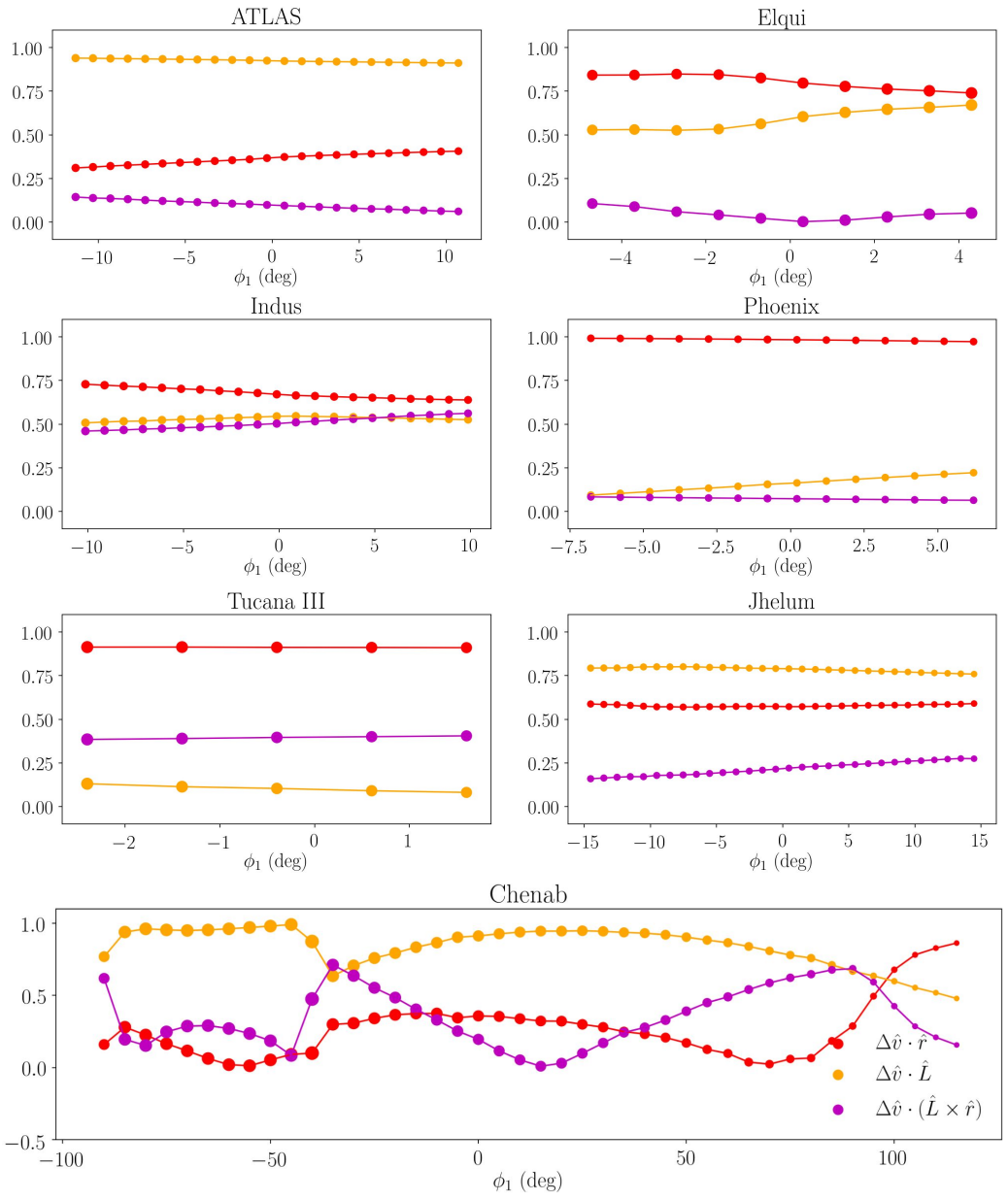

Figure 7.4.4 Velocity kicks in three directions for each stream, assuming an impulsive interaction. Yellow represents the direction of the angular momentum of the stream orbit, orange represents the radial direction (towards the center of the Milky Way) and purple represents the direction tangential to the stream orbit. Offsets in the angular momentum direction are the most visible given currently available data. Therefore, streams with large offsets in that direction, such as Chenab, are predicted to provide the strongest constraint on the LMC mass.

roughly match the scale of the corresponding offsets in the data. Differences in the shapes of the curves may be due to lack of complexity in the model (e.g., additional small-scale perturbations), or the effect of the progenitor as $\phi_1 = 0°$. In the data (red), Chenab, ATLAS, and Elqui have the largest offsets between the two lines (note the differing axis scales between panels), which is consistent with the predictions illustrated in Figure 7.4.4.

Figure 7.4.6 shows the offsets in the radial direction. Here, the dashed line represents the distance gradient along the stream ($\frac{dr}{d\phi_1}$), while the solid line represents the ratio of the reflex-corrected radial velocity to the reflex-corrected proper motion along the stream (v_r/μ_{ϕ_1}). Once again, unperturbed streams should show no offsets between these two lines, while streams perturbed in the radial direction should show significant offsets. The stream with the largest predicted offset in the model is Tuc III. This suggests that with improved distance measurements, and accounting for the possible affect of the Milky Way bar, we may be able to use Tuc III to place strong constraints on the mass of the LMC.

7.4.1 Individual Streams

ATLAS

The ATLAS stream is a narrow stellar stream that was first discovered in the VST ATLAS survey (Koposov et al., 2014), and further studied with deeper data from DES (Shipp et al., 2018), and with spectroscopic data from S^5 (Li et al., 2020).

Our model of the ATLAS stream is fit to the 72 S^5 members identified by Li et al. (2020). In addition, we include distance measurements to 13 BHBs and 5 RRLs in the calculation of the likelihood. The best-fit model for ATLAS is shown in Figure 7.3.1. As noted in Section 7.3, we exclude Aliqa Uma, which has been shown to be an extension of the ATLAS stream (Li et al., 2020), separated by a small perturber which has passed close to the stream.

Our fit to the ATLAS stream provides a measurement of $M_{\rm LMC} = 16.1^{+5.8}_{-4.6} \times 10^{10} M_\odot$. Li et al. (2020) also fit a model to the ATLAS stream, including an LMC with a fixed mass

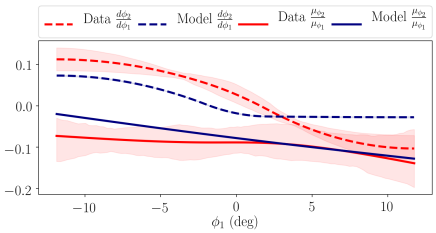

(a) ATLAS

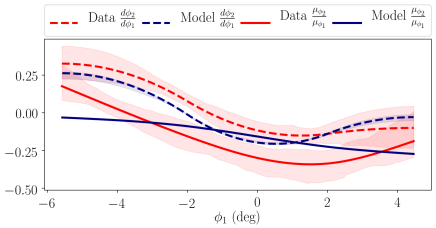

(b) Elqui

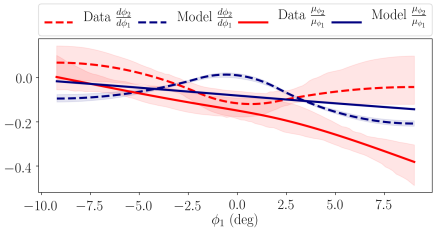

(c) Indus

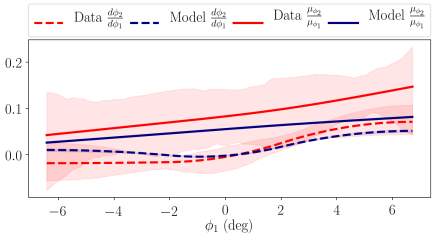

(d) Phoenix

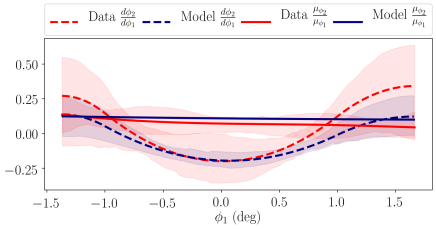

(e) Tucana III

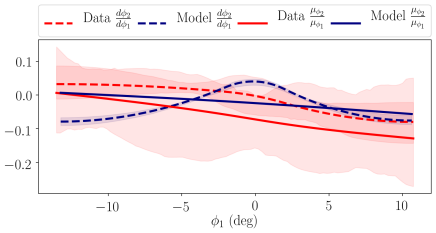

(f) Jhelum

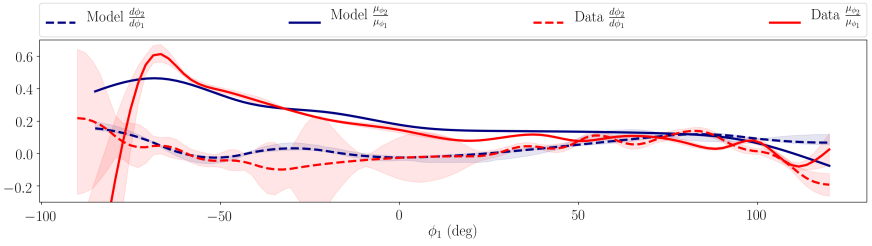

(g) Chenab

Figure 7.4.5 Offsets between the proper motion and the track of each stream. Solid lines represent the ratio of the proper motions ($\mu_{\phi_2}/\mu_{\phi_1}$), and the dashed lines represent the slope of the track on the sky. Blue lines correspond to the model, and red lines correspond to the S^5 data. For an unperturbed stream on a simple orbit, these two lines will be aligned. However, several of these streams show some offset. Chenab, as predicted, has the largest proper motion offset, in both the data and the model.

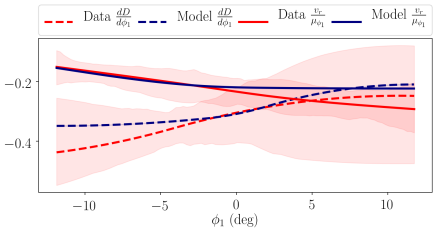

(a) ATLAS

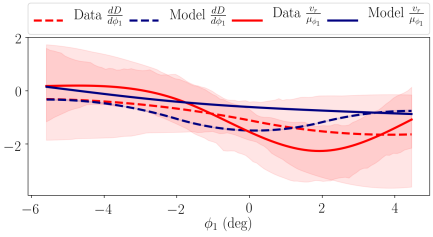

(b) Elqui

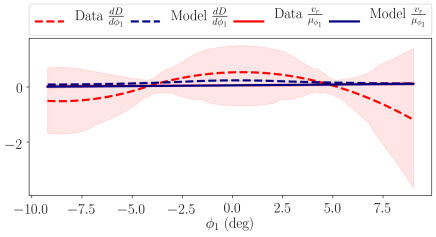

(c) Indus

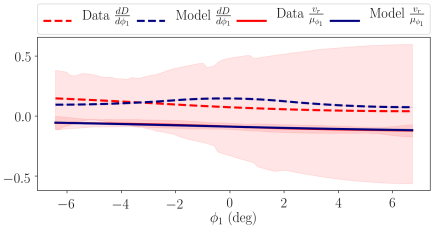

(d) Phoenix

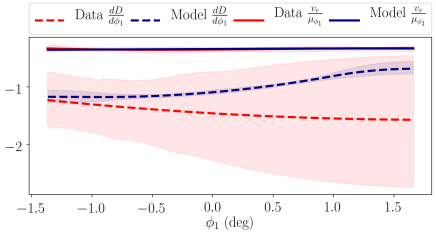

(e) Tucana III

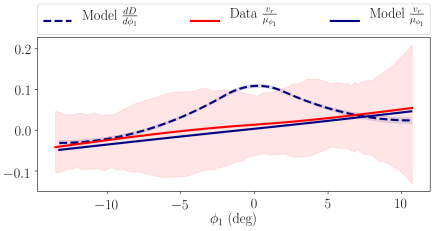

(f) Jhelum

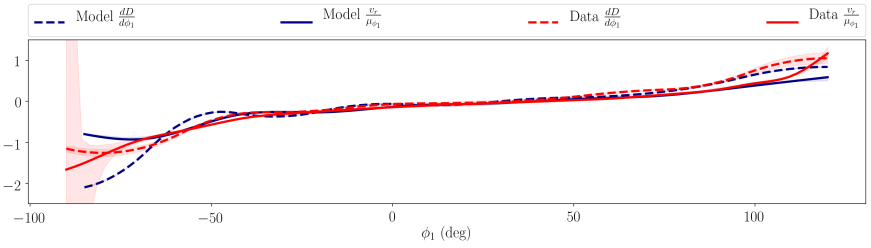

(g) Chenab

Figure 7.4.6 Offsets between the radial velocity and distance gradient of each stream. Solid lines represent the ratio of the radial velocity to the proper motion (v_r/μ_{ϕ_1}) along each stream, and the dashed lines represent the distance gradient. As in the above figure, blue lines correspond to the model, and red lines correspond to the data. None of the streams have sufficient data to measure a significant offset between the two red lines. Tuc III is the only stream with a large predicted offset in the model. We find that the magnitude of this offset increases with larger LMC masses.

of $1.5 \times 10^{11} M_{\odot}$. This is within 1σ of our LMC mass measurement, and it is therefore unsurprising that Li et al. (2020) obtained a good fit to the ATLAS stream including this fixed LMC mass and that their derived orbital properties are consistent with our best-fit orbit.

Figure 7.4.3 and Figure 7.4.4 show that ATLAS has one of the smaller predicted total perturbations, but one of the larger perturbations out of its orbital plane, suggesting that the majority of the perturbation should be observable as an offset between the track and proper motion of ATLAS. This is consistent with the large observed proper motion offset in ATLAS (Shipp et al., 2019; Li et al., 2020), and explains why ATLAS provides a strong constraint on the LMC mass.

Chenab

Chenab was first discovered in DES by Shipp et al. (2018) and was later determined to be an extension of the Orphan stream by Koposov et al. (2019). Here we fit the full observed stream, using splines fit to data from S^5, LAMOST, and APOGEE (Koposov et al. in prep.).

The southern component of Chenab has one of the largest predicted total perturbations by the LMC, and the largest along its angular momentum vector. Therefore, Chenab is expected to provide the strongest constraint on the LMC mass of the 5 streams included in this work. As seen in Figure 7.4.1, Chenab does in fact provide one of the tightest constraints.

Figure 7.4.3 illustrates how the impact of the LMC on Chenab varies along the length of the stream. The strongest predicted impact is along the southern portion of the stream. This part of the stream is also most significantly perturbed out of its orbital plane (Figure 7.4.4), which is consistent with the large proper motion offset seen in Figure 7.4.5. Fardal et al. (2019) identify a misalignment between the spatial track and velocity vector along the northernmost component of the stream, which is consistent with the offset shown at large ϕ_1 in Figure 7.4.6. At $\phi_1 > 125^{\circ}$, we see an offset in both the data and the model between

the distance gradient and the ratio of the radial velocity to the proper motion along the stream, which suggests the stream is curving away in distance at a greater rate than would be expected along an unperturbed orbit.

We obtain a best-fit value of $M_{\rm LMC} = 18.18^{+2.60}_{-10.20} M_\odot$, which differs from the result of Erkal et al. (2019a) by $< 1\sigma$. This offset may be due to differences in dataset or model. We discuss the possible sources of this difference in greater detail Section 7.5.

Elqui

Elqui was discovered by Shipp et al. (2018) in the DES data, and is the most distant of the DES stellar streams at 50 kpc. Elqui has 43 S^5 members and 3 BHBs and 5 RRLs, which we fit to constrain the mass of the LMC to $M_{\rm LMC} = 18.0^{+4.6}_{-3.8} \times 10^{10} M_\odot$. Elqui passes within 15 kpc of the LMC and shows signs of significant perturbation. In particular, the track of Elqui appears to deviate from the great circle connecting the two endpoints (Figure 7.A.1). This deviation can be reproduced by a model including a massive LMC, but cannot be reproduced if the LMC is excluded. Elqui has a significant predicted perturbation in the angular momentum direction, but the largest predicted velocity kick is in the radial direction. This suggests that with improved distance measurements we may be able to use Elqui to place an even stronger constraint on the LMC mass.

Elqui is measured to have a large velocity dispersion of $\sim 13\,{\rm km\,s^{-1}}$. For comparison, streams with similar predicted progenitor masses, such as Indus, have typical velocity dispersions of $\sim 3\,{\rm km\,s^{-1}}$. This large dispersion is also present in the best-fit stream model. This is despite the fact that our progenitor for Elqui is dynamically cold, with a mass of only $M_{\rm proj} = 10^6\,{\rm M}_\odot$. This indicates that the measured stream dispersion does not necessarily map directly onto the dispersion of the progenitor system. It seems unlikely that this unusually large dispersion is due to perturbation by the LMC, as it does not significantly decrease with decreasing LMC mass. The large dispersion may be due to the high orbital

eccentricity of Elqui. The source of this large dispersion requires further investigation.

Shipp et al. (2018) proposed a possible connection between Elqui and the Magellanic stream, due to the similar distance and orientation of Elqui. Shipp et al. (2019) showed that the proper motion of Elqui is inconsistent with an association with the Magellanic stream. We further support this conclusion here, noting that at closest approach Elqui has a velocity relative to the LMC of $\sim 420\,\mathrm{km\,s^{-1}}$, indicating that it cannot be bound to the Magellanic system.

Indus

The Indus stream is a thick stream discovered by Shipp et al. (2018) in DES. Indus has 59 S^5 members including 4 BHBs and 1 RRL, which we fit to measure an LMC mass of $M_{\mathrm{LMC}} = 17.3^{+6.5}_{-5.9} \times 10^{10} M_{\odot}$. Of the 5 streams used to fit the LMC mass, Indus has the largest distance of closest approach to the LMC. However, it passes by at a slow relative velocity and with a geometry such that the predicted velocity kick in the angular momentum direction is similar in magnitude to that of ATLAS or Elqui. Indus is predicted to have experienced a radial perturbation equal in magnitude to its perturbation out of its orbital plane. Indus also has only a small number of known distance tracers, and therefore a large uncertainty in its distance gradient. Given the large width of Indus, it is likely that additional distance tracers lie outside the limits of the S^5 footprint. With an improved measurement of the distance gradient, it is likely that Indus can provide an even stronger constraint on the LMC mass.

Phoenix

Phoenix is a narrow stream discovered in the DES data by Balbinot et al. (2016) and further studied by Shipp et al. (2018). Significant density variations of unknown origin have been identified along the stream (Balbinot et al., 2016, Tavangar et al. in prep.). These variations

are unlikely to be due to a large-scale perturbation by a system like the LMC. Wan et al. (2020) found that Phoenix has a very low metallicity ([Fe/H] = -2.7), suggesting that Phoenix represents the tidal debris of the most metal-poor globular cluster known to date.

Phoenix has the least sensitivity to the LMC mass of the five streams, as seen in Figure 7.4.1. We fit the 30 S^5 members of Phoenix, as published in Wan et al. (2020), and 3 BHBs to obtain an LMC mass measurement of $M_{\rm LMC} = 6.9^{+10.8}_{-4.0} \times 10^{10} M_\odot$. It is unsurprising that Phoenix provides a weaker constraint on the LMC mass than the other streams, for two primary reasons. First, the Phoenix stream has the smallest predicted velocity kick from the LMC, as shown in Figure 7.4.3. Only Indus has a larger distance of closest approach to the LMC, and Phoenix passes by the LMC with a much larger relative velocity. Second, the orientation of the Phoenix stream relative to the LMC suggests that the majority of the velocity kick is in the radial direction, as seen in Figure 7.4.4, and is thus very difficult to detect with current observations. This suggests that with an improved distance gradient we may be better able to measure the effect of the LMC on the Phoenix stream, and perhaps tighten the constraint on the mass of the LMC.

Tucana III

Tuc III was discovered in the first year of DES data by Drlica-Wagner et al. (2015) and consists of thin tidal tails extending from a central progenitor. We exclude Tuc III from this analysis due to its probable interaction with the Milky Way bar, as discussed in Section 7.3. However, Tuc III is an interesting stream to consider in the context of the LMC since it passes within 10 kpc of the LMC. We fit a model to Tuc III including an LMC with a mass fixed to $1.5 \times 10^{11}\,{\rm M}_\odot$, motivated by the results of Erkal et al. (2019a).

Erkal et al. (2018) modeled the Tuc III stream and predicted the proper motion offset that would be revealed with the release of *Gaia* DR2. They predicted a large value of the reflex corrected proper motion perpendicular to the stream, μ_{ϕ_2}, would be observed for any

LMC mass greater than $\sim 10^{10} M_{\odot}$. However, the observed proper motion is found to be generally aligned with the track of the stream (Shipp et al., 2019). This inconsistency may be a result of how the Milky Way potential was modeled by Erkal et al. (2018). The LMC is known to induce a significant reflex motion in the Milky Way (e.g., Gómez et al., 2015; Garavito-Camargo et al., 2019; Erkal et al., 2020b; Petersen & Peñarrubia, 2021); however, Erkal et al. (2018) fixed the centroid of the Milky Way potential, which may have biased the fits to Tuc III and thereby the predictions for μ_{ϕ_2}. In this paper, we allow the center of the Milky Way to move in response to the LMC, and find that we are able to obtain a good fit to the data without a significant proper motion offset. Instead, we find that Tuc III is predicted to have a large offset between its radial velocity and distance gradient (see Figure 7.4.6). This predicted offset suggests that a precise measurement of the distance gradient along Tuc III, along with an understanding of the effects of the Milky Way bar, may enable strong constraints on the LMC mass. However, improved distance gradient measurements are difficult due to the distance and low luminosity of the stream. Therefore, despite Tuc III's close passage to the LMC its utility as a probe of the LMC mass is unclear.

Jhelum

Jhelum is a thick stream discovered in the DES data by Shipp et al. (2018). As with Tuc III, we have excluded Jhelum from our analysis due to the evidence of perturbation presented by Bonaca et al. (2019a) and Shipp et al. (2019). In particular, Bonaca et al. (2019a) identified two distinct spatial components in Jhelum—a thin dense component and a broader, more diffuse component—while Shipp et al. (2019) identified two distinct proper motion components in Jhelum in the *Gaia* data. The cause of this unique morphology remains unknown. Despite this evidence of perturbation, we fit a model to Jhelum with a fixed LMC mass of $1.5 \times 10^{11}\,\mathrm{M}_{\odot}$ in order to explore the predicted impact of the LMC. We find that Jhelum is not predicted to be significantly perturbed by the LMC.

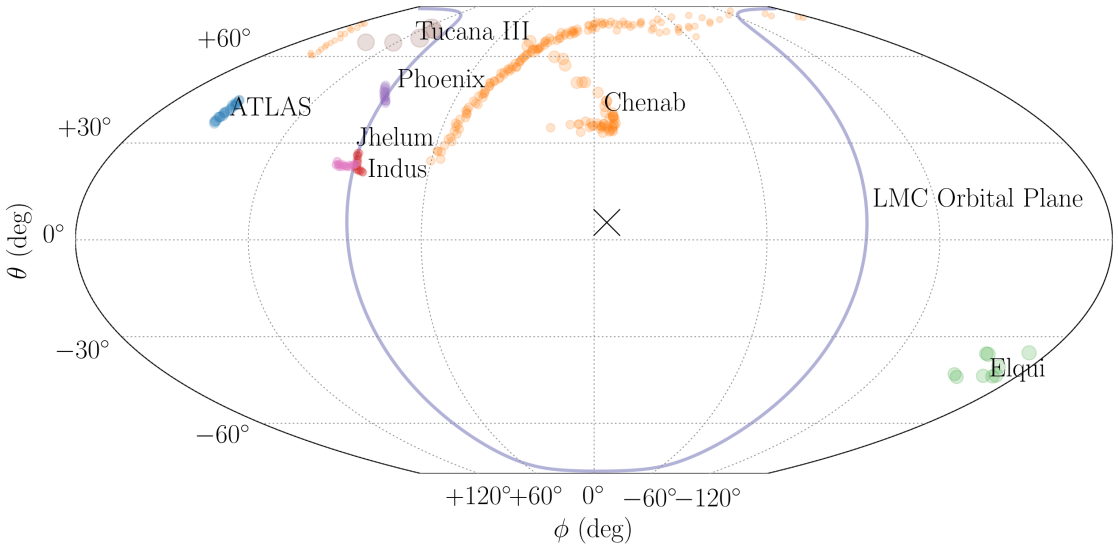

Figure 7.4.7 The position around the LMC at which each stream passes at closest approach. θ and ϕ represent the polar angles of the closest approach of each stream as viewed from the center of the LMC. The coordinate system is identical to Galactocentric coordinates shifted to the center of the LMC. The cross shows the direction of the LMC's orbital angular momentum and the blue line shows the plane of the LMC's orbit around the Milky Way. Most of the streams pass to the north of the LMC, while Elqui passes below the galaxy. Each stream probes a different part of the LMC potential, by passing by at a different position, distance, and time. Ultimately we will be able to use a large population of streams to constrain the disrupting, asymmetrical potential of the LMC.

7.5 Discussion

We have fit the mass of the LMC independently using 5 stellar streams with data from S^5, *Gaia* EDR3, and DES DR1. In Section 7.4, we present the constraint on the LMC mass from each of these fits (Figure 7.4.1), and discuss the unique interactions between each stream and the LMC (Figures 7.4.3 and 7.4.4). Here, we place these measurements in context. We discuss how these measurements begin to establish a consistent picture of the influence of the Milky Way's largest satellite on the population of southern stellar streams, draw comparisons to other measurements, and discuss future efforts to model a realistic LMC and Milky Way potential.

As discussed in Section 7.4, due to the precision of the *Gaia* proper motion measurements, our data are most sensitive to perturbations out of the stream orbital plane, which produce observed misalignments between stream tracks and proper motions. Therefore, by combining the results of Figure 7.4.3 and Figure 7.4.4, which demonstrate the predicted magnitude and geometry of the perturbation of the LMC on each stream, we can predict the ability of each stream to constrain the mass of the LMC. These predictions suggest that Chenab, followed by Elqui, ATLAS, and Indus should have the largest observed proper motion offsets and should provide there strongest constraints on the LMC mass. In fact, these are the streams that we find provide the strongest constraints. Streams with large offsets in other directions may require additional data in order to better constrain the LMC mass. For example, Tuc III, Elqui, and Phoenix all have large predicted offsets in the radial direction, which are detectable only with precise measurements of the distance gradient along the stream. This suggests that the constraints on the LMC mass with each of these streams may show significant improvement with improved distance measurements, which may be obtained in the future with additional distance tracers, deeper photometric data, or the extension of precise parallax measurements to more distant sources. Given these predictions, it is also unsurprising that Phoenix does little to constrain the LMC mass, given it has both the

smallest predicted total perturbation, and is predicted to have been perturbed primarily in the radial direction.

By examining the orbits of each stream relative to the LMC, we have assembled a consistent picture of the effect of the LMC on this population of stellar streams. This consistency supports our measurements of a massive LMC with $M_{\rm LMC} \sim 1.5 \times 10^{11}\,{\rm M}_\odot$. We find that all of the streams considered in this work, with the exception of Phoenix, prefer a total mass of the LMC equal to or greater than this value, supporting an LMC with a mass of $\sim 15\%$ that of the Milky Way.

7.5.1 Comparison to Previous Measurements

Prior to this work, two streams have been used to fit the mass of the LMC — Chenab (Erkal et al., 2019a) and Sagittarius (Vasiliev et al., 2021). Erkal et al. (2019a) measured an LMC mass of $1.38^{+0.27}_{-0.24} \times 10^{11}\,{\rm M}_\odot$, and Vasiliev et al. (2021) obtained a consistent measurement of $M_{\rm LMC} = 1.3 \pm 0.3 \times 10^{11}\,{\rm M}_\odot$.

As mentioned in Section 7.4.1, our fit to Chenab is a particularly interesting comparison to the results of fitting the same stream by Erkal et al. (2019a). In this work, Chenab prefers an LMC mass of $18.18^{+2.60}_{-10.20} \times 10^{10}\,{\rm M}_\odot$, which differs from the result of the Erkal et al. (2019a) by $< 1\sigma$. This may be due in part to the fact that we are fitting a different dataset, and in particular that Erkal et al. (2019a) did not include radial velocities in their likelihood. In fact, the Erkal et al. (2019a) best-fit model does not match the S^5 radial velocity measurements along the southern portion of the stream.

Another important distinction is that we do not vary the Milky Way potential, whereas Erkal et al. (2019a) allow the mass, shape, and orientation of the Milky Way to vary; they find that the Chenab stream prefers a substantially asymmetric halo shape. Similarly, Vasiliev et al. (2021) find that the Sagittarius stream prefers a twisted dark matter halo that is aligned with the Milky Way disk in the inner halo but flattened in an almost perpendicular

direction in the outskirts. This suggests that further work on simultaneously fitting multiple streams in a flexible joint Milky Way and LMC potential is necessary in order to entangle the complex interplay between the LMC and Milky Way potentials.

7.5.2 Shape of the LMC

The LMC is also known to have an asymmetric potential and in fact is disrupting as it orbits the Milky Way (e.g., Garavito-Camargo et al., 2019, 2020; Petersen & Peñarrubia, 2020). In this work we have used a simplified model of the LMC. We have modeled the potential of the LMC as a spherical Hernquist profile, while in reality the LMC potential is more complex. A more realistic model of the LMC potential is necessary to explore the full complexity of the interactions between the LMC and Milky Way stellar streams. The fact that the LMC is a complex, non-spherical, disrupting system suggests that the S^5 streams may experience very different effects from the LMC depending on which part of the galaxy they pass by and at what time.

To explore this idea further, Figure 7.4.7 shows the predicted point of closest approach of each stream relative to the LMC. Each stream probes a different part of the LMC potential, and notably Elqui passes on the opposite side of the LMC from the other streams. In this figure we also show the orbital plane of the LMC around the Milky Way (blue line). Since the LMC material spreads out the most within this plane (e.g. see Fig. 10 in Erkal et al., 2019a), the streams closest to this plane likely experience a stronger LMC force field than those farther away. As we continue to build up our dataset, our population of streams, and the complexity of our models, we may be able to use each of these streams to measure not only the total mass of the LMC, but its disrupting, asymmetrical radial profile.

7.6 Conclusions

The dynamical influence of the LMC on structures in the Milky Way has been the focus of much recent work (e.g., Erkal et al., 2018, 2019a, 2020b; Erkal & Belokurov, 2020; Vasiliev et al., 2020; Petersen & Peñarrubia, 2021). In this contribution, we measure the LMC mass with five streams observed by S^5 in the Southern Galactic hemisphere. These streams are sensitive to the LMC due to their proximity. Previous work (Shipp et al., 2019) has shown that many of these streams have proper motions misaligned with their stream tracks, a telltale sign of a perturbation to the stream (e.g., Erkal et al., 2019a). We find the mass to be $\sim 1.5 \times 10^{11} M_{\odot}$, consistent with previous measurements of the LMC mass with stellar streams (Erkal et al., 2019a; Vasiliev et al., 2021). By examining the interaction between each individual stream and the LMC we can build a consistent picture of how the Milky Way's largest satellite has perturbed the population of stellar streams.

In order to understand the constraining power of each stream, we used a simple model which assumes the velocity kick imparted by the LMC is impulsive. We then decomposed the predicted velocity kicks into three directions relative to each stream's orbital plane: aligned with the angular momentum direction (i.e., perpendicular to the stream plane), in the radial direction (i.e., towards the Milky Way), and the tangential direction (i.e., along the stream). We found that the streams with the most stringent constraints on the LMC mass have significant velocity kicks which are perpendicular to the stream plane since these are visible as a misalignment between the proper motion direction and stream track.

Our best-fit models predict that several streams (Tuc III, Elqui, and Phoenix) are expected to have a significant misalignment along the line of sight. This alignment should be observable by comparing their distance gradient with the ratio of the radial velocity to the proper motion along the stream. These are currently not measurable due to the relatively large uncertainty in distance compared to the other observables. With improved measurements of radial velocities and distance gradients in the future we should be able to more

precisely measure the impact of the LMC in the radial direction. The detection of this misalignment will allow us to better constrain the LMC mass with these streams.

Although the main result of this work is that we can successfully model all of the streams with an LMC of mass $\sim 1.5 \times 10^{11} M_{\odot}$, there are a number of additional avenues for exploration. First, we have varied the LMC mass but we have kept the Milky Way fixed. Fitting these streams, along with streams from the Northern Galactic hemisphere, will likely provide strong constraints on the shape of the Milky Way's dark matter halo. Second, we have neglected the tidal deformation of the Milky Way and LMC which may have a substantial effect on these streams. Interestingly, the streams considered in this work approach the LMC from a variety of directions (see Fig. 7.4.7), suggesting that they will be a powerful probe of any deformations of the LMC. Further study of the complexity of the Milky Way and LMC potential will build upon this work to reveal a more complete picture of the effect of the Milky Way's largest satellite on our Galaxy.

7.A Model Parameters

Table 7.A.1. Stream progenitor and LMC parameters.

Parameter	ATLAS	Chenab	Elqui	Indus	Phoenix	Tucana III	Jhelum
$\phi_{2,\mathrm{prog}}$ (deg)	0.73	-0.77	0.31	0.30	-0.11	-0.10	0.01
$\sigma_{\phi_2,\mathrm{prog}}$ (deg)	0.30	–	0.18	0.48	0.11	0.07	0.29
$v_{\mathrm{r,prog}}$ ($\mathrm{km\,s^{-1}}$)	-110.09	96.97	-57.60	-52.83	47.61	-102.26	-5.35
$\sigma_{\mathrm{v_r,prog}}$ ($\mathrm{km\,s^{-1}}$)	4.06	–	13.60	4.83	3.14	0.89	18.41
d_{prog} (*kpc*)	21.22	18.78	52.85	15.77	17.29	23.97	12.79
$\mu_{\alpha,\mathrm{prog}}$ (mas $\mathrm{yr^{-1}}$)	-0.40	4.25	-0.56	-5.74	-0.92	0.21	-7.13
$\mu_{\delta,\mathrm{prog}}$ (mas $\mathrm{yr^{-1}}$)	-0.90	1.95	-0.32	-1.27	-2.55	-1.60	-3.15
M_{LMC} ($10^{10}\,\mathrm{M_\odot}$)	16.04	18.18	17.95	17.21	6.93	15.00	15.00
$v_{\mathrm{r,LMC}}$ ($\mathrm{km\,s^{-1}}$)	262.51	263.91	263.93	261.78	262.13	262.20	262.20
d_{LMC} (kpc)	49.48	51.36	48.44	50.19	50.05	49.97	49.97
$\mu_{\alpha,\mathrm{LMC}}$ (mas $\mathrm{yr^{-1}}$)	1.91	1.92	1.91	1.91	1.91	1.91	1.91
$\mu_{\delta,\mathrm{LMC}}$ (mas $\mathrm{yr^{-1}}$)	0.21	0.36	0.17	0.22	0.23	0.23	0.23
M_{prog} ($\mathrm{M_\odot}$)	2×10^4	1×10^7	1×10^6	1×10^7	2×10^4	2×10^3	2×10^7
$r_{\mathrm{s,prog}}$ (kpc)	0.01	0.5	0.1	0.1	0.01	0.05	0.1

Note. — Progenitor and LMC parameters for the best-fit stream models. Note that for Tucana III and Jhelum, all LMC parameters were fixed. For all streams, M_{prog} and $r_{\mathrm{s,prog}}$ were fixed. See parameter descriptions in Table 7.3.

Table 7.A.2. Stream orbital parameters.

Parameter	ATLAS	Chenab	Elqui	Indus	Phoenix	Tucana III	Jhelum
r_{peri} (kpc)	12.8	16.4	10.2	13.0	13.1	0.8	10.5
r_{apo} (kpc)	40.0	76.0	66.4	21.6	18.4	49.1	71.2
ϕ (deg)	349.2	190.4	344.7	125.7	61.8	322.9	119.5
ψ (deg)	114.9	137.8	90.9	110.4	119.9	71.5	97.7

Note. — Orbital parameters of the best-fit stream models. ϕ and ψ are the Galactocentric azimuthal and polar angles of the orbital pole, respectively.

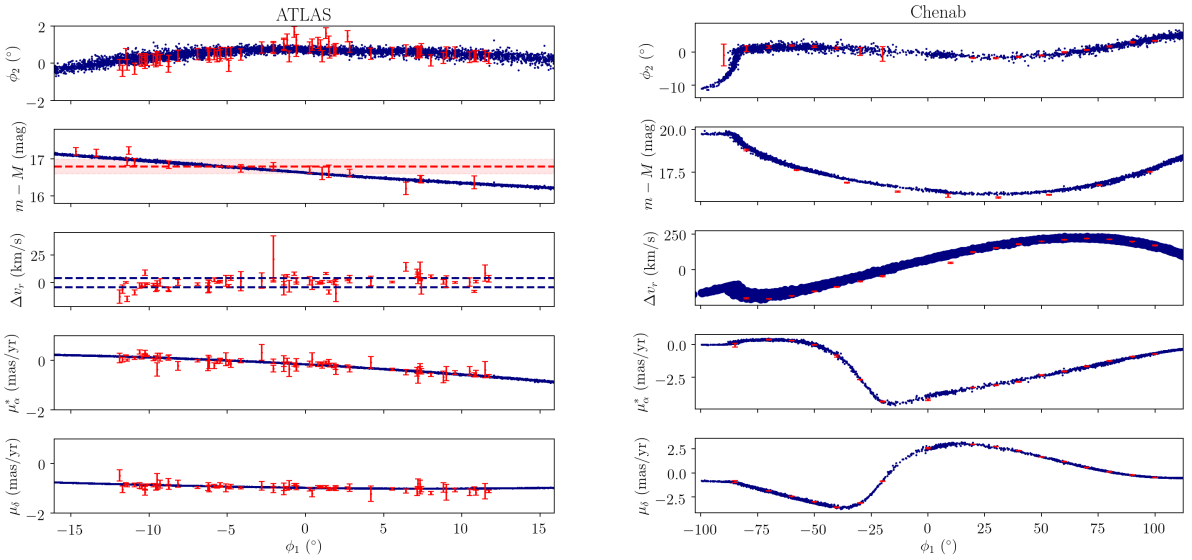

(a) (b)

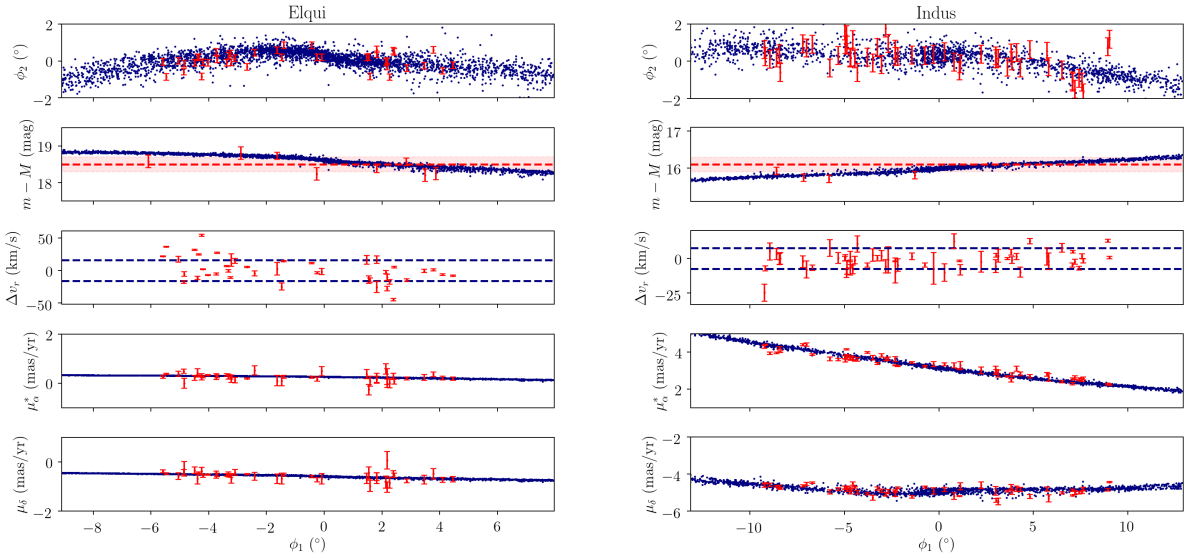

(c) (d)

Figure 7.A.1 Stream models.

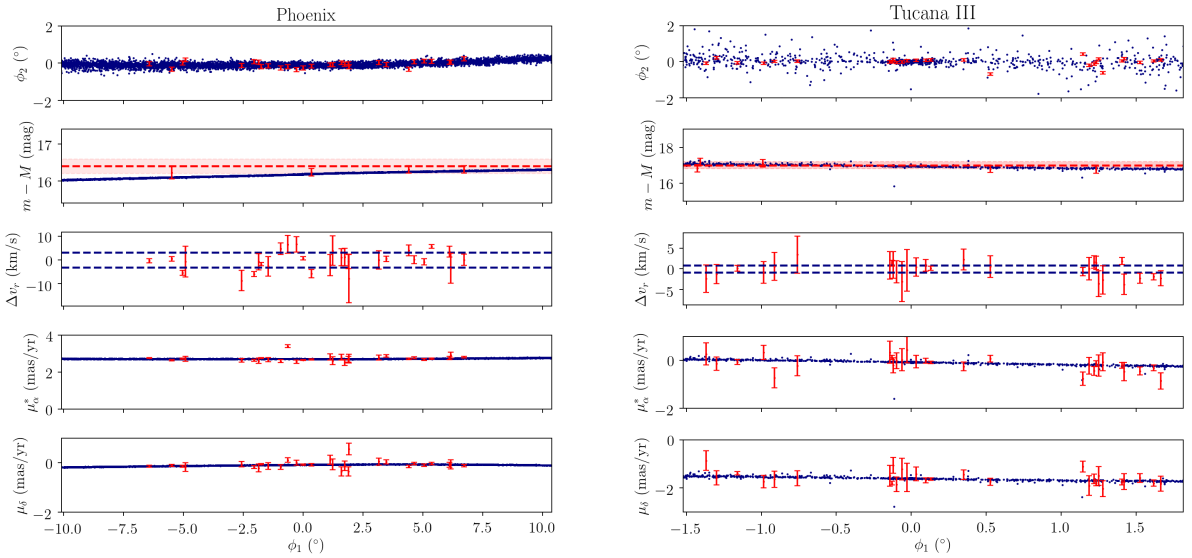

(e) (f)

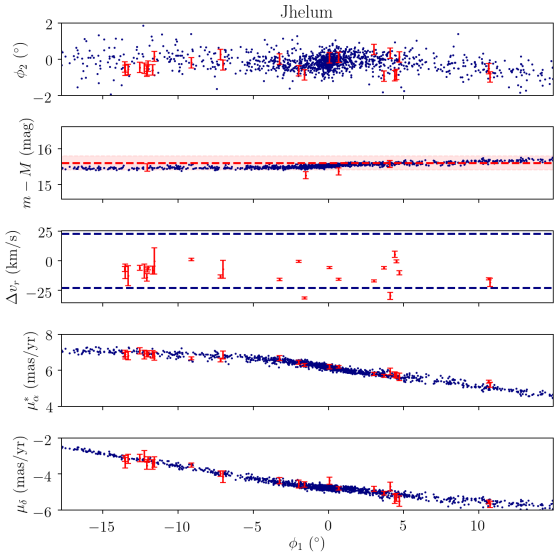

(g)

Figure 7.A.2 Stream models.

Table 7.A.3. Potential parameters

Parameter	Property		
$\Sigma_{0,\mathrm{thin}}$	679.3 $\mathrm{M}_\odot\mathrm{pc}^{-2}$	v_0	233.7 km s^{-1}
$R_{d,\mathrm{thin}}$	2.823 kpc	M_b	$9.821 \times 10^9\,\mathrm{M}_\odot$
$\Sigma_{0,\mathrm{thick}}$	231.8 $\mathrm{M}_\odot\mathrm{pc}^{-2}$	$M_{d,\mathrm{thin}}$	$3.403 \times 10^{10}\,\mathrm{M}_\odot$
$R_{d,\mathrm{thick}}$	2.956 kpc	$M_{d,\mathrm{thick}}$	$1.272 \times 10^{10}\,\mathrm{M}_\odot$
$\rho_{0,b}$	104.7 $\mathrm{M}_\odot\mathrm{pc}^{-3}$	M_v	$8.273 \times 10^{11}\,\mathrm{M}_\odot$
$\rho_{0,h}$	0.01576 $\mathrm{M}_\odot\mathrm{pc}^{-3}$	$c_{v'}$	15.07
r_h	13.14 kpc		
R_0	8.228 kpc		
U	8.406 km s^{-1}		
V	12.01 km s^{-1}		
W	7.280 km s^{-1}		

Note. — Parameters of the potential from McMillan (2017) which we use to fit streams in this work. We note that the parameters here come from a realization of the posterior MCMC chains in McMillan (2017) and are thus consistent with that work. For ease of use, the parameters are in the same format as McMillan (2017).

CHAPTER 8

CONCLUSION

Stellar streams, the tidal remnants of accreted globular clusters and dwarf galaxies, are powerful probes of near-field cosmology, and have the ability to transform our understanding of dark matter and galaxy formation in the Local Universe. These studies, however, require a large, well-observed sample of stellar streams with full 6D phase-space measurements. Until recently, such a population was unattainable. However, recent large photometric, astrometric, and spectroscopic surveys have enabled the detailed observation of populations of stellar streams. In this thesis, I presented efforts to combine these data in order to assemble and model the first-ever population of systematically-observed 6D stellar streams and to measure the mass of the Milky Way's largest perturber – the Large Magellanic Cloud.

8.1 Summary

8.1.1 Discovery of Stellar Streams

Wide-field optical imaging surveys have revolutionized the field of stellar streams in recent years, enabling significant increases in the quality of observations and the number of known Milky Way streams. The Dark Energy Survey (DES) in particular, is a powerful dataset for the study of faint stellar density features, due to the wide-area, depth, and uniformity of the survey. In Chapter 4, I presented the systematic search for stellar streams in DES, which led to the discovery of 11 new stellar streams, and improved observations of four previously known streams (Shipp et al., 2018) This increased the number of known streams at the time by $\sim 50\%$, and more than doubled the number of known streams in the Southern Hemisphere. Due to the quality and depth of the DES photometry, these streams are generally fainter, more distant, and lower surface brightness than streams detected by similar techniques in previous photometric surveys. The large distance range and wide area covered by the DES

streams make this a uniquely powerful group of stellar streams for constraining the local matter distribution and the evolution of our Galaxy.

In Chapter 5, I presented a search for stellar streams in the The Dark Energy Camera Legacy Survey (DECaLS) data, leading to the discovery of thin, extended tidal tails around the globular cluster Palomar 13 (Pal 13; Shipp et al., 2020). Pal 13 is one of only a handful of thin, extended stellar streams that has been confidently associated with a bound progenitor, and, conversely, one of the few globular clusters with detectable long tidal tails. Pal 13 has the potential, therefore, to provide crucial and unique insight into the tidal disruption of globular clusters, the formation of the stellar halo, and the gravitational field of our Galaxy.

8.1.2 6D Measurements of Stellar Streams

Complete 6D phase-space measurements are critical to the study of stellar streams. Only recently has it become possible to systematically and efficiently obtain kinematic measurements of large numbers of Milky Way streams. In this thesis, I presented the combination of the precise DES photometry and the unprecedented astrometric measurements of *Gaia* DR2 to obtain 6D measurements of stellar streams across the Southern Sky.

Proper Motions

The second data release from the *Gaia* satellite (*Gaia* DR2) has provided invaluable data for the study of stellar streams, including precision astrometric measurements of more than 1 billion stars. In Chapter 6, I presented measurements of the proper motions of the DES streams (Shipp et al., 2019), using a dataset cross-matched between *Gaia* DR2 and DES DR1. I used the precise photometric measurements of DES to efficiently remove foreground and background contamination, and the Gaia DR2 astrometry to measure the the proper motions of stream member stars. By fitting Gaussian mixture models to the data, I was able to obtain confident proper motion measurements for the majority of the DES streams,

including the most distant DES stream at 50 kpc.

These proper motion measurements are critical to the study of stellar streams. In addition, they revealed that the majority of the proper motions of the DES streams are not aligned with the track of the stream on the sky, indicating an intriguing complexity in the gravitational field experienced by these systems. Due to the proximity of the Large Magellanic Cloud (LMC) to the DES footprint, and the direction of the proper motion offsets, it is likely that perturbation by the LMC is responsible for the observed offsets. This idea was explored further in Chapter 7.

Spectroscopic Observations

As the proper motion coordinator and builder in The Southern Stellar Stream Spectroscopic Survey collaboration (S^5; Li et al., 2019), I have also played a key role in obtaining radial velocity and metallicity measurements of stellar streams across the southern sky. Historically, spectroscopic observations of stellar streams have been very difficult and, until recently, only a handful of streams had radial velocity measurements. However, by taking advantage of the precise photometric and astrometric measurements with DES and *Gaia*, we have been able to significantly increase the efficiency of target selection in order to conduct the first systematic spectroscopic survey of stellar streams. S^5 is a spectroscopic survey with $\sim$60 allocated nights on the Anglo-Australian Telescope, using the 2dF AAOmega spectrograph, with the goal of measuring radial velocities and metallicities of southern stellar streams. So far, we have observed 21 streams and we are continuing to take observations with the ultimate goal of surveying stellar streams across the entire southern sky.

8.1.3 Mass of the Large Magellanic Cloud

With data from DES, *Gaia*, and S^5, this population of 6D stellar streams is the most precisely-observed sample of streams to date, and will provide unprecedented insight into a

range of unsolved questions pertaining to the local matter distribution and the structure and evolution of our Galaxy. In Chapter 7, I presented how these data may be used to constrain the mass of the LMC (Shipp et al., 2021).

This work was motivated by the proper motion offsets discovered in Shipp et al. (2019), and by the fact that the LMC has a mass of about 15% that of the Milky Way itself, and is therefore a significant perturber to our Galaxy. It induces a reflex motion in the Milky Way and deforms its dark matter halo, both of which are essential considerations when modeling any structures orbiting our Galaxy. The influx of gas from the LMC also has the ability to cause a burst in Milky Way star formation and simulations of the LMC have shown that it may cause significant warps in the Milky Way disk. A complete understanding of the influence of the LMC requires a precise measurement of its total mass, which is currently observationally constrained only within $\sim$ 9 kpc to $\sim$ 10^{10} $M_\odot$, while the total mass is estimated to be an order of magnitude larger.

The population of stellar streams that I have presented in this thesis is uniquely able to constrain the LMC mass due to the proximity of the streams to the LMC and our extensive observations. I have fit stream models, using a particle spray method to simulate realistic streams in the presence of the Milky Way and the LMC, and have found that introducing a massive LMC can explain all of the observed proper motion offsets. Furthermore, I have used these streams to constrain the total initial mass of the LMC to $\sim$ 10^{11} $M_\odot$ (Shipp et al., 2021). Only two streams had been used previously to measure the LMC mass (Erkal et al., 2019a; Vasiliev et al., 2021); with the 6D data I have been able to use a population of streams for the first time to measure the mass of the Milky Way's largest satellite. Moreover, I have demonstrated that it is critical to include the effect of a massive LMC when drawing cosmological conclusions from observations of the Local Universe.

8.2 Looking Forward

The population of systematically-observed 6D stellar streams that I have presented in this thesis, including data from the Dark Energy Survey, *Gaia*, and the Southern Stellar Stream Spectroscopic Survey, is the most precisely-observed sample of streams to date, and will provide unprecedented insight into a range of unsolved questions pertaining to the local matter distribution and the structure and evolution of our Galaxy.

In particular, stellar streams are powerful tools in the study of near-field cosmology, providing essential insight into properties of our Galaxy and enabling us to place our Galaxy in a cosmological context, in order to test theories of dark matter and galaxy formation in the broader Universe.

For the first time, we have a population of stellar streams that is predicted to constrain the Milky Way potential to the percent level (Bonaca & Hogg, 2018). By fitting the population of streams presented in this thesis, and building upon the techniques utilized in Chapter 7 to fit the mass of the LMC, we will be able to place unprecedented constraints on the total mass, as well as the 3D shape of the joint Milky Way and LMC potential. This will enable precise comparisons between our Galaxy and Milky Way-like galaxies in simulations and extragalactic observations, tightening near-field cosmological constraints on the structure and evolution of our Universe.

In addition, this large population of well-observed stellar streams will enable detailed studies of the accretion and disruption history of the Milky Way. These systematic measurements are an essential first step towards building a complete census of stellar streams around our Galaxy, and already provide powerful insight into the population of structures that have been accreted onto and disrupted by our Galaxy, including the building blocks of the Milky Way's stellar halo. In addition, studies of satellites currently undergoing disruption, in comparison to the population of intact satellites around the Milky Way, will enable detailed tests of the disruption history of systems accreted onto the Milky Way, informing

near-field cosmological predictions.

These stellar streams will also facilitate detailed searches for low-mass dark matter subhalos around the Milky Way and enable strong constraints on the properties of dark matter. With continued and improved observations and with precise modeling of the density variations and orbits of this population of stellar streams, we will be able to study the perturbation histories of these systems, infer the population of dark subhalos around the Milky Way, and place unprecedented constraints on the particle nature of dark matter.

Several new and upcoming surveys have the ability to further revolutionize the study of stellar streams. The Vera C. Rubin Observatory's Legacy Survey of Space and Time (LSST; Ivezić et al., 2019) will extend the photometric observations of surveys such as DES across a greater portion of the sky and to fainter magnitudes, enabling the discovery of fainter, more diffuse, and more distant stellar streams, as well as the detailed study of density variations along a larger population of streams. In addition, by the end of its planned 10 year survey, LSST will extend proper motions measurements to stars about 3 magnitudes deeper than those of *Gaia*. The Dark Energy Spectroscopic Instrument (DESI; DESI Collaboration et al., 2016) has begun its spectroscopic survey in the Northern Hemisphere, and will be complementary to S^5, providing similar radial velocity and metallicity measurements for many stream member stars in a different part of the sky. The Roman space telescope (Spergel et al., 2013) will obtain measurements of resolved halo stars at great distances into the outskirts of the Milky Way, enabling the discovery of additional Milky Way stellar streams, as well as high precision proper motion measurements of faint stars. In addition, the deep imaging of surveys like LSST and Roman will enable studies of stellar streams outside of the Milky Way, around neighboring galaxies, facilitating important comparisons and complementary studies.

Continuing to model and to grow and improve observations of this population of 6D stellar streams will enable a wide range of exciting new science. Stellar streams will pro-

vide unprecedented measurements of the Milky Way, enabling us to place our Galaxy in a cosmological context, facilitate comparisons to theoretical predictions and extragalactic observations, and challenge our understanding of dark matter and galaxy formation in the Local Universe and beyond.

References

Abazajian, K. N., Adelman-McCarthy, J. K., Agüeros, M. A., et al. 2009, ApJS, 182, 543

Abbott, T. M. C., Adamow, M., Aguena, M., et al. 2021, arXiv e-prints, arXiv:2101.05765

Agnello, A. 2017, MNRAS, 471, 2013

Aihara, H., Arimoto, N., Armstrong, R., et al. 2018, PASJ, 70, S4

Amorisco, N. C., Gómez, F. A., Vegetti, S., & White, S. D. M. 2016, MNRAS, 463, L17

An, D., Beers, T. C., Santucci, R. M., et al. 2015, ApJ, 813, L28

An, D., Beers, T. C., Johnson, J. A., et al. 2013, ApJ, 763, 65

Balbinot, E., & Gieles, M. 2018, MNRAS, 474, 2479

Balbinot, E., Yanny, B., Li, T. S., et al. 2016, ApJ, 820, 58

Banik, N., & Bovy, J. 2018, ArXiv e-prints, arXiv:1809.09640

Baumgardt, H., Hilker, M., Sollima, A., & Bellini, A. 2019, MNRAS, 482, 5138

Bechtol, K., Drlica-Wagner, A., Balbinot, E., et al. 2015, ApJ, 807, 50

Behroozi, P. S., Marchesini, D., Wechsler, R. H., et al. 2013, ApJ, 777, L10

Bell, E. F., Zucker, D. B., Belokurov, V., Sharma, S., et al. 2008, ApJ, 680, 295

Belokurov, V., Evans, N. W., Irwin, M. J., Lynden-Bell, D., et al. 2007a, ApJ, 658, 337

Belokurov, V., & Koposov, S. E. 2016, MNRAS, 456, 602

Belokurov, V., Zucker, D. B., Evans, N. W., et al. 2006a, ApJ, 642, L137

—. 2006b, ApJ, 647, L111

—. 2007b, ApJ, 654, 897

Belokurov, V., Evans, N. W., Bell, E. F., et al. 2007c, ApJ, 657, L89

Bernard, E. J., Ferguson, A. M. N., Schlafly, E. F., et al. 2014, MNRAS, 443, L84

—. 2016, MNRAS, 463, 1759

Bertin, E., & Arnouts, S. 1996, A&AS, 117, 393

Bertin, E., Mellier, Y., Radovich, M., et al. 2002, in Astronomical Society of the Pacific Conference Series, Vol. 281, Astronomical Data Analysis Software and Systems XI, ed. D. A. Bohlender, D. Durand, & T. H. Handley, 228

Besla, G., Kallivayalil, N., Hernquist, L., et al. 2007, ApJ, 668, 949

—. 2010, ApJ, 721, L97

—. 2012, MNRAS, 421, 2109

Binney, J., & Tremaine, S. 2008, Galactic Dynamics: Second Edition

Blumenthal, G. R., Faber, S. M., Primack, J. R., & Rees, M. J. 1984, Nature, 311, 517

Bonaca, A., Conroy, C., Price-Whelan, A. M., & Hogg, D. W. 2019a, ApJ, 881, L37

Bonaca, A., Geha, M., & Kallivayalil, N. 2012, ApJ, 760, L6

Bonaca, A., Geha, M., Küpper, A. H. W., et al. 2014, ApJ, 795, 94

Bonaca, A., & Hogg, D. W. 2018, ApJ, 867, 101

Bonaca, A., Hogg, D. W., Price-Whelan, A. M., & Conroy, C. 2019b, ApJ, 880, 38

Bonaca, A., Pearson, S., Price-Whelan, A. M., et al. 2020, ApJ, 889, 70

Bovy, J. 2014, ApJ, 795, 95

—. 2015, The Astrophysical Journal Supplement Series, 216, 29

Bovy, J., Bahmanyar, A., Fritz, T. K., & Kallivayalil, N. 2016, ApJ, 833, 31

Bovy, J., Erkal, D., & Sanders, J. L. 2017, MNRAS, 466, 628

Bovy, J., Allende Prieto, C., Beers, T. C., et al. 2012, ApJ, 759, 131

Bowden, A., Belokurov, V., & Evans, N. W. 2015, MNRAS, 449, 1391

Boylan-Kolchin, M., Bullock, J. S., & Kaplinghat, M. 2012, MNRAS, 422, 1203

Boylan-Kolchin, M., Springel, V., White, S. D. M., & Jenkins, A. 2010, MNRAS, 406, 896

Boylan-Kolchin, M., Weisz, D. R., Johnson, B. D., et al. 2015, MNRAS, 453, 1503

Bozek, B., Boylan-Kolchin, M., Horiuchi, S., et al. 2016, MNRAS, 459, 1489

Bradford, J. D., Geha, M., Muñoz, R. R., et al. 2011, ApJ, 743, 167

Brown, T. M., Tumlinson, J., Geha, M., et al. 2014, ApJ, 796, 91

Buckley, M. R., & Peter, A. H. G. 2017, ArXiv e-prints, arXiv:1712.06615

Bullock, J. S., & Boylan-Kolchin, M. 2017, ARA&A, 55, 343

Bullock, J. S., & Johnston, K. V. 2005, ApJ, 635, 931

Burke, D., Rykoff, E. S., Allam, S., et al. 2018, AJ, 155, 41

Busha, M. T., Wechsler, R. H., Behroozi, P. S., et al. 2011, ApJ, 743, 117

Callingham, T., Cautun, M., Deason, A. J., et al. 2018, arXiv e-prints, arXiv:1808.10456

Carballo-Bello, J. A., Martínez-Delgado, D., Navarrete, C., et al. 2018, MNRAS, 474, 683

Carlberg, R. G. 2009, ApJ, 705, L223

—. 2012, ApJ, 748, 20

—. 2016, ApJ, 820, 45

—. 2019, arXiv e-prints, arXiv:1902.03275

Carlberg, R. G., & Grillmair, C. J. 2013, ApJ, 768, 171

Carollo, D., Beers, T. C., Lee, Y. S., et al. 2007, Nature, 450, 1020

Carollo, D., Beers, T. C., Chiba, M., et al. 2010, ApJ, 712, 692

Chabrier, G. 2001, ApJ, 554, 1274

Chambers, K. C., Magnier, E. A., Metcalfe, N., et al. 2016, arXiv e-prints, arXiv:1612.05560

Claydon, I., Gieles, M., & Zocchi, A. 2017, MNRAS, 466, 3937

Clem, J. L. 2005, PhD thesis, University of Victoria

Clementini, G., Ripepi, V., Molinaro, R., et al. 2019, A&A, 622, A60

Côté, P., Djorgovski, S. G., Meylan, G., Castro, S., & McCarthy, J. K. 2002, ApJ, 574, 783

Cullinane, L. R., Mackey, A. D., Da Costa, G. S., et al. 2020, MNRAS, 497, 3055

Dalessandro, E., Miocchi, P., Carraro, G., Jílková, L., & Moitinho, A. 2015, MNRAS, 449, 1811

Dalton, G. 2016, in Astronomical Society of the Pacific Conference Series, Vol. 507, Multi-Object Spectroscopy in the Next Decade: Big Questions, Large Surveys, and Wide Fields, ed. I. Skillen, M. Balcells, & S. Trager, 97

Dambis, A. K. 2006, Astronomical and Astrophysical Transactions, 25, 185

Das, P., & Binney, J. 2016, MNRAS, 460, 1725

de Boer, T. J. L., Belokurov, V., Koposov, S. E., et al. 2018, MNRAS, 477, 1893

de Boer, T. J. L., Erkal, D., & Gieles, M. 2020, MNRAS, 494, 5315

de Grijs, R., & Bono, G. 2016, ApJS, 227, 5

de Jong, J. T. A., Yanny, B., Rix, H.-W., et al. 2010, ApJ, 714, 663

de Jong, R. S., Agertz, O., Berbel, A. A., et al. 2019, The Messenger, 175, 3

Deason, A. J., Belokurov, V., & Evans, N. W. 2011, MNRAS, 416, 2903

Dehnen, W., & Binney, J. 1998, MNRAS, 294, 429

DES Collaboration. 2005, ArXiv Astrophysics e-prints

—. 2016, MNRAS, 460, 1270

—. 2017, ArXiv e-prints

DES Collaboration, Abbott, T. M. C., Abdalla, F. B., et al. 2018, The Astrophysical Journal Supplement Series, 239, 18

DESI Collaboration, Aghamousa, A., Aguilar, J., et al. 2016, arXiv e-prints, arXiv:1611.00036

Dey, A., Schlegel, D. J., Lang, D., et al. 2018, ArXiv e-prints

—. 2019, AJ, 157, 168

Diehl, H. T., Neilsen, E., Gruendl, R., Yanny, B., et al. 2016, in Proc. SPIE, Vol. 9910, Observatory Operations: Strategies, Processes, and Systems VI, 99101D

Diemand, J., Kuhlen, M., Madau, P., et al. 2008, Nature, 454, 735

Diemand, J., Moore, B., & Stadel, J. 2005, Nature, 433, 389

Dinescu, D. I., Girard, T. M., van Altena, W. F., Mendez, R. A., & Lopez, C. E. 1997, AJ, 114, 1014

Dinescu, D. I., van Altena, W. F., Girard, T. M., & López, C. E. 1999, AJ, 117, 277

Dooley, G. A., Peter, A. H. G., Carlin, J. L., et al. 2017a, MNRAS, 472, 1060

Dooley, G. A., Peter, A. H. G., Yang, T., et al. 2017b, MNRAS, 471, 4894

Dotter, A., Chaboyer, B., Jevremović, D., et al. 2008, ApJS, 178, 89

Drimmel, R., & Poggio, E. 2018, Research Notes of the American Astronomical Society, 2, 210

Drlica-Wagner, A., Sevilla-Noarbe, I., Rykoff, E. S., et al. 2018, ApJS, 235, 33

Drlica-Wagner, A., Bechtol, K., Rykoff, E. S., et al. 2015, ApJ, 813, 109

Drlica-Wagner, A., Bechtol, K., Allam, S., et al. 2016, ApJ, 833, L5

Drlica-Wagner, A., Bechtol, K., Mau, S., et al. 2020, ApJ, 893, 47

Eilers, A.-C., Hogg, D. W., Rix, H.-W., & Ness, M. 2018, arXiv e-prints, arXiv:1810.09466

Erkal, D., & Belokurov, V. 2015a, MNRAS, 450, 1136

—. 2015b, MNRAS, 454, 3542

Erkal, D., Belokurov, V., Bovy, J., & Sanders, J. L. 2016a, MNRAS, 463, 102

Erkal, D., Belokurov, V., & Parkin, D. L. 2020a, arXiv e-prints, 498, arXiv:2001.11030

Erkal, D., & Belokurov, V. A. 2020, MNRAS, 495, 2554

Erkal, D., Koposov, S. E., & Belokurov, V. 2017, MNRAS, 470, 60

Erkal, D., Sanders, J. L., & Belokurov, V. 2016b, MNRAS, 461, 1590

Erkal, D., Li, T. S., Koposov, S. E., et al. 2018, MNRAS, 481, 3148

Erkal, D., Belokurov, V., Laporte, C. F. P., et al. 2019a, MNRAS, 487, 2685

—. 2019b, MNRAS, 487, 2685

Erkal, D., Deason, A. J., Belokurov, V., et al. 2020b, arXiv e-prints, arXiv:2010.13789

Eyre, A., & Binney, J. 2009, MNRAS, 399, L160

Fardal, M. A., Huang, S., & Weinberg, M. D. 2015, MNRAS, 452, 301

Fardal, M. A., van der Marel, R. P., Sohn, S. T., & del Pino Molina, A. 2019, MNRAS, 486, 936

Feroz, F., & Hobson, M. P. 2008, MNRAS, 384, 449

Feroz, F., Hobson, M. P., & Bridges, M. 2009, MNRAS, 398, 1601

Fitzpatrick, E. L. 1999, PASP, 111, 63

Flaugher, B., Diehl, H. T., Honscheid, K., et al. 2015, AJ, 150, 150

Foreman-Mackey, D., Hogg, D. W., Lang, D., & Goodman, J. 2013, PASP, 125, 306

Frebel, A., & Norris, J. E. 2015, ARA&A, 53, 631

Fritz, T. K., Battaglia, G., Pawlowski, M. S., et al. 2018, A&A, 619, A103

Gaia Collaboration, Brown, A. G. A., Vallenari, A., et al. 2020, arXiv e-prints, arXiv:2012.01533

Gaia Collaboration, Prusti, T., de Bruijne, J. H. J., et al. 2016, A&A, 595, A1

Gaia Collaboration, Brown, A. G. A., Vallenari, A., et al. 2018, A&A, 616, A1

Garavito-Camargo, N., Besla, G., Laporte, C. F. P., et al. 2019, ApJ, 884, 51

—. 2020, arXiv e-prints, arXiv:2010.00816

Garrison-Kimmel, S., Wetzel, A., Bullock, J. S., et al. 2017, MNRAS, 471, 1709

Gibbons, S. L. J., Belokurov, V., & Evans, N. W. 2014, MNRAS, 445, 3788

Gillessen, S., Eisenhauer, F., Trippe, S., et al. 2009, ApJ, 692, 1075

Gnedin, O. Y., & Ostriker, J. P. 1997, ApJ, 474, 223

Gómez, F. A., Besla, G., Carpintero, D. D., et al. 2015, ApJ, 802, 128

Górski, K. M., Hivon, E., Banday, A. J., et al. 2005, ApJ, 622, 759

Green, A. M., Hofmann, S., & Schwarz, D. J. 2004, MNRAS, 353, L23

Grillmair, C. J. 2006, ApJ, 645, L37

—. 2009, ApJ, 693, 1118

—. 2014, ApJ, 790, L10

—. 2017a, ApJ, 847, 119

—. 2017b, ApJ, 834, 98

—. 2019, ApJ, 884, 174

Grillmair, C. J., & Carlberg, R. G. 2016, ApJ, 820, L27

Grillmair, C. J., & Dionatos, O. 2006, ApJ, 643, L17

Grillmair, C. J., Freeman, K. C., Irwin, M., & Quinn, P. J. 1995, AJ, 109, 2553

Grillmair, C. J., Jarrett, T. H., & Ha, A. C. 2004, in Astronomical Society of the Pacific Conference Series, Vol. 327, Satellites and Tidal Streams, ed. F. Prada, D. Martinez Delgado, & T. J. Mahoney, 276

Hamilton, A. J. S., & Tegmark, M. 2004, MNRAS, 349, 115

Harris, W. E. 1996, AJ, 112, 1487

—. 2010, arXiv e-prints, arXiv:1012.3224

Hattori, K., Erkal, D., & Sanders, J. L. 2016, MNRAS, 460, 497

Hattori, K., Yoshii, Y., Beers, T. C., Carollo, D., & Lee, Y. S. 2013, ApJ, 763, L17

Helmi, A., & White, S. D. M. 1999, MNRAS, 307, 495

Hernquist, L. 1990, ApJ, 356, 359

Holl, B., Audard, M., Nienartowicz, K., et al. 2018, A&A, 618, A30

Ibata, R., Irwin, M., Lewis, G. F., & Stolte, A. 2001, ApJ, 547, L133

Ibata, R. A., Bellazzini, M., Malhan, K., Martin, N., & Bianchini, P. 2019, Nature Astronomy, 3, 667

Ibata, R. A., Gilmore, G., & Irwin, M. J. 1994, Nature, 370, 194

Ibata, R. A., Lewis, G. F., Irwin, M. J., & Quinn, T. 2002, MNRAS, 332, 915

Ibata, R. A., Lewis, G. F., & Martin, N. F. 2016, ApJ, 819, 1

Ibata, R. A., Lewis, G. F., Thomas, G., Martin, N. F., & Chapman, S. 2017, ApJ, 842, 120

Iorio, G., Belokurov, V., Erkal, D., et al. 2018, MNRAS, 474, 2142

Ivezić, Ž., Kahn, S. M., Tyson, J. A., et al. 2019, ApJ, 873, 111

Jarvis, M., Sheldon, E., Zuntz, J., et al. 2016, MNRAS, 460, 2245

Jethwa, P., Erkal, D., & Belokurov, V. 2016, MNRAS, 461, 2212

Jethwa, P., Torrealba, G., Navarrete, C., et al. 2017, ArXiv e-prints, arXiv:1711.09103

—. 2018, MNRAS, 480, 5342

Ji, A. P., Li, T. S., Hansen, T. T., et al. 2020, AJ, 160, 181

Johnston, K. V. 1998, ApJ, 495, 297

—. 2016, Origins and Interpretation of Tidal Debris, ed. H. J. Newberg & J. L. Carlin, Vol. 420, 141

Johnston, K. V., Law, D. R., & Majewski, S. R. 2005, ApJ, 619, 800

Johnston, K. V., Spergel, D. N., & Haydn, C. 2002, ApJ, 570, 656

Jones, E., Oliphant, T., Peterson, P., et al. 2001–, SciPy: Open source scientific tools for Python, Zenodo

Jurić, M., Ivezić, Ž., Brooks, A., et al. 2008, ApJ, 673, 864

Kafle, P. R., Sharma, S., Lewis, G. F., & Bland-Hawthorn, J. 2013, MNRAS, 430, 2973

Kallivayalil, N., van der Marel, R. P., Alcock, C., et al. 2006, ApJ, 638, 772

Kallivayalil, N., van der Marel, R. P., Besla, G., Anderson, J., & Alcock, C. 2013a, ApJ, 764, 161

—. 2013b, ApJ, 764, 161

Kim, D., & Jerjen, H. 2015, ApJ, 808, L39

King, I. 1962, AJ, 67, 471

Kirby, E. N., Cohen, J. G., Guhathakurta, P., et al. 2013, ApJ, 779, 102

Koposov, S. E., Belokurov, V., Torrealba, G., & Evans, N. W. 2015, ApJ, 805, 130

Koposov, S. E., Irwin, M., Belokurov, V., et al. 2014, MNRAS, 442, L85

Koposov, S. E., Rix, H.-W., & Hogg, D. W. 2010, ApJ, 712, 260

Koposov, S. E., Belokurov, V., Evans, N. W., et al. 2012, ApJ, 750, 80

Koposov, S. E., Belokurov, V., Li, T. S., et al. 2019, MNRAS, 485, 4726

Küpper, A. H. W., Balbinot, E., Bonaca, A., et al. 2015a, ApJ, 803, 80

—. 2015b, ApJ, 803, 80

Küpper, A. H. W., Lane, R. R., & Heggie, D. C. 2012, MNRAS, 420, 2700

Kuzma, P. B., Da Costa, G. S., & Mackey, A. D. 2018, MNRAS, 473, 2881

Lang, D., Hogg, D. W., & Mykytyn, D. 2016, The Tractor: Probabilistic astronomical source detection and measurement

Laporte, C. F. P., Gómez, F. A., Besla, G., Johnston, K. V., & Garavito-Camargo, N. 2018, MNRAS, 473, 1218

Law, D. R., Johnston, K. V., & Majewski, S. R. 2005, ApJ, 619, 807

Law, D. R., & Majewski, S. R. 2010, ApJ, 714, 229

Leon, S., Meylan, G., & Combes, F. 2000, A&A, 359, 907

Levine, E. S., Blitz, L., & Heiles, C. 2006, ApJ, 643, 881

Lewis, I. J., Cannon, R. D., Taylor, K., et al. 2002, MNRAS, 333, 279

Li, T. S., Balbinot, E., Mondrik, N., et al. 2016, ApJ, 817, 135

Li, T. S., Simon, J. D., Kuehn, K., et al. 2018, ApJ, 866, 22

Li, T. S., Koposov, S. E., Zucker, D. B., et al. 2019, MNRAS, 490, 3508

Li, T. S., Koposov, S. E., Erkal, D., et al. 2020, arXiv e-prints, arXiv:2006.10763

Lindegren, L., Hernández, J., Bombrun, A., et al. 2018, A&A, 616, A2

LSST Science Collaboration. 2009, ArXiv e-prints

Luque, E., Pieres, A., Santiago, B., et al. 2017, MNRAS, 468, 97

Luque, E., Queiroz, A., Santiago, B., et al. 2016, MNRAS, 458, 603

Luque, E., Santiago, B., Pieres, A., et al. 2018, MNRAS

Majewski, S. R., Skrutskie, M. F., Weinberg, M. D., & Ostheimer, J. C. 2003, ApJ, 599, 1082

Majewski, S. R., Kunkel, W. E., Law, D. R., et al. 2004, AJ, 128, 245

Majewski, S. R., Schiavon, R. P., Frinchaboy, P. M., et al. 2017, AJ, 154, 94

Malhan, K., & Ibata, R. A. 2018, MNRAS, 477, 4063

Malhan, K., Ibata, R. A., & Martin, N. F. 2018, MNRAS, 481, 3442

Martínez-Delgado, D., Gabany, R. J., Crawford, K., et al. 2010, AJ, 140, 962

Mateu, C., Read, J. I., & Kawata, D. 2018a, MNRAS, 474, 4112

—. 2018b, MNRAS, 474, 4112

McMillan, P. J. 2017, MNRAS, 465, 76

Miyamoto, M., & Nagai, R. 1975, Publications of the Astronomical Society of Japan, 27, 533

Morganson, E., Gruendl, R. A., Menanteau, F., et al. 2018, Publications of the Astronomical Society of the Pacific, 130, 074501

Moster, B. P., Naab, T., & White, S. D. M. 2013, MNRAS, 428, 3121

Muraveva, T., Delgado, H. E., Clementini, G., Sarro, L. M., & Garofalo, A. 2018, MNRAS, 481, 1195

Myeong, G. C., Jerjen, H., Mackey, D., & Da Costa, G. S. 2017, ApJ, 840, L25

Nadler, E. O., Wechsler, R. H., Bechtol, K., et al. 2020, ApJ, 893, 48

Nadler, E. O., Drlica-Wagner, A., Bechtol, K., et al. 2021, Phys. Rev. Lett., 126, 091101

Navarrete, C., Belokurov, V., & Koposov, S. E. 2017, The Astrophysical Journal, 841, L23

Newberg, H. J., & Carlin, J. L., eds. 2016, Astrophysics and Space Science Library, Vol. 420, Tidal Streams in the Local Group and Beyond

Newberg, H. J., Yanny, B., & Willett, B. A. 2009, ApJ, 700, L61

Newberg, H. J., Yanny, B., Rockosi, C., et al. 2002, ApJ, 569, 245

Ngan, W. H. W., & Carlberg, R. G. 2014, ApJ, 788, 181

Nidever, D. L., Majewski, S. R., & Butler Burton, W. 2008, ApJ, 679, 432

Nidever, D. L., Olsen, K., Walker, A. R., et al. 2017, AJ, 154, 199

Niederste-Ostholt, M., Belokurov, V., Evans, N. W., et al. 2010, MNRAS, 408, L66

Odenkirchen, M., Grebel, E. K., Rockosi, C. M., et al. 2001, ApJ, 548, L165

Olszewski, E. W., Saha, A., Knezek, P., et al. 2009, AJ, 138, 1570

Pace, A. B., & Li, T. S. 2019, ApJ, 875, 77

Pawlowski, M. S., McGaugh, S. S., & Jerjen, H. 2015, MNRAS, 453, 1047

Pawlowski, M. S., Pflamm-Altenburg, J., & Kroupa, P. 2012, MNRAS, 423, 1109

Peñarrubia, J., Gómez, F. A., Besla, G., Erkal, D., & Ma, Y.-Z. 2016, MNRAS, 456, L54

Pearson, S., Küpper, A. H. W., Johnston, K. V., & Price-Whelan, A. M. 2015, ApJ, 799, 28

Pearson, S., Price-Whelan, A. M., & Johnston, K. V. 2017, Nature Astronomy, 1, 633

Peebles, P. J. E. 1965, ApJ, 142, 1317

Perryman, M. A. C., Lindegren, L., Kovalevsky, J., et al. 1997, A&A, 500, 501

Petersen, M. S., & Peñarrubia, J. 2020, MNRAS, 494, L11

—. 2021, Nature Astronomy, 5, 251

Piatti, A. E. 2018, MNRAS, 473, 492

Piatti, A. E., & Fernández-Trincado, J. G. 2020, A&A, 635, A93

Pieres, A., Santiago, B., Balbinot, E., et al. 2016, MNRAS, 461, 519

Pieres, A., Santiago, B. X., Drlica-Wagner, A., et al. 2017, MNRAS, 468, 1349

Pietrzyński, G., Graczyk, D., Gieren, W., et al. 2013a, Nature, 495, 76

—. 2013b, Nature, 495, 76

Plummer, H. C. 1911, MNRAS, 71, 460

Prada, J., Forero-Romero, J. E., Grand, R. J. J., Pakmor, R., & Springel, V. 2019, MNRAS, 490, 4877

Press, W. H., & Schechter, P. 1974, ApJ, 187, 425

Price-Whelan, A. M. 2017, The Journal of Open Source Software, 2, 388

Price-Whelan, A. M., & Bonaca, A. 2018, ApJ, 863, L20

Price-Whelan, A. M., Hogg, D. W., Johnston, K. V., & Hendel, D. 2014, ApJ, 794, 4

Price-Whelan, A. M., Mateu, C., Iorio, G., et al. 2019, AJ, 158, 223

Robertson, B. E., Ellis, R. S., Dunlop, J. S., McLure, R. J., & Stark, D. P. 2010, Nature, 468, 49

Robles, V. H., Kelley, T., Bullock, J. S., & Kaplinghat, M. 2019, MNRAS, 490, 2117

Rocha-Pinto, H. J., Majewski, S. R., Skrutskie, M. F., Crane, J. D., & Patterson, R. J. 2004, ApJ, 615, 732

Rockosi, C. M., Odenkirchen, M., Grebel, E. K., et al. 2002, AJ, 124, 349

Röser, S., & Schilbach, E. 2019, A&A, 627, A4

Rosino, L. 1957, Mem. Soc. Astron. Italiana, 28, 293

Rozo, E., Rykoff, E. S., Abate, A., et al. 2016, MNRAS, 461, 1431

Sanders, J. L. 2014, MNRAS, 443, 423

Sanders, J. L., & Binney, J. 2013, MNRAS, 433, 1813

Sanders, J. L., Bovy, J., & Erkal, D. 2016, MNRAS, 457, 3817

Sanders, J. L., Smith, L., & Evans, N. W. 2019, MNRAS, 488, 4552

Sanderson, R. E., Vera-Ciro, C., Helmi, A., & Heit, J. 2016, ArXiv e-prints

Sandford, E., Küpper, A. H. W., Johnston, K. V., & Diemand, J. 2017, MNRAS, 470, 522

Schlafly, E. F., & Finkbeiner, D. P. 2011, ApJ, 737, 103

Schlegel, D. J., Finkbeiner, D. P., & Davis, M. 1998, ApJ, 500, 525

Schommer, R. A., Suntzeff, N. B., Olszewski, E. W., & Harris, H. C. 1992, AJ, 103, 447

Schönrich, R., Binney, J., & Dehnen, W. 2010a, MNRAS, 403, 1829

—. 2010b, MNRAS, 403, 1829

Sesar, B., Bovy, J., Bernard, E. J., et al. 2015, ApJ, 809, 59

Sesar, B., Hernitschek, N., Mitrović, S., et al. 2017, AJ, 153, 204

Shanks, T., Metcalfe, N., Chehade, B., et al. 2015, MNRAS, 451, 4238

Sharp, R., Saunders, W., Smith, G., et al. 2006, in Society of Photo-Optical Instrumentation Engineers (SPIE) Conference Series, Vol. 6269, Society of Photo-Optical Instrumentation Engineers (SPIE) Conference Series, 62690G

Sheldon, E. S. 2014, MNRAS, 444, L25

Shipp, N., Erkal, D., Drlica-Wagner, A., et al. 2021, AJ

Shipp, N., Price-Whelan, A. M., Tavangar, K., Mateu, C., & Drlica-Wagner, A. 2020, AJ, 160, 244

Shipp, N., Drlica-Wagner, A., Balbinot, E., et al. 2018, ApJ, 862, 114

Shipp, N., Li, T. S., Pace, A. B., et al. 2019, ApJ, 885, 3

Siegel, M. H., Majewski, S. R., Cudworth, K. M., & Takamiya, M. 2001, AJ, 121, 935

Simon, J. D. 2018, ApJ, 863, 89

Simon, J. D., Li, T. S., Drlica-Wagner, A., et al. 2017, ApJ, 838, 11

Skrutskie, M. F., Cutri, R. M., Stiening, R., et al. 2006, AJ, 131, 1163

Sollima, A. 2020, MNRAS, 495, 2222

Sollima, A., Martínez-Delgado, D., Valls-Gabaud, D., & Peñarrubia, J. 2011, ApJ, 726, 47

Spergel, D., Gehrels, N., Breckinridge, J., et al. 2013, arXiv e-prints, arXiv:1305.5425

Springel, V., Wang, J., Vogelsberger, M., et al. 2008, MNRAS, 391, 1685

Swanson, M. E. C., Tegmark, M., Hamilton, A. J. S., & Hill, J. C. 2008, MNRAS, 387, 1391

The MSE Science Team, Babusiaux, C., Bergemann, M., et al. 2019, arXiv e-prints, arXiv:1904.04907

van der Marel, R. P. 2006, in The Local Group as an Astrophysical Laboratory, ed. M. Livio & T. M. Brown, Vol. 17, 47–71

van der Marel, R. P., Alves, D. R., Hardy, E., & Suntzeff, N. B. 2002a, AJ, 124, 2639

—. 2002b, AJ, 124, 2639

van der Marel, R. P., & Kallivayalil, N. 2014a, ApJ, 781, 121

—. 2014b, ApJ, 781, 121

Vasiliev, E. 2019, MNRAS, 484, 2832

Vasiliev, E., Belokurov, V., & Erkal, D. 2020, arXiv e-prints, arXiv:2009.10726

—. 2021, MNRAS, 501, 2279

Vera-Ciro, C., & Helmi, A. 2013, ApJ, 773, L4

Walker, A. R., Kunder, A. M., Andreuzzi, G., et al. 2011, MNRAS, 415, 643

Wan, Z., Lewis, G. F., Li, T. S., et al. 2020, Nature, 583, 768

Wang, J., Bose, S., Frenk, C. S., et al. 2020, Nature, 585, 39

Wang, W., & White, S. D. M. 2012, MNRAS, 424, 2574

Watkins, L. L., van der Marel, R. P., Sohn, S. T., & Evans, N. W. 2018, arXiv e-prints, arXiv:1804.11348

Weinberg, M. D. 1998, MNRAS, 299, 499

Weinberg, M. D., & Blitz, L. 2006, ApJ, 641, L33

Weisz, D. R., Dolphin, A. E., Skillman, E. D., et al. 2014, ApJ, 789, 148

Willman, B., Blanton, M. R., West, A. A., et al. 2005a, AJ, 129, 2692

Willman, B., Dalcanton, J. J., Martinez-Delgado, D., et al. 2005b, ApJ, 626, L85

Yanny, B., Newberg, H. J., Grebel, E. K., et al. 2003, ApJ, 588, 824

Yepez, M. A., Arellano Ferro, A., Schröder, K. P., et al. 2019, , 71, 1

Yoon, J. H., Johnston, K. V., & Hogg, D. W. 2011a, ApJ, 731, 58

—. 2011b, ApJ, 731, 58

York, D. G., Adelman, J., Anderson, Jr., J. E., et al. 2000, AJ, 120, 1579

Zhao, G., Zhao, Y.-H., Chu, Y.-Q., Jing, Y.-P., & Deng, L.-C. 2012, Research in Astronomy and Astrophysics, 12, 723

Zucker, D. B., Kniazev, A. Y., Bell, E. F., et al. 2004, ApJ, 612, L117

Zucker, D. B., Belokurov, V., Evans, N. W., et al. 2006a, ApJ, 650, L41

—. 2006b, ApJ, 643, L103